FEDERAL UNIVERSITY OF MINAS GERAIS

Graduate Program in Metallurgical, Materials and Mining Engineering

Programa de Pós-Graduação em Engenharia Metalúrgica, Materiais e de Minas

Doctoral Thesis

The Applicability of X-ray Microtomography for Mineral Liberation Determination

A Aplicabilidade da Microtomografia de Raios-X para a Determinação de Liberação Mineral

Author: Guilherme José Ramos Oliveira

Academic Advisor: Prof. Doctor Douglas Batista Mazzinghy

Academic Co-advisor: Prof. Doctor Daniela Gomes Horta

April/2021

Guilherme José Ramos Oliveira

The Applicability of X-ray Microtomography for Mineral Liberation Determination

A Aplicabilidade da Microtomografia de Raios-X para a Determinação de Liberação Mineral

Doctoral thesis presented to the Graduate Program in Metallurgical, Materials and Mining Engineering of the School of Engineering of the Federal University of Minas Gerais, in partial fulfilment of the requirement for the degree of Doctor in Metallurgical, Materials and Mining Engineering.

Area of concentration: Mineral Technology

Academic Advisor: Prof. Doctor Douglas Batista Mazzinghy

Academic Co-advisor: Prof. Doctor Daniela Gomes Horta

Belo Horizonte

Federal University of Minas Gerais

2021

Oliveira, Guilherme José Ramos.
O48a The Applicability of X-ray Microtomography for Mineral Liberation Determination [recurso eletrônico] = A Aplicabilidade da Microtomografia de Raios-X para a Determinação de Liberação Mineral / Guilherme José Ramos Oliveira. – 2021.
1 recurso online (121 f.: il., color.): pdf.

Orientador: Douglas Batista Mazzinghy.
Coorientadora: Daniela Gomes Horta.

Tese (doutorado) - Universidade Federal de Minas Gerais, Escola de Engenharia.

Inclui bibliografia.

Exigências do sistema: Adobe Acrobat Reader.

1. Engenharia de Minas - Teses. 2. Tecnologia mineral - Teses. 3. Estereologia– Teses. 4. Processamento de imagens—Técnicas digitais -- Teses. I. Mazzinghy, Douglas Batista. II. Horta, Daniela Gomes. III. Universidade Federal de Minas Gerais. Escola de Engenharia. IV. Título.

CDU: 622(043)

Ficha catalográfica: Biblioteca Prof. Mário Werneck, Escola de Engenharia da UFMG

UNIVERSIDADE FEDERAL DE MINAS GERAIS
ESCOLA DE ENGENHARIA
Programa de Pós-Graduação em Engenharia Metalúrgica, Materiais e de Minas

Tese intitulada **"The Applicability Of X-ray Microtomography For Mineral Liberation Determination"**, área de concentração: Tecnologia Mineral, apresentada pelo candidato **Guilherme José Ramos Oliveira**, para obtenção do grau de Doutor em Engenharia Metalúrgica, Materiais e de Minas, aprovada pela comissão examinadora constituída pelos seguintes membros:

Prof. Douglas Batista Mazzinghy
Orientador - Dr. (UFMG)

Profª Daniela Gomes Horta
Coorientadora - Drª (UNIFAL-Poços de Caldas)

Profª Carolina del Roveri
Drª (UNIFAL-MG)

Profª Fabiane Leocádia da Silva
Drª (UEMG)

Prof. Maurício Guimarães Bergerman
Dr. (USP)

Profª Carina Ulsen
Drª (USP)

Prof. Rodrigo Lambert Orefice
Coordenador do Programa de Pós-Graduação em Engenharia Metalúrgica, Materiais e de Minas/UFMG
Belo Horizonte, 01 de abril de 2021

AGRADECIMENTOS

Agradeço ao meu orientador, Prof. Douglas Mazzinghy, pelos ensinamentos, pela dedicação e, principalmente, pelo compromisso que assumiu ao aceitar me orientar. Todas as conversas e discussões que tivemos, desde o primeiro contato, foram essenciais para manter a calma e o foco para recomeçar o doutorado.

À Prof.ª Daniela Horta, que tem me ajudado desde mesmo antes de saber seu nome e me coorientar. Seu apoio foi valioso no último ano, tanto como coorientadora, como colega de UNIFAL-MG.

À Prof.ª Fabiane Leocádia, que se mostrou extremamente prestativa desde o primeiro convite para usar o microtomógrafo no NanoLab da UFOP e pelas análises de DRX. Agradeço, também, a toda equipe do NanoLab pelas análises no TIMA, em especial ao Fernando von Krüger e ao Prof. Guilherme Brigolini.

À Coordenação de Aperfeiçoamento de Pessoal de Nível Superior (CAPES) e ao Conselho Nacional de Desenvolvimento Científico e Tecnológico (CNPq) pelo financiamento, especialmente a este último pela minha bolsa de doutorado.

À ALCOA pelas amostras de bauxita.

Agradeço à Cida Pacheco, secretária do PPGEM, pelos momentos de descontração na sala da pós e por sempre estar de prontidão para auxiliar os discentes do programa.

Um obrigado muito especial para todos os amigos do PPGEM, em especial Gisele, Luana, Dirce, Denise, Ricardo, Mariana, Hugo, Moara, Paula, Lorena e Bia. Os momentos na sala da pós ou no laboratório, dividindo alegrias e anseios, foram fundamentais para não surtar.

Ao João Henrique por todos os compartilhamentos e carinho, desde o início do mestrado.

Aos meus amigos Isabel, Maria Olívia, Kamylla e Guilherme que, de perto ou de longe, não deixaram de estar ao meu lado. Amo vocês.

Gratidão a todo amor da minha família e, principalmente, pelo suporte incondicional para seguir meu sonho da carreira acadêmica.

TABLE OF CONTENTS

LIST OF FIGURES

LIST OF TABLES

LIST OF ABBREVIATIONS

μCT	X-ray microtomography
2D	Two-dimensional
3D	Three-dimensional
BET	Brunauer, Emmett and Teller
BJH	Barrett-Joyner-Halend
BSE	Backscattered electrons
CAPES	Coordenação de Aperfeiçoamento de Pessoal de Nível Superior
CNPq	Conselho Nacional de Desenvolvimento Científico e Tecnológico
EDS	Energy-dispersive X-ray Spectroscopy
EDS	Espectroscopia de Raios-X por Energia Dispersiva
FEG	Field emission gun
FT	Fourier transform
FTIR	Fourier Transform Infrared Spectroscopy
MEV	Microscopia Eletrônica de Varredura
MLA	Mineral Liberation Analyzer
NLM	Non-local means filter
QEMSCAN	Quantitative Evaluation of Minerals by Scanning Electron Microscopy
SEM	Scanning electron microscope/microscopy
TIMA	TESCAN Integrated Mineral Analyzer
XRD	X-ray diffraction
XRF	X-ray fluorescence

LIST OF NOTATIONS

μ	linear attenuation coefficient
$\mu(x,y)$	position-dependent attenuation coefficient
d	interplanar distance
E	photon energy
I	transmitted intensity
I_0	intensity of the incident beam
M	number of projections taken in 180º
n	diffraction order
N	number of steps (Shannon theorem)
$P_\theta(t)$	set of projections (sinogram)
$S_\theta(w$	Fourier transform of a projection
t	scanning direction vector
w	frequency
x	length crossed by a photon through an object
Z	atomic number
Δz	slice thickness
H	backscattered coefficient
θ	scattering angle
λ	X-ray wavelength
ρ	density of the material

ABSTRACT

In mineral processing, a detailed characterization of multiphase particulate systems is fundamental to guarantee an efficient separation of the valuable minerals. A precise analysis allows the process engineer, for instance, to evaluate the optimum concentration route and to achieve the best metallurgical recovery possible. One of the most important aspects of the ore is mineral liberation, as it defines the maximum possible grade for subsequent mineral concentration processes. Scanning electron microscope-based (SEM-based) automated image analysis systems have been used to obtain information concerning mineral liberation. One of the limitations of SEM-based techniques for mineral liberation assessment is the unavoidable loss of 3D information, leading to significant stereological errors. In this regard, X-ray microtomography emerges as a solution that allows three-dimensional imaging and direct measurement of spatial characteristics of mineral ores, eliminating stereological issues. In this thesis, high-resolution X-ray microtomography was used to evaluate the characteristics of liberation of a metallurgical bauxite ore and of an iron ore tailing. Mineralogical characterization showed that the bauxite ore was composed by 54.5% of gibbsite as the aluminum-bearing mineral, 39.8% of kaolinite as silicate gangue, and 5.7% of hematite, whereas the iron ore tailing was constituted by 88.8% of quartz, 10.4% of hematite, and 0.8% of goethite. The liberation analyses were carried out with respect to compositional liberation (grade) and textural liberation (surface exposure), in both 2D and 3D perspectives to assess the degree of stereological bias. For the bauxite ore, grade distributions in 2D and 3D were correspondent when all possible cross-sections were considered in 2D. However, 2D surface exposure did not converge accurately to the 3D fashion due to the loss of 3D information. In the case of the iron ore tailing, the stereological effect was more pronounced in surface exposure quantification. There was a linear relationship between grade and surface exposure and also between particle size and surface exposure. A comparison of the results of SEM-based and X-ray microtomography for the iron ore tailing evidenced the fact that only a 3D technique would be able to represent the real characteristics of particulate systems.

Keywords: X-ray microtomography, mineral liberation, stereological errors

RESUMO

No processamento de minerais, uma caracterização detalhada de partículas é fundamental para garantir uma separação eficiente dos minerais de interesse. Uma análise precisa permite que engenheiro, por exemplo, avalie a melhor rota de concentração e obtenha a melhor recuperação metalúrgica possível. Um dos aspectos mais importantes do minério é a liberação mineral, pois define o teor máximo possível para os processos subsequentes de concentração mineral. Equipamentos automatizados de análise de imagem baseados em Microscopia Eletrônica de Varredura (MEV) têm sido utilizados para obter informações sobre o grau de liberação mineral. Uma das limitações das técnicas baseadas em observações ao microscópio para avaliação da liberação de minerais é a perda inevitável de informações em 3D, levando a erros estereológicos significativos. Nesse sentido, a microtomografia de raios-X surge como uma alternativa que permite a obtenção de imagens tridimensionais e medição direta das características espaciais dos minérios, eliminando os efeitos estereológicos. Nesta tese, microtomografia de raios-X de alta resolução foi utilizada para avaliar as características de liberação de um minério de bauxita metalúrgica e de um rejeito de minério de ferro. A caracterização mineralógica mostrou que o minério de bauxita era composto por 54,5% de gibbsita como mineral contendo alumínio, 39,8% de caulinita como ganga silicatada e 5,7% de hematita, enquanto o rejeito de minério de ferro era constituído por 88,8% de quartzo, 10,4% de hematita e 0,8% de goethita. As análises de liberação foram realizadas em relação à composição (teor) e à textura (superfície exposta), em ambas as perspectivas 2D e 3D, para avaliar o grau do erro estereológico. Para a bauxita, as distribuições de teor em 2D e 3D foram correspondentes quando todas as seções transversais foram consideradas em 2D. No entanto, o grau de exposição da superfície 2D não convergiu para o 3D, devido à perda de informações 3D. No caso do rejeito de minério de ferro, o efeito estereológico foi mais pronunciado na quantificação da exposição superficial. Foi observada uma relação linear entre o teor e o grau de exposição da superfície, bem como entre o tamanho da partícula e a exposição da superfície. Uma comparação dos resultados de métodos automatizados de análise de imagem baseados em MEV e microtomografia de raios-X para o rejeito de minério de ferro evidenciou o fato de que apenas uma técnica 3D seria capaz de representar as características reais de sistemas particulados.

Palavras-chave: microtomografia de raios-X, liberação mineral, erros estereológicos

CAPÍTULO 1

INTRODUÇÃO

1.1 Considerações iniciais e motivação

No processamento de minerais, uma caracterização detalhada de sistemas particulados multifásicos é fundamental para garantir uma separação eficiente dos minerais de interesse (WANG et al, 2018; WILLS e FINCH, 2016). Os pontos de maior interesse são composição química e mineralógica das partículas e a distribuição espacial dos diferentes minerais pelas partículas (FURAT et al, 2018). Uma análise precisa permite que o engenheiro de processos, por exemplo, avalie a melhor rota de concentração e o processo atinja a melhor recuperação metalúrgica possível (WILLS e FINCH, 2016).

Especialmente, a liberação desempenha um papel importante na concentração mineral. Esta pode ser definida como a fração de partículas liberadas de um dado mineral sobre a quantidade total de minério – *grau de liberação* – ou como a distribuição cumulativa de partículas com relação ao seu conteúdo de mineral de interesse – *distribuição de liberação* (UEDA et al, 2018). Sua relevância reside no fato de condicionar o teor máximo possível para uma dada recuperação dos processos de concentração subsequentes (LEISSNER et al, 2013; WILLS e FINCH, 2016; REYES et al, 2018). Além disso, a liberação é obtida, principalmente, por meio de processos de cominuição, que consomem muita energia e são ineficientes. Dessa forma, uma determinação confiável é importante para evitar a sobremoagem, o que, consequentemente, minimiza a energia e os custos necessários para o processamento mineral (WANG et al, 2018; GHOLAMI et al, 2020).

Habitualmente, sistemas automatizados de análise de imagem que se baseiam em observações ao microscópio têm sido usados para obter dados sobre a liberação de minerais. Os mais recentes desenvolvimentos, que combinam Microscopia Eletrônica de Varredura (MEV) e Espectroscopia de Raios-X por Energia Dispersiva (EDS), permitiram a aquisição simultânea de informações morfológicas e composicionais automaticamente, identificando e visualizando um grande número de partículas dentro de tempos de medição aceitáveis. Três tecnologias poderosas que são amplamente utilizadas incluem *Mineral Liberation Analyzer* (MLA), *Quantitative Evaluation of Minerals by*

Scanning Electron Microscopy (QEMSCAN), and *TESCAN Integrated Mineral Analyzer* (TIMA) (REYES et al, 2017).

No entanto, esse tipo de análise leva a um erro estereológico significativo, devido à característica bidimensional intrínseca da técnica. A avaliação da liberação por seções polidas geralmente superestima o grau de liberação, porque as partículas mistas podem parecer liberadas em 2D, enquanto as partículas realmente livres são sempre liberadas em 2D (UEDA et al, 2018; REYES et al, 2018, WANG et al, 2018). Este erro é inevitável e independente de abordagens estatísticas, ou seja, do número de partículas que são levadas em consideração (UEDA et al, 2016). Muitas tentativas têm sido feitas para corrigir esta grande desvantagem da técnica, porém, os modelos geralmente não são satisfatórios, pois dependem da textura do minério e cada um apresenta características próprias. Além disso, as correções para mais de duas fases são bastante insatisfatórias (WANG et al, 2018).

Nesse contexto, a utilização de técnicas tridimensionais e não-destrutivas de imagem, como a microtomografia de raios-X (μCT), surge como um método alternativo para medir a liberação de minerais, eliminando a necessidade de correções estereológicas. Inicialmente limitada a fragmentos mais grosseiros, devido à limitação da resolução espacial, agora é possível adquirir dados tomográficos de alta resolução de sistemas particulados em tempos de varredura curtos. A técnica permite uma visualização 3D rápida, com simples ou nenhuma preparação de amostra, fornecendo informações volumétricas sobre a morfologia dos grãos e distribuição de fases dentro das partículas. Entretanto, uma limitação do método é a impossibilidade de determinar a mineralogia do minério (EVANS et al, 2015; REYES et al, 2018).

A caracterização tridimensional de partículas multifásicas usando μCT tem despertado interesse crescente nas indústrias de processamento mineral e metalurgia extrativa. Neste trabalho, avaliou-se a potencialidade da microtomografia de raios-X para explorar as características de liberação de um rejeito de minério de ferro e de uma bauxita metalúrgica. Modelos de liberação para correções estereológicas não encontraram muita aplicação prática e ainda há a necessidade de coletar mais evidências e dados experimentais em 3D. Há uma carência de trabalhos publicados sobre o assunto e, portanto, mais estudos são necessários para suprir essa lacuna. Nas seções a seguir, os

desenvolvimentos na área ao longo dos anos são discutidos e as contribuições científicas mais recentes apresentadas.

1.2 Objetivos do estudo

1.2.1 Objetivo geral

O objetivo desta tese de doutorado foi medir as características de liberação 3D de partículas minerais por microtomografia de raios-X e avaliar o grau do erro estereológico associado às medições 2D. Para cumprir esta tarefa, um rejeito de minério de ferro e um minério de bauxita metalúrgica, na granulometria empregada na indústria do processamento mineral, foram selecionados e investigados.

1.2.2 Objetivos específicos

1. Realizar a caracterização mineralógica e química das amostras.
2. Obter a distribuição de liberação a partir de dados 3D coletados por meio de microtomografia de raios-X de alta resolução.
3. Obter a distribuição de liberação a partir de dados 2D coletados por meio do *TESCAN Integrated Mineral Analyzer.*
4. Avaliar a magnitude do efeito estereológico comparando os resultados obtidos por análises 2D e 3D.

1.3 Estrutura da tese

Esta tese está dividida em 5 capítulos.

O Capítulo 1 consiste em uma introdução ao assunto, destacando os pontos que motivaram o estudo e os objetivos da tese.

O Capítulo 2 traz uma revisão da literatura. O estado da arte é apresentado neste capítulo, bem como a teoria sobre liberação mineral, tomografia de raios-X, processamento de imagens e técnicas convencionais de caracterização de minerais.

O Capítulo 3 cobre a avaliação da liberação mineral de um minério de bauxita metalúrgica com base em dados 2D e 3D obtidos por tomografia de raios-X. São mostradas as distribuições de liberação baseadas nas características composicionais e texturais do minério e a magnitude do erro estereológico.

Em uma abordagem semelhante, no Capítulo 4, a aplicabilidade da tomografia de raios-X é testada para um rejeito de minério de ferro. Neste capítulo, além das distribuições de liberação 2D e 3D obtidas por tomografia de raios-X, avaliou-se também a liberação mineral aferida pelo *TESCAN Integrated Mineral Analyzer.*

Por fim, o Capítulo 5 resume os resultados e mostra as contribuições do trabalho e sugestões para pesquisas futuras.

CHAPTER 1

INTRODUCTION

1.1 Background and motivation

In mineral processing, a detailed characterization of multiphase particulate systems is fundamental to guarantee an efficient separation of the valuable minerals (WANG et al, 2018; WILLS and FINCH, 2016). The points of major interest are the mineralogical and chemical composition of the particles, and the spatial distribution of different minerals within the particles (FURAT et al, 2018). A precise analysis allows the process engineer, for instance, to evaluate the optimum concentration route and to achieve the best metallurgical recovery possible (WILLS and FINCH, 2016).

Particularly, mineral liberation plays an important role in mineral concentration. It can be expressed as the fraction of the liberated particles of a given mineral over the total amount of it – *degree of liberation* – or, as the cumulative distribution of particles with respect to their content of the mineral of interest – *liberation distribution* (UEDA et al, 2018). Its relevance relies in the fact that it determines the maximum possible grade for a given recovery of downstream processes (LEISSNER et al, 2013; WILLS and FINCH, 2016; REYES et al, 2018). In addition, liberation is mostly achieved by means of comminution processes, which are highly energy-intensive and inefficient. This way, a reliable determination is important to avoid overgrinding, which, as consequence, minimizes the energy and costs required for mineral processing (WANG et al, 2018; GHOLAMI et al, 2020).

Commonly, microscope-based automated image analysis systems are used to obtain data regarding mineral liberation. The latest developments that combine scanning electron microscopy (SEM) and energy-dispersive X-ray spectroscopy (EDS) have enabled simultaneous acquisition of morphological and compositional data automatically, identifying and visualizing a great number of particles within acceptable measurement times. Three powerful technologies that are widely used include Mineral Liberation Analyzer (MLA), Quantitative Evaluation of Minerals by Scanning Electron Microscopy (QEMSCAN), and TESCAN Integrated Mineral Analyzer (TIMA) (REYES et al, 2017).

However, this kind of analysis leads to significant stereological bias due to the intrinsic two-dimensionality characteristic of the technique. The liberation assessment from polished sections generally overestimates the degree of liberation because mixed particles can appear to be liberated in 2D, whereas truly free particles are always liberated in 2D (UEDA et al, 2018; REYES et al, 2018, WANG et al, 2018). This error is unavoidable and independent of statistical approaches, i.e., the number of particles that are taken into consideration (UEDA et al, 2016). There have been many attempts to correct this major drawback, however, it is challenging and the models are usually not satisfactory, since they depend on ore texture and each ore features its own characteristics. Additionally, corrections for more than two phases are fairly unsatisfactory (WANG et al, 2018).

In this context, the usage of non-destructive three-dimensional imaging techniques such as X-ray microtomography (μCT) comes as an alternative method to measure mineral liberation, eliminating the need for stereological corrections. Early limited to coarser fragments due to limitation of spatial resolution, it is now possible to acquire high-resolution tomographic data of packed beds within short scanning times. The technique allows fast 3D visualization, with simple or no sample preparation, readily providing volumetric information concerning grains morphology and phase distribution within the particles. Nevertheless, one limitation of the method is the inability to determine the mineralogy of the ore (EVANS et al, 2015; REYES et al, 2018).

Three-dimensional characterization of multiphase particles using μCT has been of growing interest of mineral processing and extractive metallurgy industries. In this work, it was evaluated the potentiality of X-ray microtomography to explore the characteristics of liberation of an iron ore tailing and a metallurgical bauxite ore. Liberation models for stereological corrections have not found much practical application and there is still the need to collect more evidences and 3D experimental data.

There is a lack of published works on the subject and, therefore, more studies are necessary to fulfill this gap. In the following sections, the developments on the field over the years are discussed and the latest scientific contributions presented.

1.2 Aims of the study

1.2.1 General aim

The aim of this doctoral thesis was to measure the 3D liberation characteristics of mineral particles by X-ray microtomography and to evaluate the degree of stereological errors associated to 2D measurements. To accomplish this task, an iron ore tailing and a metallurgical bauxite ore, in the granulometry employed in the mineral processing industry, were selected and investigated.

1.2.2 Specific aims

1. To perform mineralogical and chemical characterization of the samples.
2. To obtain the liberation distribution from 3D data collected through high-resolution X-ray microtomography.
3. To obtain the liberation distribution from 2D data collected through TESCAN Integrated Mineral Analyzer.
4. To assess the magnitude of stereological bias by comparing the results obtained by 2D and 3D analyses.

1.3 Thesis structure

This thesis is divided into 5 chapters.

Chapter 1 consists of an introduction to the subject, highlighting the points that have motivated the study and the aims of the thesis.

Chapter 2 brings a literature review. The state of the art is presented in this chapter, as well as the theory regarding mineral liberation, X-ray tomography, image processing, and conventional mineral characterization techniques.

Chapter 3 covers the evaluation of mineral liberation of a metallurgical bauxite ore based on 2D and 3D data obtained by X-ray tomography. It is shown the liberation distributions based on compositional and textural characteristics of the ore, and the magnitude of stereological bias.

In a similar approach, in Chapter 4, the applicability of X-ray tomography is tested for an iron ore tailing. In this chapter, besides the 2D and 3D liberation distributions

obtained by X-ray microtomography, it was also evaluated liberation measured through TESCAN Integrated Mineral Analyzer.

Finally, Chapter 5 summarizes the results and shows the contributions of the work and suggestions for further research.

References

EVANS, C.L. et al. Quantifying mineral grain size distributions for process modelling using X-ray micro-tomography. **Minerals Engineering** 82, 78–83, 2015.

FURAT, O. et al. Description of Ore Particles from X-Ray Microtomography (XMT) Images, Supported by Scanning Electron Microscope (SEM)-Based Image Analysis. **Microsc Microanal.**, 2018.

GHOLAMI, H. et al. The effect of microwave's location in a comminution circuit on improving grindability of a porphyry copper deposit. **Energy Sources A**, 2020.

LEISSNER, T. et al. Evaluation of mineral processing by assessment of liberation and upgrading. **Minerals Engineering** 53, 171–173, 2013.

REYES, F. et al. Calibrated X-ray micro-tomography for mineral ore quantification. **Minerals Engineering** 110, 122–130, 2017.

REYES, F. et al. Quantifying mineral liberation by particle grade and surface exposure using X-ray microCT. **Minerals Engineering** 125, 75–82, 2018.

UEDA, T. et al. Statistical effect of sampling particle number on mineral liberation assessment. **Minerals Engineering** 98, 204–212, 2016.

UEDA, T. et al. Experimental analysis of mineral liberation and stereological bias based on X-ray computed tomography and artificial binary particles. **Advanced Powder Technology** 29, 462–470, 2018.

WANG, Y. et al. Stereological correction of perimeter-based estimates of exposed grain surface area. **Minerals Engineering** 126, 64–73, 2018.

WILLS, B.A., FINCH, J.A. **Will's Mineral Processing Technology**. 8ed. Elsevier, Oxford, 2016.

CHAPTER 2

LITERATURE REVIEW

2.1 State of the art

Gaudin, in 1939, was the first researcher to report a mineral liberation model; described as the percentage of a phase occurring as free particles, in relation to the total amount of that given phase in all particles. He was the first one as well to point out the existence of stereological bias of the degree of liberation (GAUDIN, 1939; WANG et al, 2017). Following this, many researchers have attempted to correct this intrinsic error.

Miller and Lin (1988) used computer simulation to estimate mineral liberation from one or two-dimensional information obtained by image analysis of polished sections. They presented a transformation matrix that expressed the relationship between one, two, and three-dimensional data. However, the implementation of the matrix was limited to a certain particle grade. King and Schneider (1998) developed a work with similar approach, but for real mineralogical particles. The method presented by the authors, however, required narrow grade and narrow size distribution.

Fandrich et al (1998) proposed two stereological correction methods: allocation method and kernel transformation method. The former was based on theoretical geometrical equations and the latter on direct texture measurement. The two approaches were tested for real ores and, although both demonstrated positive results, they were only valid when applied to binary systems. Gay (1994), in his PhD thesis, suggested nine stereological equations to correlate 2D and 3D attributes.

Leigh et al (1996) studied the Barbery's liberation model, a statistical model based on particle shape and texture, to deduce three-dimensional information from 1D and 2D data. Recently, Zhang and Subasinghe (2013) suggested modifications in this model, removing the ore texture assumption and introducing a new method of quantifying the amount of fully liberated particles. The model, however, fails for very fine sizes where the errors due to sample preparation become significant.

Van der Wielen and Rollinson (2016), using a free image analysis software solution, proposed a method based on mathematical tools to represent fragmentation patterns. The patterns were superimposed onto mineral images and liberation spectra

produced. Nonetheless, the authors pointed out that more experimental validation was required.

A profound discussion on mathematical modelling of mineral liberation is beyond the scope of this thesis. The abovementioned works are only some relevant examples to illustrate the applications and limitations of models for stereological correction developed over the years. Other studies that are worth highlighting include Guimarães and Durão (2003, 2007), Evans and Napier-Munn (2013), Mariano and Evans (2015), Lotter et al (2018), Wiegel (2006, 2011), and Ueda et al (2017).

X-ray microtomography (μCT) has been explored for the last few decades to surpass the problematic of stereological bias. This imaging method can non-invasively, non-destructively, and three-dimensionally examine the morphology of particles that constitute complex particulate systems with spatial resolution down to 1μm (STARON et al, 2017).

Pioneers in this approach, Lin and Miller (1996) performed tomographic investigations to determine the liberation spectrum of dolomite/sphalerite particles. Although the spatial resolution achieved by the experiments was not sufficient to carry out deep investigations, due to equipment limitations back then, their work anticipated the potential of implementation of μCT to overcome the limitations of polished sections analysis. The authors provided a detailed explanation of the microtomograph setup, scanning procedure, and image analysis.

Following, Lin, Miller and their colleagues have published many papers on this subject. In 2002, they wrote about the latest developments of microfocus X-ray generation, which increased the potential of the technique in mineral processing studies (LIN and MILLER, 2002). In 2005, they measured, characterized, and analyzed particle shape using μCT (LIN and MILLER, 2005). They have also evaluated the liberation-limited grade/recovery curves from tomographic images to predict separation efficiency of phosphate rock by flotation (MILLER et al, 2009).

Gay and Morrison (2006) is another great early contribution to the field. A well-characterized ore sample was subjected to 2D imaging through polished sections to estimate 3D properties. The results were then compared to 3D information obtained by μCT to validate the model proposed.

Even though μCT technique has been available for the last decades, only recently advanced instrumentation and improved software functionalities have allowed more detailed analysis of particulate systems. It is now possible to perform high-resolution X-ray microtomography with suitable spatial resolution in shorter acquisition times. Additionally, the processing capacity of modern computers has enabled to deal with larger data in faster manners with enhanced quality.

Wang et al (2018) investigated a copper ore containing valuable minerals such as pyrite, chalcopyrite and molybdenite, with gangue minerals composed mainly by quartz and potash feldspar. Particles were scanned at a voxel size of 5.19μm, varying between 5,000 and 13,000 particles analyzed per scan. The ore was also analyzed by MLA and a comparison of 2D perimeter-based liberation with 3D mineral liberation by exposed surface reported. The results indicated that liberation was overestimated in 2D analysis and that perimeter-based grain exposure distribution is similar to the volume grade distribution. The article has also brought important highlights of image analysis procedures, delineating a precise description of the tools implemented in the investigation. However, the particle size analyzed (approximately, 417μm) was not compatible to mineral processing operations.

In a different work, Wang et al (2017) performed X-ray microtomography to assess liberation and exposed grain surface of an auriferous pyrite ore for flotation. Concentrate and tailing samples of 500x850μm size class were scanned at 4.59μm pixel size. They showed the procedures of pre-processing and corrections of the images, as well as the use of an algorithm for determination of exposed grain surface area. The authors found out that a minimum exposed surface area percentage of 1.5% was required for recovery in the flotation system utilized. Moreover, they discussed how the mineral arrangement in the particle impacts the flotation efficiency. Particles with fine and widely distributed grains would have an inferior flotation performance in comparison to particles having the same percentage of exposed area, but with one or more large exposed grains

for bubble attachment. Similar to the previous work, the particle size was not in agreement with the practice of mineral beneficiation.

Reyes et al (2017) developed a methodology that combined μCT and SEM images in order to obtain more detailed information on mineral characterization. For this, the authors scanned fragments of copper sulphide ore of about 8 to 12mm of size, achieving a spatial resolution of 8.9 and 16.1μm. The particles were also analyzed using a SEM-EDS system. The method made use of a track algorithm that matched both imaging modalities at a grain level, readily providing properties such as mineralogy, mineral liberation, grain size, and texture characteristics. The size of the fragments studied, though, was greater than the size practiced in mineral processing.

Reyes et al (2018) tested the application of μCT on low grade porphyry copper ore containing chalcopyrite, pyrite, and siliceous gangue, representative of the commonly treated ore for copper production. The samples displayed granulometry in 4 size classes: 53-75μm, 75-90μm, 90-150μm, and 150-220μm. In their work, more than 20,000 particles were analyzed, with a resolution of 6.21 and 2.01μm. Liberation in terms of grade and surface exposure was calculated in 2D and 3D. In the case of grade, the results show that the finer the fragments, the more liberated material was found, as expected. When it comes to surface exposure, even considering every possible slice of each particle in 2D, two-dimensional data did not converge to the 3D surface exposure. The results showed advances in the application of μCT for particles in the size range of mineral beneficiation, but for virtually binary and simple particles.

Evans et al (2015), inspired by advances in modelling of mineral liberation, developed a method that used μCT to acquire 3D information regarding grain size distribution and spatial location of the minerals in an ore. To achieve this, the authors chose a gold-bearing pyrite ore of simple mineralogy with fragments varying in dimension from 4.75 to 6.70mm, scanned at a resolution of 5.0μm voxel size. Coupled to images and mineralogy information obtained from MLA, the data collected exhibited vast applicability to model and simulate mineral liberation in comminution. The results also provided an opportunity to estimate the magnitude of the discrepancy between grain size distributions measured in 2D and 3D, being finer when evaluated from 2D data.

Ueda et al (2018) prepared artificial binary particles by dispersing silica sand or glass beads through a matrix of epoxy resin or Portland cement. They proposed a method for stereological correction based on 2D and 3D attributes of the particles acquired by μCT, and tested to 16 samples with various internal structure. The authors were able to reduce approximately 60.5% of the stereological bias via the correction. In a different word, Ueda (2019) proved the statistical reliability of the approach. However, the method is limited to particles containing two phases and still needs to be validated for real mineral particles.

2.2 Brief description of the mineral ores

2.2.1 Iron ore

About 98% of all iron ore extracted is used in steel industries, which makes it vital to maintain a solid industrial base (USGS, 2019a). Steel is the most consumed metal alloy in the world (SHETTIMA et al, 2016).

During the ore genesis, iron formations have undergone to intense mineralogical alterations and texture modifications, making it possible for iron ore to exhibit a vast diversity of configurations. The most common iron ores occur in the form of hematite (α-Fe_2O_3), magnetite (Fe_3O_4), and goethite (α-FeOOH), with gangue mostly composed by quartz (SiO_2) (KLEIN and HURLBUT, 1985). Table 2.1 brings the main characteristics of the minerals commonly found in iron ore.

Table 2.1. Description of the main mineral phases found in iron ore. Source: KLEIN and HURLBUT, 1985.

Mineral	**Hematite**	**Magnetite**	**Goethite**
Chemical formula	α-Fe_2O_3	Fe_3O_4	α-FeOOH
Chemical classification	Oxide	Oxide	Oxyhydroxide
Crystal system	Trigonal	Isometric	Orthorhombic
Mohs hardness	5.5-6.5	5.0-6.5	5.0-5.5
Density (g/cm^3)	5.0-5.3	5.2	3.3-4.3

World's proven iron ore reserves account for 170 billion tons and, although it is mined in about fifty countries, the seven largest producing countries are responsible for about three-quarters of total world production. For instance, Australia and Brazil together

dominate two-thirds of total exports. In 2017, 2.4 billion tons were produced worldwide (JESUS and JOAQUIM, 2018; USGS, 2019a).

The largest reserves in Brazil are located in Minas Gerais (74.4%), Pará (19.5%), and Mato Grosso do Sul (2.2%). The average Brazilian ore grade is 46.2% of iron, varying from about 40%, as in the case of Minas Gerais, up to 66%, as in the case of Pará (JESUS and JOAQUIM, 2018).

Froth flotation is the most common separation method implemented to concentrate iron ore at fine size classes (<150μm). There are different flotation routes when the gangue mineral is quartz: cationic reverse flotation of quartz, anionic direct flotation of iron oxides, and anionic reverse flotation of activated quartz. Independently of the route selected, iron oxides must be as liberated as possible from quartz to guarantee an efficient flotation. Preliminary steps may include: crushing, grinding, mineral attrition, and wet classification. Magnetic separation comes as an alternative method if magnetite is abundant (ARAUJO et al, 2013).

Each year, more than 10 billion tons of iron ore tailings and barren rock are discharged in the world (YU et al, 2018). The crescent demand for iron worldwide resulted in the mining of ores with lower iron contents, contributing even more to the amount of waste produced after mineral processing operations (MAGALHÃES et al, 2020). The disposal of mining tailings in dams has received extra attention in the past years, as it represents a threat to the ecological environment and to the social welfare (SUN et al, 2020).

Stimulated by this scenario, researchers have been exploring the conversion of sandy tailings into value-added products, such as geopolymers and pigmented cements, as well as additional iron recovery, as it implies sustainable mining with environmental, social, and economic outcomes (ALMEIDA and SCHNEIDER, 2020; SUN et al, 2020).

2.2.2 Bauxite ore

Bauxite ore is the primary source of aluminum metal and its oxides, which is the third-most common element in Earth's crust, after oxygen and silicon (SAMPAIO et al, 2008). Additionally, bauxite is the third largest mineral resource in Brazil, after aggregates for construction and iron ore. On a global scale, Brazil also ranks third in production, behind China and Australia (USGS, 2019b). The ore finds applications that go from production of metallic aluminum to abrasive materials, refractory products, chemicals, high alumina cements, and orthopedic prosthesis, among others (SAMPAIO et al, 2008).

The ore consists of an impure mixture of aluminum minerals, known as aluminum oxyhydroxides. The most significant minerals are gibbsite ($Al(OH)_3$), boehmite (AlO(OH)), and diaspore (AlO(OH)). The proportions of these minerals in the rock vary widely between deposits, as well the type and amount of impurities, for instance: hematite (Fe_2O_3), goethite (FeO(OH)), kaolinite ($Al_4(Si_4O_{10})(OH)_8$), quartz (SiO_2), rutile (TiO_2), and anatase (TiO_2). It is said metallurgical bauxite if the ore presents a great proportion of gibbsite and non-metallurgical if a great proportion of diaspore is found (SAMPAIO et al, 2008). Table 2.2 brings the main characteristics of the aluminum minerals and Table 2.3 the typical composition of the metallurgical and the non-metallurgical bauxite.

Table 2.2. Description of the main mineral phases found in bauxite. Source: KLEIN and HURLBUT, 1985.

Mineral	**Gibbsite**	**Boehmite**	**Diaspore**
Chemical formula	$Al(OH)_3$ - γ	AlO(OH) - γ	AlO(OH) - α
Al_2O_3:H_2O	1:3	1:1	1:1
Crystal system	Monoclinic	Orthorhombic	Orthorhombic
Mohs hardness	2.5-3.5	3.5-4.0	6.5-7.0
Density (g/cm^3)	2.42	3.01	3.44
Dehydration temperature (ºC)	150	350	450
Product of dehydration	Al_2O_3 - χ	Al_2O_3 - γ	Al_2O_3 - α
Solubility (g Al_2O_3/L)(*)	128	54	Insoluble

(*) In Na_2O solution, 100g/L, 125ºC

Table 2.3. Typical composition of the non-metallurgical and metallurgical bauxite. Source: HABASHI, 1993.

Non-metallurgical bauxite		**Metallurgical bauxite**	
Phase	**Composition (%)**	**Phase**	**Composition (%)**
Fe_2O_3	2.5 (max)	Fe_2O_3	11 - 12
SiO_2	5 – 7	SiO_2	< 4.0
Al_2O_3	50	Al_2O_3	> 48

The essential condition for the formation of bauxite is the existence of a tropical to subtropical climate, with an average annual temperature above 20ºC. The alternance between dry and humid seasons favors the weathering process. Thus, the main reserves are located in countries such as Brazil, Jamaica, Australia, Guinea, India, and China. Due to the weathering mechanism, bauxite has a reddish color (more or less intense depending, respectively, on the more or less occurrence of iron oxide) (SAMPAIO et al, 2008, ABAL, 2018).

According to the U.S. Geological Survey (2019b), Guinea, Australia, Brazil, Vietnam, and Jamaica hold over 70% of the world's bauxite reserves. It is estimated 55 billion to 75 billion tons of ore distributed in Africa (32%), Oceania (23%), South America and the Caribbean (21%), Asia (18%), and elsewhere (6%).

In Brazil, 91% of the reserves are located in the state of Pará - when added to Minas Gerais reserves, they make up 98.3% of the total. About 95% of Brazil's bauxite correspond to metallurgical bauxite, which is of excellent quality (more than 40% of Al_2O_3) (ABAL, 2018).

Bauxite ores can be categorized into two classes: lateritic and nodular. Nodular bauxite exhibits a complex structure and contains substantial amounts of impurities, such as kaolinite and hematite, which grades may reach 14.5% and 16.3%, respectively (COSTA, 2016). The presence of these impurities impacts negatively the performance of Bayer process, as they react with other components of the process and cause loss of alumina and sodium hydroxide (feedstock of Bayer process). As a consequence, currently, nodular bauxite is not economic viable (NOVO et al, 2015).

2.2.2.1 Bayer process

The Bayer process aims to produce alumina, which can afterwards be transformed into metallic aluminum by means of Hall-Héroult process (SAMPAIO et al, 2008).

In the Bayer process, bauxite ore (<208μm) is heated in pressure reactors of about 5m x 30m along with sodium hydroxide at a temperature varying from 150 to 200ºC and pressure between 4.0 to 8.0atm. The solubility of Al^{3+} in water is very low, but increases considerably at either high or low pH. At these conditions, the aluminum is dissolved as sodium aluminate in an extraction process, while the impurities remain in the solid state and are known as red mud (HIND et al, 1999; SAMPAIO et al, 2008).

The chemical equation governing the dissolution of gibbsite, the most common aluminum oxide found in Brazil, into sodium aluminate is elucidated by Equation 2.1 (SAMPAIO et al, 2008).

$$Al_2O_3N.3H_2O + 2NaOH \Leftrightarrow 2NaAlO_2 + 4H_2O \quad (2.1)$$

The treatment also dissolves silica from kaolinite, which only implies in higher consumption of caustic soda and no contribution to alumina production. Hence, it is necessary to have an Available aluminum/Reactive silica (AA/RS) mass ratio higher than 10, or Bayer process will not be economic viable (HIND et al, 1999; SAMPAIO et al, 2008).

After filtration to remove the red mud, the residual liquid is cooled and alumina is crystallized. At the precipitation stage, aluminum hydroxide crystals at fine sizes (“seeds”) are introduced, or crystallization would take several days. Following, the product is filtered, washed, dried, and calcinated to form pure alumina (SAMPAIO et al, 2008). A schematic representation of Bayer process is shown in Figure 2.1.

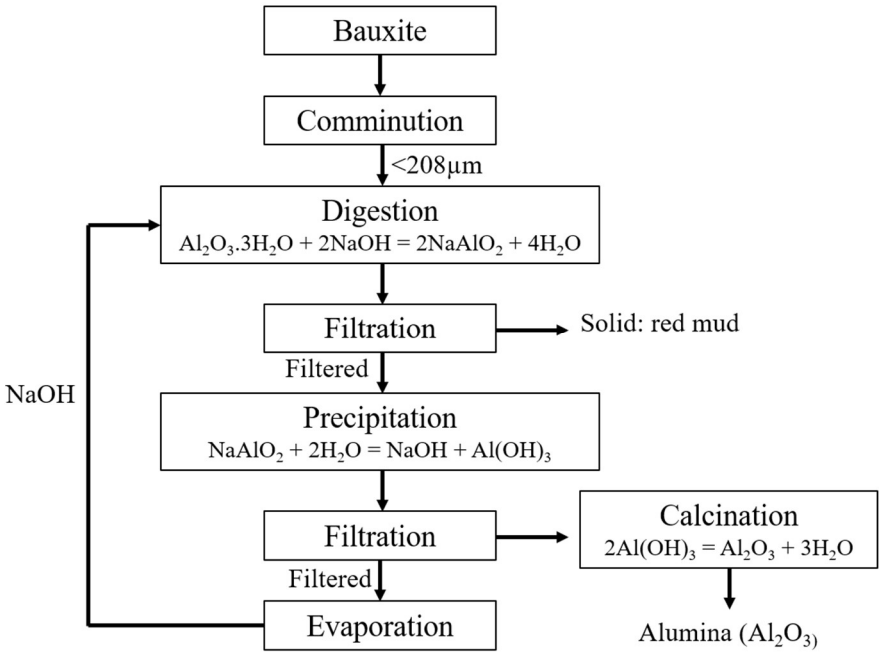

Figure 2.1. Bayer process of alumina production. Source: Adapted from SAMPAIO et al, 2008.

2.2.2.2 Mineral beneficiation of bauxite

The specifications of non-metallurgical bauxite, for example for refractory and chemical industry, demand low content of iron and alkalis. The most common separation method applied is magnetic separation with field intensity higher than 1.5T (15,000G). The ore is crushed and grinded to reduce particle size to a suitable size and to achieve mineral liberation, which is, in general, 74µm. Mineral attrition and wet classification are employed to eliminate fine particles. Following, magnetic separation is performed to remove Fe_2O_3 and TiO_2. The next and final steps are: dewatering (filtration), drying, calcination, and ore transportation and storage (SAMPAIO et al, 2008). Alternatively, gravity concentration and dense medium separation may be applied as concentration methods in some cases (CHAVES et al, 2013).

On the other hand, the processing of metallurgical bauxite includes more stages. Sometimes it is desirable to enhance the AA/RS ratio by means of physical and physical-chemical techniques of mineral processing prior to Bayer process. In the following paragraphs, it will be described the mineral processing operations that take place in three different beneficiation plants in Brazil (Mineração Rio do Norte, Mineração Bauxita Paragominas, and Mineração Miraí), as synthesized by Van Deursen (2016).

Mineração Rio do Norte is a bauxite mine in Pará, Brazil. The primary and secondary crushing are performed by sizers and impact crushers, located close to the mine front. The products from the crushers are transported by belt conveyors and feed scrubbers, where bauxite is disaggregated. Following, the ore finds a trommel and two products are generated: the coarse fraction, that is redirected to tertiary crushing; and the fine fraction, which feeds a screen (along with the product of the tertiary crusher). The retained fraction from screening is the final product and the passing fraction is directed to cyclones, where bauxite is separated from the gangue minerals. The dewatering of the fine bauxite is performed by horizontal belt filters (VAN DEURSEN, 2016).

In *Mineração Bauxita Paragominas*, also located in the State of Pará, after the primary and secondary crushing, the ore is homogenized and headed to semi-autogenous grinding (SAG) mills. The discharge of the SAG mills is screened: The retained fraction feeds an impact crusher and the passing fraction is classified. The product of the crusher and the underflow of the cyclone are directed to ball mills, in which their discharges, after thickening, consist in the final product (VAN DEURSEN, 2016).

In the case of *Mineração Miraí*, in Minas Gerais, the ore is crushed by primary and secondary crushers and scrubbed with water for disaggregation. The discharge of the scrubbers is screened in two stages: 6.35mm and 0.85mm. The retained fraction of the secondary screening is final product and the passing fraction is tailing (VAN DEURSEN, 2016).

Although the described operations have been used successfully in Brazil, the depletion of high-quality ore has been demanding the investigation of new concentration strategies to increase the AA/RS ratio. Due its versatility, froth flotation has been a potential candidate.

2.3 Mineral liberation

Liberation of a certain mineral from its gangue is achieved mostly through comminution, which includes crushing and grinding until a size reduction where valuable minerals and gangue minerals co-exist as liberated or free particles. Ideally, liberation ought to occur at the coarsest possible particle size. If this objective is accomplished, energy is saved not only in comminution process, but also in any subsequent separation stages, as the amount of fines produced is reduced and the operations become easier to

operate (WILLS and FINCH, 2016). It is important to emphasize that grinding is one of the most extensively used unit operation, but the most inefficient as well, consuming up to 50% of the total electrical energy expended in a concentration plant (BOBICKI et al, 2018; GHOLAMI et al, 2020).

Frequently, liberation is expressed as degree of liberation or liberation distribution. The former, formulated by Gaudin in 1939, is the fraction of liberated particles of a specified mineral over the total amount of particles. The latter expresses a cumulative distribution of particles with respect to their content of the mineral of interest (UEDA et al, 2018). From the cumulative distribution, also acknowledged as liberation spectrum, it is possible to quantify the amount of liberated minerals, as well as the amount of mixed particles (NEUMANN et al, 2010). In the specific case of flotation, liberation is considered to be surface liberation, due to the dependence of the operation performance on the achieved surface exposure of the floatable minerals (WILLS and FINCH, 2016; REYES et al, 2018).

It is often necessary to grind the ore to a size down to 100μm to obtain clean concentrates with little contamination. This number, however, depends on each ore. If high-grade solid products are required for downstream processes, then good liberation is essential and finer size classes may be need. On the other hand, a high degree of liberation is not always necessary. As an example, there are cases in which it is possible to achieve a high recovery of magnetite by magnetic separation even if it is completely enclosed by quartz, and hence presents a degree of liberation zero (WILLS and FINCH, 2016).

In practice, complete liberation is rarely achieved, rather generating particles of mixed composition between mineral and gangue, known as middlings. The performance of liberation achievement depends upon characteristics as hardness, cleavability, and particle features in general, such as grain arrangement, crystal cohesion, crystal morphology, porosity, and pre-existence of zones of natural weakness (PORPHÍRIO et al, 2010). For instance, liberation can be high if there are weak boundaries between the species that compose the ore, as in the case of sedimentary minerals – this mechanism is often referred to as liberation by detachment. The most common scenario, however, is a strong adhesion between mineral and gangue, and, during comminution, the breakage is

random. Under these circumstances, a significant amount of middlings is produced (WILLS and FINCH, 2016).

To illustrate the impact of ore texture in mineral liberation, Figure 2.2 brings micrographs showing variation in ore texture, with structure complexity increasing from simple to fine-grained inter-grown texture. Strongly reliant on the texture, different fragments can be formed, from fully liberated mineral and gangue particles, as schematic shown in Figure 2.3. Particles of type 1 are high-grade and can be classified as concentrate, as they carry a low content of locked gangue. At the other extremity, particles of type 4 would be classified as tailings. Particles of type 2 and 3 are considered middlings and may require additional regrinding to promote mineral liberation.

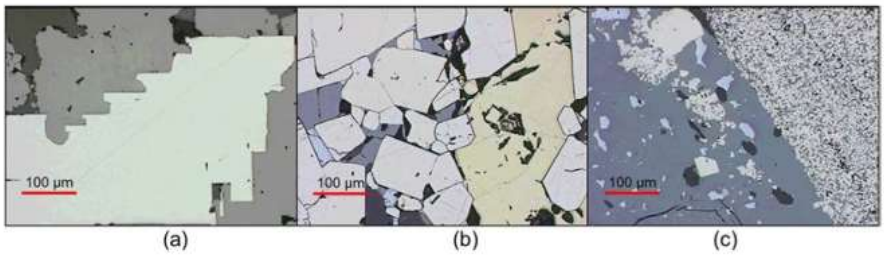

Figure 2.2. Micrographs of (a) galena/sphalerite, (b) sphalerite/chalcopyrite, and (c) galena/sphalerite/pyrite. Source: WILLS and FINCH, 2016.

Figure 2.3. Different products of comminution exhibiting different liberation patterns Source: WILLS and FINCH, 2016.

Over the years, many researchers have attempted to create models of the degree of liberation. Even though some approaches have demonstrated to be useful for some specific applications (as discussed in Chapter 1), liberation models have not found much generalized practical use. The main issue relies on the fact that these models make unrealistic assumptions with respect to the grain structure of the minerals in the ore (WILLS and FINCH, 2016). They usually require knowledge of grain shape, often erroneously assumed to be spherical or ellipsoidal (REYES et al, 2017).

Gaudin was a pioneer of the study of mineral liberation. In 1939, he proposed a simple liberation model based on random breakage and its predictions is presented in Figure 2.4. The degree of liberation of the least abundant mineral is given as a function of the particle size to grain size ratio. For example, to achieve 75% of mineral liberation, the particle size has to be 10 times smaller than the grain size – if the grain size is 1mm, then size reduction must produce a particle size at least 0.1mm or less. Gaudin's model points out something very intuitive and of extreme relevance: the finer the size of the particle obtained, the more liberated the ore is (GAUDIN, 1939; WILLS and FINCH, 2016).

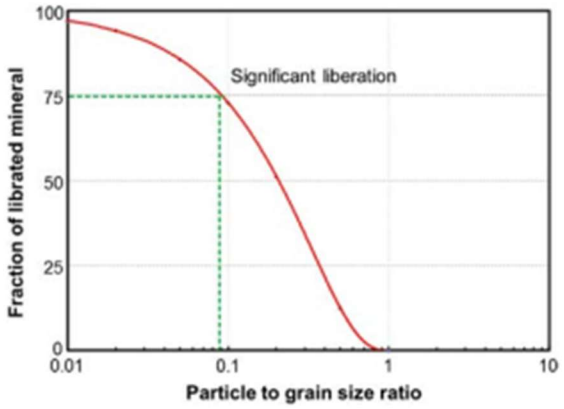

Figure 2.4. Degree of liberation for the least abundant mineral as a function of the particle to grain ratio. Source: WILLS and FINCH, 2016.

2.3.1 Liberation-limited grade recovery

Liberation plays an important key in mineral concentration, as it determines the maximum possible grade for a given recovery of separation stages. Grade can be defined as the content of the mineral of interest in the feed or in the concentrate (or any other stream). Recovery refers to percentage of the total mineral contained in the ore that is recovered into the concentrate (WILLS and FINCH, 2016).

The grade of concentrate and recovery are the most usual measures of metallurgical efficiency, and they are generally inversely related: as recovery increases, grade decreases and vice versa. For instance, if high recovery is aimed, there will be more gangue in the concentrate and the grade of concentrate will decrease.

The concentration is limited by the composition of the particles and this explains the inverse relationship between grade and recovery. To elucidate the impact of particle composition, i.e., mineral liberation, consider the particles illustrated in Figure 2.5 undergoing an ideal separation process (a separator that recovers particles sequentially based on valuable mineral content).

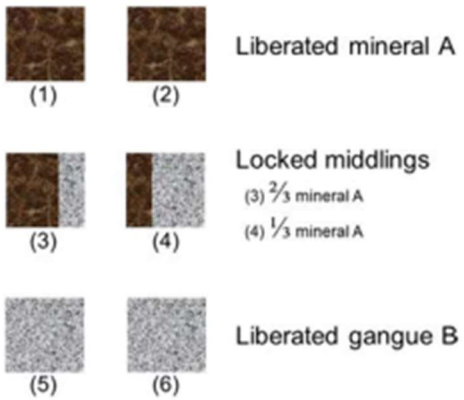

Figure 2.5. Examples of particles fed to a perfect separator. Source: WILLS and FINCH, 2016.

The particles represent three mineral (A) equivalents and three gangue (B) equivalents, and would be recovered in order 1 through 6. The grade and recovery of A after each particle is separated into the concentrate are given in Table 2.4.

Table 2.4. Recovery of the particles illustrated in Figure 2.4 by an ideal separator. Source: Adapted from WILLS and FINCH, 2016.

Particle recovered	**1**	**2**	**3**	**4**	**5**	**6**
Concentrate grade (%)	100	100	89	75	60	50
Recovery (%)	33	66	89	100	100	100

The grade-recovery corresponding to optimum efficiency is known as the mineralogically-limited or liberation-limited grade-recovery, and it is the most common representation of metallurgical performance. It can be obtained from mineralogical data followed by adequate calculations. It is used, for example, to compare against the actual operation and take actions to improve separation effectiveness. By way of illustration, in Figure 2.6, it was compared the liberation-limited curve for two rare earth element deposits determined by mineralogical analysis (MIN) with actual metallurgical test results (MET). In the case of C-2 ore, the metallurgical result approached the predicted by mineralogical analysis. The same did not happen for C-1 (WILLS and FINCH, 2016).

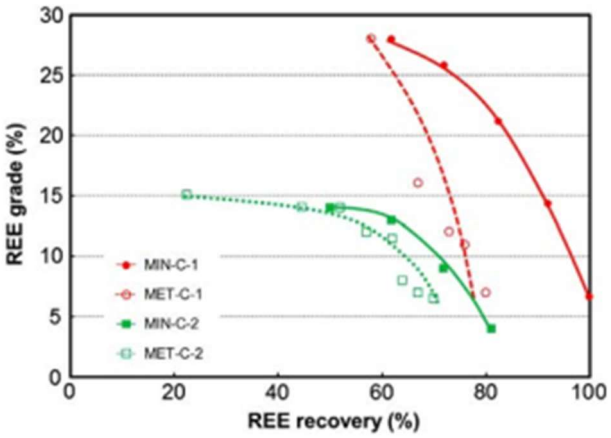

Figure 2.6. Liberation-limited curve calculated from mineralogical analysis (MIN) and compared to actual metallurgical performance (MET) for rare earth ores. Source: WILLS and FINCH, 2016.

2.3.2 Conventional methods of liberation assessment

According to Neumann et al (2010), image analysis is one of the oldest methods of phase quantification and liberation assessment. In the early times, the measurements relied upon images produced by transmitted and reflected light microscopes, and posterior counting of the number of liberated particles. One approach, known as Gaudin's method, consists of a systematic counting of mineral particles, one by one, recording the number of free particles of a given phase and the number of mixed particles. Then, the degree of liberation is calculated by dividing the number of liberated particles by the total amount of counted particles. It is a very time-consuming activity and, even if thousands of particles are taken into consideration, the results are just an indicative of the liberation condition of the ore (NEUMANN et al, 2010; WILLS and FINCH, 2016).

Rather than just calculating the degree of liberation, it is more useable and find more practical applications to measure the liberation spectrum (the cumulative distribution of particles with respect to their content of the mineral of interest). Currently, scanning electron microscopy-based (SEM-based) measurements are the most reliable and widely used technique to accomplish this task (NEUMANN et al, 2010; REYES et al, 2017). The images, often obtained from detected backscattered electrons, exhibit an atomic number contrast, where the gray-scale of each pixel is proportional to the average atomic weight of the mineral phase present at that position. With appropriate computer programs and additional mineralogical information derived from supplementary characterization techniques, an accurate and quick analysis is performed and the liberation distribution is produced (NEUMANN et al, 2010).

Advances in instrumentation for materials characterization have permitted to perform this task automatically, by combining scanning electron microscopy and energy-dispersive X-ray spectroscopy (SEM-EDS). This sort of system enables simultaneous acquisition of morphological and compositional data automatically, readily providing mineral liberation, grade, surface exposure, porosity, and other features of the ore analyzed. Mineral Liberation Analyzer (MLA), Quantitative Evaluation of Minerals by Scanning Electron Microscopy (QEMSCAN), and TESCAN Integrated Mineral Analyzer (TIMA) are examples of SEM-EDS-based systems. A description of TIMA system will be presented in the following sections.

To construct the liberation distribution, particles are classified into groups based on mineral of interest area percentage. Conventionally, 12 classes are employed: 0%, 0-10%, 10-20%, 20-30%, continuing consecutively with increments of 10% until the maximum class, corresponding to 100%. The area is calculated by counting the number of pixels corresponding to each phase (based on gray-levels) (NEUMANN et al, 2010; WILLS and FINCH, 2016).

As discussed in Chapter 1, the main disadvantage of image analysis for ore quantification is to measure volumetric distributions from 2D data obtained from polished sections – there is an intrinsic loss of information. For instance, locked particles may seem to be liberated depending on the location where the sample is sectioned, meaning the degree of liberation is overestimated. There have been many attempts to correct the

stereological bias of image analysis, but, in practical terms, no corrections are usually made (WILLS and FINCH, 2016).

As instrumentation advances and the technique becomes more accessible, X-ray microtomography has emerged as a solution to directly measure volumetric attributes of mineral particles and to overcome the stereological errors issues. A detailed elucidation of the technique is offered in the next sections.

Other methods that have been falling into disuse include dense medium separation, due to the high toxicity of the liquids required to examine metal sulfides and oxides; and separation using colloidal suspensions of ferromagnetic particles, which presents an operation principle similar to dense medium separation (NEUMANN et al, 2010). A description of these techniques is beyond the purpose of this work.

2.4 Principles of X-ray tomography

X-ray computed microtomography (μCT) has become a very important three-dimensional characterization method for non-destructive analysis, capable of evaluating material microstructure at a micron-level spatial resolution (LANDIS and KEANE, 2010; ASGHAR et al, 2015).

From a mathematical point of view, the technique has its roots in the work of Radon in 1917, who described that it was possible to obtain 2D images from a series of tomographic projections (this will be further explained in the next sections). Based on his theory, in 1957 the first tomographic images were produced. However, most early applications of tomography were for medical imaging purposes. It was only after the improvements in area detectors and processing/storage capacity of computers, that X-ray tomography became available for industrial applications, in the late 80s. Over the years, lab-based (or conventional) scanners' instrumentation continued to develop. Advances in the geometry of the X-ray beams (the emerging of microfocus sources, for example) and in the detection systems (for instance, the substitution of flat panel detectors for CCD cameras) have allowed us to reach spatial resolution (SR) down to 1μm. Concomitantly, improvements in synchrotron radiation sources have led to significant developments in microtomographic imaging as well, due to the high-flux and parallelism of the radiation. Nowadays, it is possible to achieve 3D images at the nanoscale with synchrotron sources

(STOCK, 1999; LIN and MILLER, 2002; BARUCHEL et al, 2000; LANDIS and KEANE, 2010; LEE et al, 2018; ZAMBRANO et al, 2021). Figure 2.7 summarizes the brief evolution of X-ray microtomography through time.

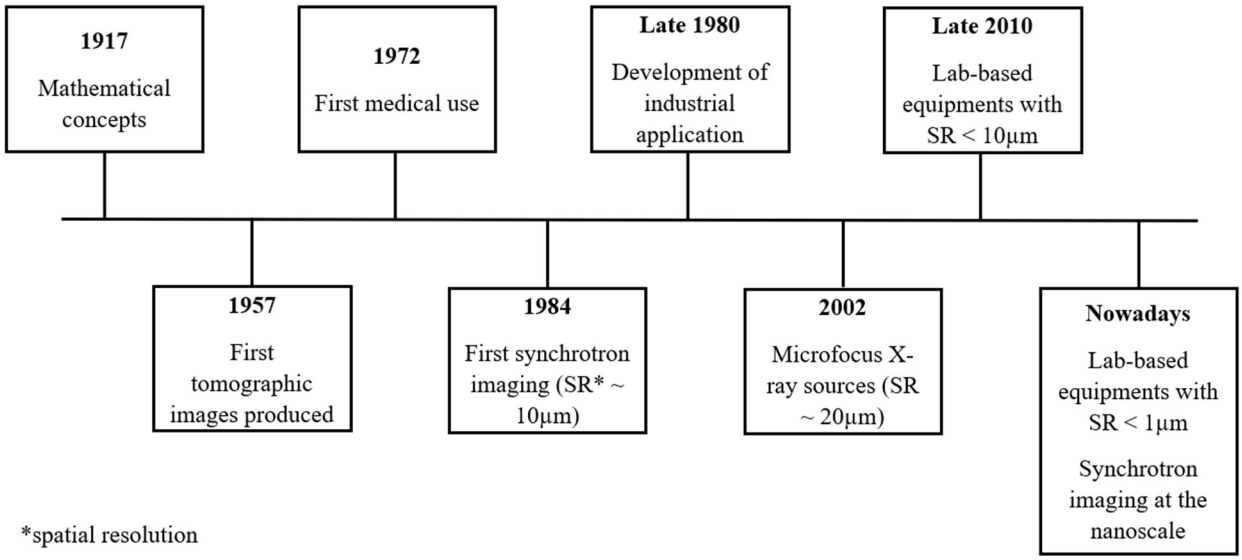

Figure 2.7. The evolution of X-ray microtomography through time. Source: Created by the author based on STOCK, 1999; LIN and MILLER, 2002; BARUCHEL et al, 2000; LANDIS and KEANE, 2010; LEE et al, 2018; and ZAMBRANO et al, 2021.

In tomographic imaging measurement, a specimen is located on a rotation station between the illuminating source and the detector. As it rotates, a series of projection images are recorded and, by mathematical principles of tomography, they are reconstructed (KAK and SLANEY, 2001). Tomography is based on either absorption- or phase-contrast (MOMOSE, 2005). As the focus of this thesis is the absorption modality, this will be the one covered. A more detailed mathematical introduction is featured as it follows.

2.4.1 Mathematical introduction

During the scan, the object is portioned into slices, where each slice, of finite thickness Δz, describes a 2D function of the position-dependent attenuation coefficient μ = μ(x,y). The measurements are taken under equidistant angles from 0º to 180º (or 360º) and the projections $P_\theta(t)$, i.e., the transmitted intensity of the beam as a function of the translation t, are recorded (TREIMER, 2017).

If it is considered a parallel beam, the transmitted intensity I is given by Lambert's law as:

$$I(x,y) = I_0\left(-\int_{path}\mu(x,y)ds\right) \tag{2.2}$$

where I_0 is the intensity of the incident beam (KAK and SLANEY, 2001).

Moreover, the projections can be defined from Eq. (2.2) as:

$$P_\theta(t) = ln\left(\frac{I_0}{I}\right) = \int_{path}\mu(x,y)ds \tag{2.3}$$

Besides, using a delta function, Eq. (2.3) can be expressed as Eq. (2.4). This is known as the Radon transform of the function μ(x,y) (KAK and SLANEY, 2001).

$$P_\theta(t) = \int_{-\infty}^{+\infty}\int_{-\infty}^{+\infty}\mu(x,y)\delta(x.cos\theta + y.sin\theta - t)dx\,dy \tag{2.4}$$

This recording procedure is illustrated for one orientation in Figure 2.8, in which the scanning direction is given by t = x.cos(θ) + y.sin(θ) and it is perpendicular to the beam direction s.

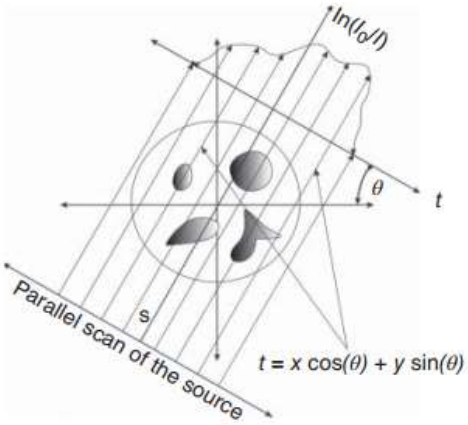

Figure 2.8. Tomographic measurement for a given orientation of the object with respect to the 2D detector system, and the respective projection recorded. Source: TREIMER, 2017.

2.4.2 Reconstruction

The theory of image reconstruction is based on the work of Radon (1917). The set of measurements for a single slice is called the sinogram $P_\theta(t)$. The reconstruction, i.e., the obtainment of a 2D slice image from the projections, can be achieved as the sinogram and the slice are linked by the *Fourier slice theorem* (BECKMANN, 2008). A one-dimensional Fourier transformation of the sinogram, at a given angle, represents a single line in the two-dimensional Fourier transform (FT) of the slice, as shown in Figure 2.9 (BECKMANN, 2008). In other words, it states that given the projection data, it is possible then to estimate the object by simply performing a two-dimensional Fourier transformation (KAK and SLANEY, 2001).

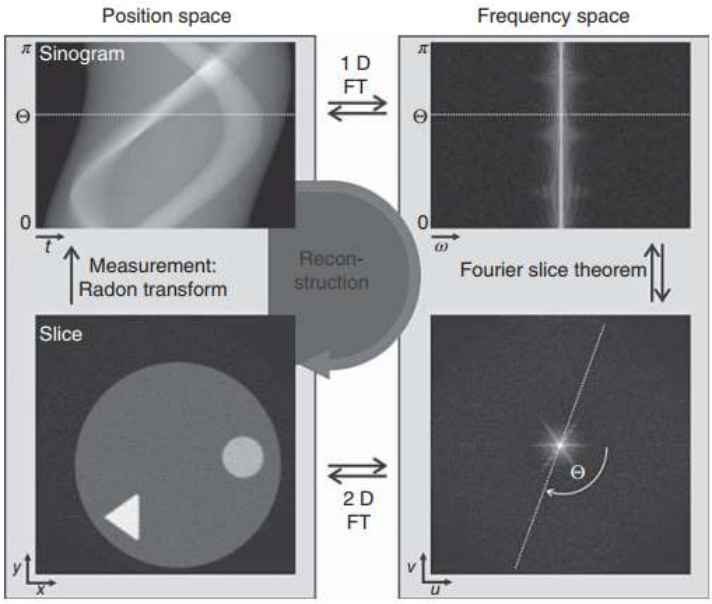

Figure 2.9. Scheme of the reconstruction process for parallel-beam tomography. Source: BECKMANN, 2008.

The more efficient way to implement image reconstruction is the so-called filtered backprojection (FBP), which is explained as it follows (TREIMER, 2017).

The algorithm divides into two parts: the filtering part and the backprojection part. In the former, a simple weighting in the frequency domain is used to estimate a slice of the object's FT (KAK and SLANEY, 2001). It can be done by taking the value of the FT of the projection, $S_\theta(w)$, and multiplying it by the width of the slice at that frequency – if there are M projections over a 180º scan, then at a given frequency w, each slice has a width of $(2\pi|w|)/M$. The factor $|w|$ derives from a change of variable from rectangular to polar coordinates required for the inverse FT (KAK and SLANEY, 2001). The backprojection part is performed by adding together the two-dimensional inverse FT of each weighted projection (KAK and SLANEY, 2001). The main advantages of this approach are: (i) reconstruction process can begin as soon as the first projection is recorded, which can speed up the procedure and reduce the amount of stored data, and, (ii) interpolation needed is often more accurate if performed in the space domain (backprojection part) (KAK and SLANEY, 2001).

A mathematical approach to the filtered backprojection is given in the following (KAK and SLANEY, 2001).

The function μ(x,y) can be expressed as the Fourier representation as:

$$\mu(x,y) = \int_{-\infty}^{+\infty}\int_{-\infty}^{+\infty} M(u,v)e^{2\pi.i.(ux+y\ )}\,dxdy \tag{2.5}$$

As the samples revolve from 0º to 180º, it suggests the use of polar coordinate system rather than the rectangular one. Hence:

$$\mu(x,y) = \int_{0}^{2\pi}\int_{-\infty}^{+\infty} M(w,\theta)e^{+2\pi.i.w.(x.\cos(\theta)+y.\sin(\theta)}w.\,dw.\,d\theta \tag{2.6}$$

Setting t = x.cos(θ) + y.sin(θ) and with the slice theorem, it can be rewritten as:

$$\mu(x,y) = \int_{0}^{\pi}\left[\int_{-\infty}^{+\infty} S_\theta(w)e^{+2\pi.i.w.t}|w|.\,dw.\right]d\theta \tag{2.7}$$

The integral in Equation (2.7) can be written as

$$\mu(x,y) = \int_{0}^{\pi} Q_\theta(x.cos\theta + y.sin\theta)d\theta \tag{2.8}$$

where

$$Q_\theta = \int_{-\infty}^{+\infty} S_\theta(w)e^{+2\pi.i.w.t}|w| \tag{2.9}$$

which represents the filtering operation.

The number of projections that leads to optimum results is given by *Shannon theorem*. It states that a consistent result is achieved if the image is sampled with a frequency that is twice higher than the highest frequency in the Fourier transformed image (TREIMER, 2017). Numerically, considering a parallel source:

$$M \geq \frac{\pi}{2}.N \tag{2.10}$$

where *N* is the number of steps from 0º to 180º for one projection, and *M* the number of projections taken. *M* must equal or be greater than (π/2) multiplied by *N* to achieve a good quality of the reconstruction.

2.4.3 Cone-beam X-ray microtomography setup

For conventional X-ray production, an electron beam is accelerated by a large potential difference against a target and produces radiation (KASTNER et al, 2010). Currently, improvements in lab-based microtomography have permitted to reach sub-micrometer spatial resolution within practicable scanning times. However, in comparison to more sophisticated sources such as synchrotron light, characteristics like the polychromatic nature of the source, limited photon flux and cone beam shape limit the quality of data achievable (LINSMEIER, 2013; RAMOS et al, 2019).

A typical configuration of lab-based X-ray tomography is represented in Figure 2.10. The setup consists of four main parts, highlighted on the figure: (1) microfocus X-ray source, (2) rotation stage, (3) flat-panel 2D detector (usually made of Si), and (4) a computer processing system. Modern systems have been substituting flat-panel detectors for CCD cameras, leading to images with enhanced resolution.

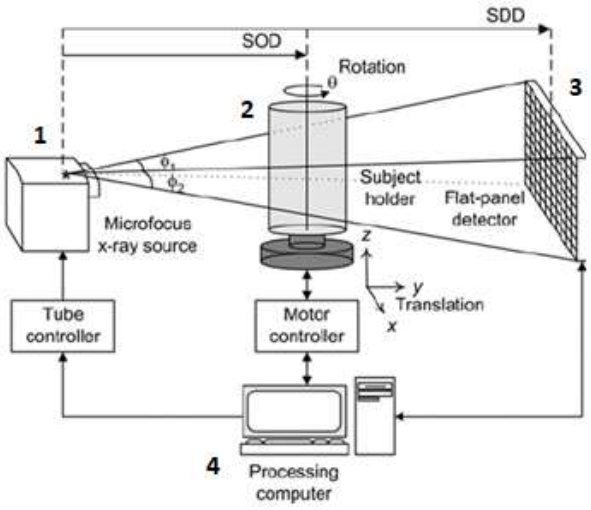

Figure 2.10. Schematic representation of the lab-based X-ray tomography layout. Source: Adapted from LEE et al, 2003.

2.4.4 Interaction of X-rays with matter

X-rays lose their intensity when they pass through an object and interact with the electronic structure of the atoms, due to Compton scattering and photoelectric absorption mechanisms (LAMARSH et al, 2001). This is illustrated in Figure 2.11. Compton scattering corresponds to an inelastic scattering - there is a reduction in photon energy due to loss of kinetic energy. Furthermore, Rayleigh scattering may occur. However, it is predominantly an elastic process; the photon energy is conserved and, hence, it does not contribute significantly to X-ray attenuation (there is only momentum transfer) (SEIBERT AND BOONE, 2005). In photoelectric absorption, the transfer of energy from the radiation to an electron takes place. This process results in the ejection of an inner electron from its shell, with energy corresponding to the difference between photon energy and electron shell binding energy. Also, when an outer atom occupies the vacancy left by the ejected electron, occurs emission of X-ray characteristic of the atom (SEIBERT AND BOONE, 2005).

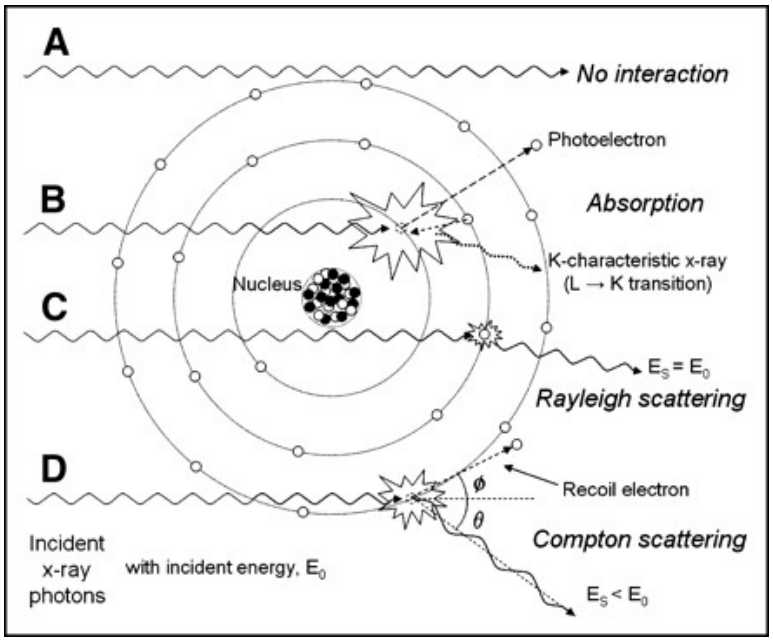

Figure 2.11. Interaction of X-ray with a single atom, showing (A) no interaction, (B) absorption, (C) Rayleigh scattering, and (D) Compton scattering. Source: SEIBERT AND BOONE, 2005.

The change in beam intensity can be quantified by Lambert's law (Eq. 2.2). Considering a monochromatic X-ray beam, the Eq. (2.2) can be rewritten as:

$$I = I_0 \cdot e^{-\mu x} \tag{2.11}$$

where I is the transmitted beam intensity, I_0 is the incident beam intensity, μ is the linear attenuation coefficient of the object (length^{-1}), and x is the length crossed by the X-ray through the sample (BECKMANN, 2008). Many of the objects investigated in materials science do not present a uniform composition though. Hence, Eq. (2.12) should be used instead (HSIEH, 2009). This case is better illustrated in Figure 2.12.

$$I = I_0 \cdot e^{-(\mu_1+\mu_2+\cdots+\mu_N)x} \tag{2.12}$$

The linear attenuation coefficient, except close to absorption edges, can be estimated in terms of atomic number Z, photon energy E, and mass density of the material ρ (BECKMANN, 2008). The relationship shown in Eq. (2.13) derives from cross-section data of atoms, which represents the probability of a given atom of interacting with X-ray radiation (KAK and SLANEY, 2001).

$$\mu \, \alpha \, \frac{Z^4}{E^3} \, \rho \tag{2.13}$$

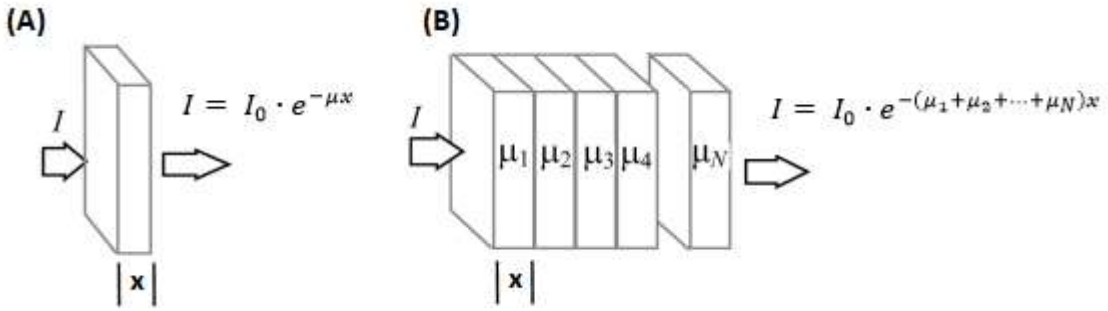

Figure 2.12. Material attenuation for monochromatic beam considering a (A) uniform and (B) non-uniform sample. Source: HSIEH, 2009.

From the database created by Berger et al (2010), the attenuation coefficients with respect to the atomic number for a photon energy of 100keV were plotted in Figure 2.13 to illustrate the power law dependency of attenuation coefficient and density of the material. The higher the atomic number, the higher the attenuation.

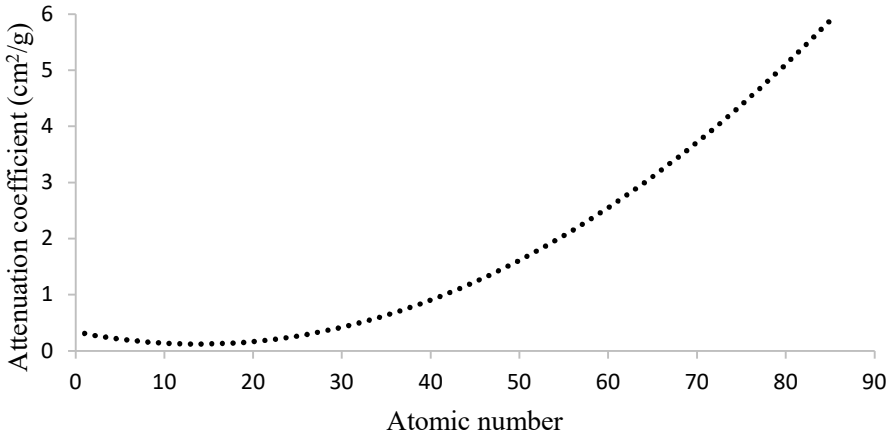

Figure 2.13. Attenuation coefficient with respect to atomic number. Source: Plotted using database from BERGER et al, 2010.

Therefore, the image contrast obtained by X-rays reveals fluctuations in material density and atomic number (STROBL et al, 2009). The output, after reconstruction, is a series of images where each pixel expresses gray-values from 0 to 255 (for 8-bit images), and pixels with a particular gray-value correspond to the same material. In practical terms, 0 corresponds to the absence of attenuation (pores, for example) and 255 the phase that has attenuated the most (lighter shades). For example, Figure 2.14 brings images of a sandstone rock obtained by μCT exhibiting variations in gray scale.

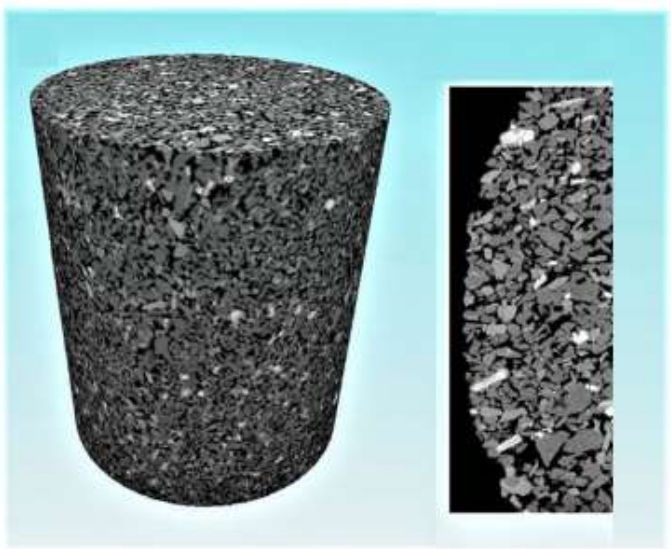

Figure 2.14. 3D image and a slice of a sandstone rock obtained using X-ray microtomography. Source: Adapted from OLIVEIRA et al, 2019.

2.5 Image processing

Image processing is a routine required before tomographic data can be analyzed, qualitatively and quantitatively. The analyzes are usually not straightforward, demanding some meticulous work. The steps usually include artifacts removal, the implementation of filters in order to enhance image quality, and image segmentation (ANDREW, 2014; WANG, 2016). Common artifacts, how to reduce them, and image segmentation are discussed so.

2.5.1 Image artifacts

Image artifacts can be defined as discrepancies between the reconstructed values in an image and the real attenuation coefficients of the material, resulting in non-ideal images that compromises an efficient evaluation of the investigated object (HSIEH, 2009). They can be caused, for example, by the nature of the beam (e.g. cone-beam shape and polychromaticity), characteristics of the material or by measurement errors (HSIEH, 2009).

2.5.1.1 Noise

Normally not recognized as an artifact, noise occurs mainly due to limited intensity of the beam or due to an unfavorable conversion rate of the attenuated beam to visible light (HAIBEL, 2008; DAVIS AND ELLIOT, 2013). Usually, noise is easily identified, and affects the quality of the image, making it harder to distinguish small features (DAVIS AND ELLIOT, 2013). Noise is dependent on resolution and it is not constant throughout the image (DAVIS AND ELLIOT, 2013). The evaluation of noise can be assessed by means of signal-to-noise ratio (SNR), comparing the level of ideal signal (attenuated beam) to the level of background noise; the higher the rate, the less noise is present (pixels deviating from normal) (KASTNER et al, 2010). The use of filters in the reconstruction process can reduce the effect of noise and preserve image details (HAIBEL, 2008). The most used filter is the non-local means filter (NLM), which is a linear denoising filter where the grey-scale of a certain voxel is replaced by the average of the grey-scales of voxels in the vicinity, resulting in an improvement of signal-to-ratio noise (ANDREW, 2014). Figure 2.15 shows the effect of the NLM filter applied to a sandstone rock scanned by synchrotron X-ray tomography.

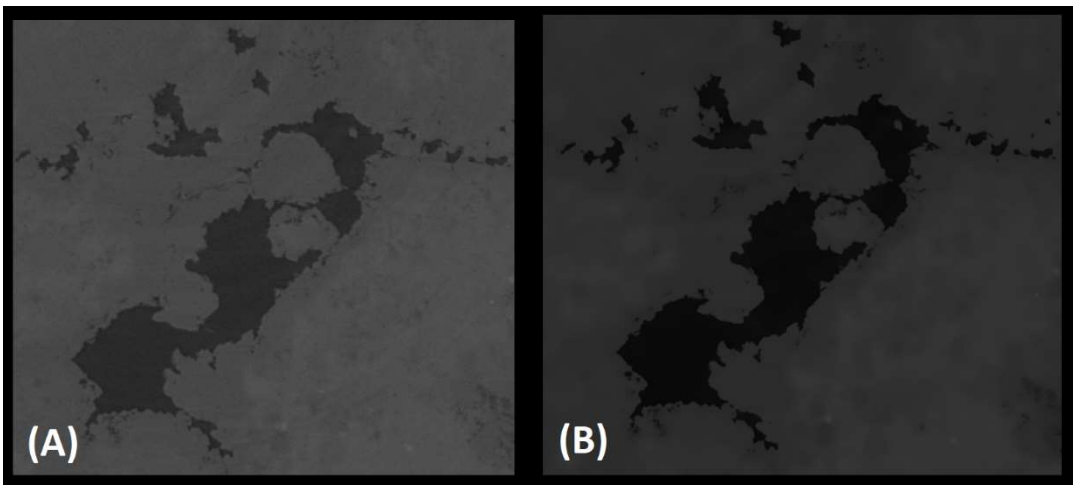

Figure 2.15. Tomographic slice of sandstone sample (A) before and (B) after the application of the non-local means filter. Source: Personal collection.

2.5.1.2 Ring artifacts

One of the most common artifacts is the so-called ring artifact, shown in Figure 2.16-A for a tomographic slice of a superconductor strand of Nb_3Sn and copper (HAIBEL, 2008). They are concentric rings in the images around the center of rotation of the tomographic stage, caused by impurities on the scintillator or by faults on the detectors, for example (HAIBEL, 2008). During measurement, characteristics of all detector elements can be averaged by moving the sample in defined directions, which may reduce ring artifacts. A second way to reduce is the usage of reconstruction filters or post-processing filters, however, ring artifacts are not removed completely, as can be noticed in figure 2.16-B (HAIBEL, 2008).

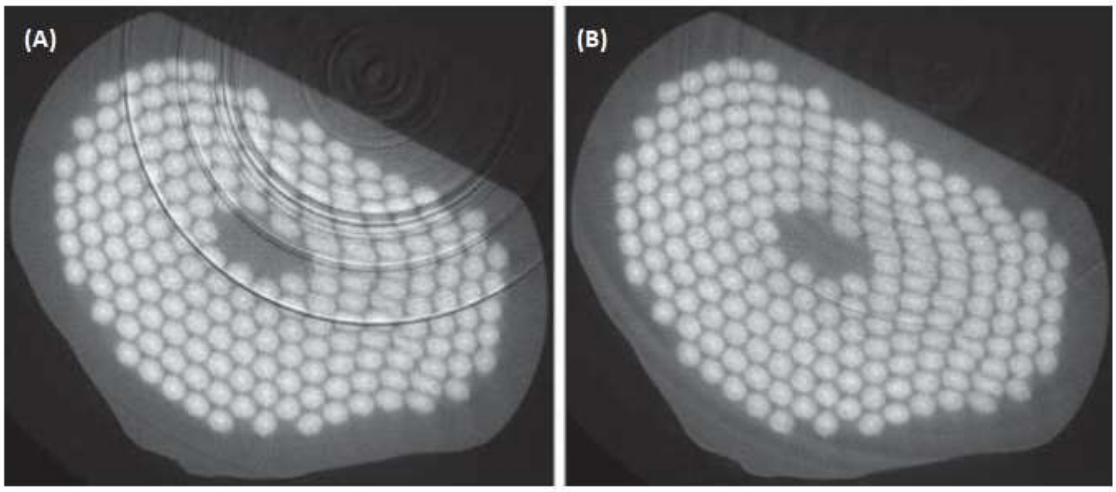

Figure 2.16. Example of ring artifacts for a superconductor material (A) pre and (B) post processing. Source: HAIBEL, 2008.

2.5.1.3 Beam hardening

Beam hardening is only existent in cone-beam X-ray data, as it is caused by the polychromatic nature of the beam (DAVIS AND ELLIOT, 2013). When the beam passes through the object, occurs differential absorption of different X-ray frequencies; low energy X-ray photons are attenuated more easily in comparison with higher energy photons (DAVIS AND ELLIOT, 2013; ANDREW, 2014). This artifact can result in streaks between the highly attenuating phases, as occurred in a sandstone sample in Figure 2.17-A, where Figure 2.17-B corresponds to the same slice, but for synchrotron X-ray tomography (i.e. monochromatic beam). There are algorithms capable of dealing with beam hardening correction, however, it depends on the amount of beam hardening and usually fails for very heterogeneous materials such as rocks (KETCHAM AND HANNA, 2014).

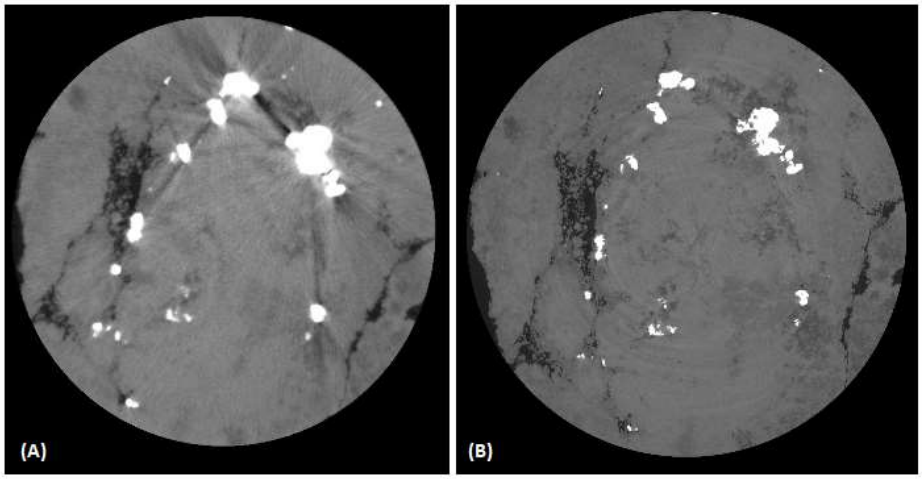

Figure 2.17. Beam hardening registered for a polychromatic X-ray tomography in a rock sample (A). The artifact does not happen for monochromatic beam (B). Source: Personal collection

2.5.1.4 Motion artifacts and centering errors

Motion artifacts occur usually due to movement of the specimen, or components of the setup (e.g. source or detector), during the measurement, or, yet, due to imprecise movement of the step motors (HAIBEL, 2008; DAVIS AND ELLIOT, 2013). Sample movement cannot be totally corrected by algorithms; however, a translational displacement of the sinogram lines towards the optimal sinus curve can fully correct the inexact movement of the step motors (HAIBEL, 2008). This is shown in Figure 2.18, which brings a cross section of a superconductor wire before and after the sinogram correction, resulting in a sharper image.

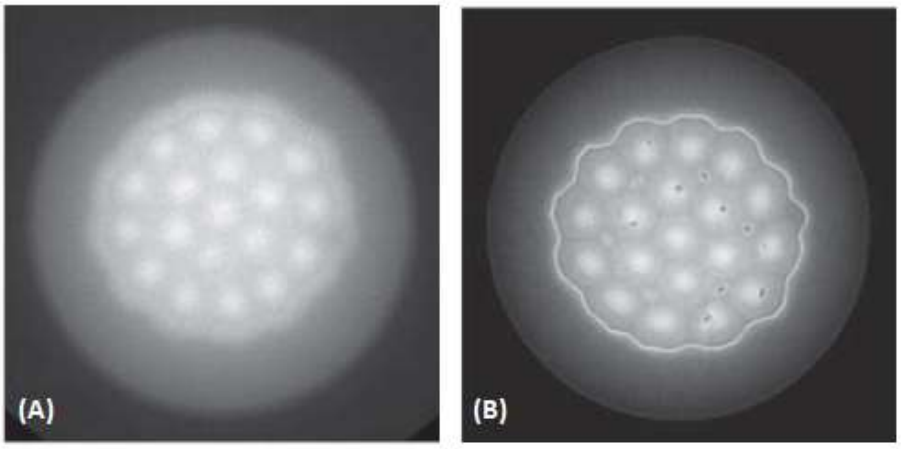

Figure 2.18. Cross section of a superconductor wire (A) before and (B) after sinogram correction. Source: Adapted from HAIBEL, 2008.

Centering error of rotation axis is caused by a deviation of the rotation axis during the progress of the scan and can be corrected by simply adjusting the parameter of the wrong rotation axis during reconstruction (HAIBEL, 2008). Figure 2.19 brings the example of the same superconductor wire mentioned previously, before and after correction.

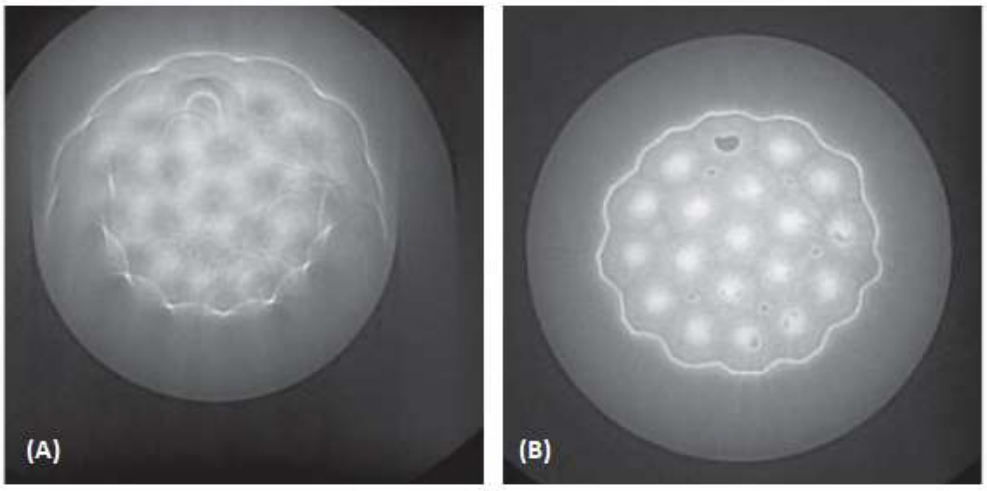

Figure 2.19. Cross section of a superconductor wire (A) before and (B) after rotation axis correction. Source: Adapted from HAIBEL, 2008.

2.5.2 Image segmentation

Image segmentation is the process where the different phases present in the images are distinguished, based on their gray-scale (ANDREW, 2014). It is an important step as it affects the subsequent analyses, such as phase quantification or porosity calculation (ANDREW, 2014).

The simplest and most used method is the global segmentation, where any grey-level below some defined threshold is associated to one phase and any grey-level above this value to another (ANDREW, 2014). The threshold values can be established with assistance of a histogram, as exemplified in Figure 2.20 for a tomographic slice of a carbonate sample obtained by synchrotron X-ray. From Figure 2.20-A, which brings a histogram of 2.20-B, it was possible to distinguish two main regions of grey-values: from 0 to 74 and from 75 to 255, corresponding, respectively, to pores and mineral matrix. Figure 2.20-C brings the mineral phase segmented.

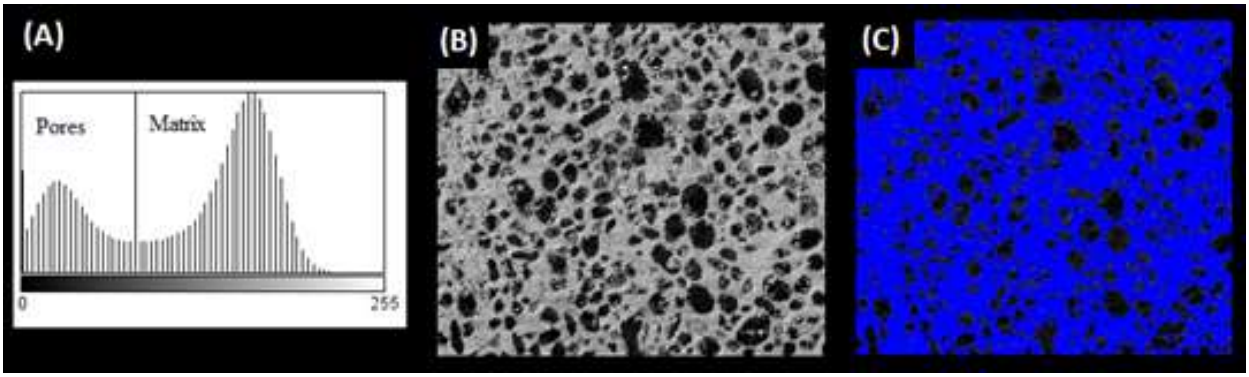

Figure 2.20. Segmentation process applied in a carbonate rock sample. (A) shows the histogram obtained from (B), and (C) shows the mineral phase segmented. Source: Adapted from RAMOS et al, 2019.

There are different software solutions available to perform these steps of image processing, such as the freeware ImageJ, used in this work.

2.6 Conventional mineral characterization techniques

2.6.1 TESCAN Integrated Mineral Analyzer

Although more traditional characterization techniques such as X-ray diffraction (XRD), optical microscopy and energy-dispersive X-ray spectroscopy (EDS) continue playing an important key in mineralogy, the last decades have experienced a widespread use of SEM-based automated systems for morphological and compositional ore quantification (PÉREZ-BARNUEVO et al, 2013).

One of the technologies available is the TESCAN Integrated Mineral Analyzer (TIMA). The system has been specially designed for use in mineral processing industry to determine mineral liberation from samples of feeds, concentrates, and tailings. Through the years, it has also been employed in geological and petrological researches, to visualize and quantify properties such as alteration, contact zones, fractures, re-crystallization, and inclusions mapping (HRSTKA et al, 2018).

The hardware consists of an integrated scanning electron microscope (SEM) equipped with a field emission gun (FEG) coupled to two energy-dispersive X-ray silicon drift detectors. Latest versions may include up to four detectors. While the detectors

record the characteristic X-ray spectra of the elements analyzed, the SEM simultaneously acquires backscattered electron images (HRSTKA et al, 2018; SAMPAIO N. et al, 2018).

This simultaneous acquisition requires considerably high signals digitalization speed. Hence, a high degree of integration between hardware and software is crucial. Additionally, the high integration allows to collect detailed data that were not possible to record by classical EDS phase mapping software solutions and human-interactive operation (HRSTKA et al, 2018).

Sample preparation is time-consuming, requiring particles to be mounted in acrylic or epoxy resin, carefully polished, and with a thin and uniform carbon coating (NEUMANN et al, 2010).

The operation principle of the system relies on the fact that when an electron beam interacts with a sample, a large number of externally signals are observed. Here, two signals are of major relevance: backscattered electrons (BSE) and X-ray emission.

BSE are those electrons from the incident beam that suffers a series of elastic scattering events and are reflected out of the specimen surface without much loss of energy. Backscattered imaging is often used to characterize mineral ores, as there is a strong dependence of the backscattered coefficient (η) (the number of backscattered electrons emitted from a specimen) on mean atomic number. The higher the atomic number, the whiter the pixel will appear on the image, which allows to produce images exhibiting atomic number contrast (NAPCHAN, 2001).

The emitted X-ray is the result of an electron returning to an inner and lower energy level after being excited and moved to a higher energy level. When it returns, the energy it had previously gained by the excitation is emitted as a photon, which carries a wavelength that is characteristic of the element. This can be used to identify the element, since each one has a characteristic emission spectrum (NEUMANN et al, 2010).

All the processing and integration of SEM and EDS information are performed already during data collection, saving time and providing results by the time the measurements are finished. Table 2.5 brings a summary of the main reports available.

Table 2.5. Main reports available on TIMA. Source: Adapted from SAMPAIO N. et al, 2018.

Mineral mass	Mineral locking
Element mass	Grade recovery curve
Elements maps	Grain size
Mineral associations	Particle size
Mineral liberation	Particle density
Specific surface area	Particle viewer

2.6.2 Elemental and mineralogical analysis

The identification of the minerals that compose a sample is usually performed using X-ray diffraction (XRD). The technique is based on the diffraction of a characteristic X-rays, commonly produced by copper or cobalt filaments, through the crystalline structure of the minerals.

As the X-rays travel through the sample, which is a powder sample, they may satisfy the diffraction condition stated by Bragg's law (Eq. 2.14), where d is the interplanar distance (nm), θ is the scattering angle (º), n is a positive integer (diffraction order), and λ is the wavelength of the incident X-ray beam (PORPHIRIO et al, 2010).

$$2d\ sin\theta = n\lambda \tag{2.14}$$

When Bragg's law is satisfied, constructive interference occurs and a peak in intensity occurs. These peaks are displayed in a diffraction pattern, which is individual of each mineral, allowing mineral identification. The identification can be done manually or by means of dedicated programs.

X-ray diffractometers consist of three basic components: An X-ray tube that produces X-ray by heating a filament to accelerate electrons against a target; a sample holder that rotates, and an X-ray detector (PORPHIRIO et al, 2010).

Elemental characterization may serve as supplementary information to support mineral identification. One of the most used technique is X-ray fluorescence (XRF). The principle of the method is the emission of characteristic X-rays from a material that has

been excited, as outlined in the past topic (2.5.1). However, here the sample is excited by high-energy X-rays (not electrons).

Qualitative analyzes are generally straightforward and reliable, due to elemental spectrum simplicity. The technique also offers semi-quantitative approaches by comparing peak heights with standard spectra (PORPHIRIO et al, 2010).

The Fourier-Transform Infrared Spectroscopy (FTIR) is another technique of vast application in mineral characterization, especially for better identification of minerals owing low crystallinity, with high content of substitution in the crystal structures, or amorphous materials (PORPHIRIO et al, 2010). Sample preparation is usually made by mixing the powder sample with potassium bromide (KBr) to form pellets. Minerals can absorb infrared radiation that resonates with their internal structure at specific wavelengths and produces different forms of atoms vibration. As each molecular bond carries its specific vibration pattern, this provides a signature for different minerals (GRIFFITHS and HASETH, 2007).

2.6.3 Surface exposure

Surface exposure is another attribute of interest to the process engineer, especially to predict flotation efficiency and leaching performance. It is commonly quantified using SEM-EDS-based analysis of polished sections (REYES et al, 2017).

Surface area, as well as porosity, can also be determined by the application of the Brunauer, Emmett and Teller (BET) and Barrett-Joyner-Halenda (BJH) models to N_2 adsorption/desorption isotherms (ROUQUEROL et al, 2013. A detailed explanation on these models are outside the scope of this thesis.

REFERENCES

ABAL - Brazilian Aluminum Association. Bauxite in Brazil - Responsible Mining and Competitiveness, 2018.

ALMEIDA, V.O., SCHNEIDER, I.A.H. Production of a ferric chloride coagulant by leaching an iron ore tailing. **Minerals Engineering** 156, 106511, 2020.

ANDREW M. **Reservoir-Condition Pore-Scale Imaging of Multiphase Flow.** Department of Earth Science and Engineering, Royal School of Mines, Imperial College London. PhD Thesis, 2014.

ARAUJO, A.C. et al. Flotação de Minérios de Ferro. In: Chaves, A. P. **Teoria e Prática do Tratamento de Minérios: A Flotação no Brasil**. Vol 4. Oficina de Textos, São Paulo, 2013. Portuguese.

ASGHAR Z, REQUENA G. Multiscale tomographic analysis of heterogeneous cast Al-Si-X alloys. **J. of Microscopy**. 259, 1-9, 2015.

BARUCHEL, J. et al, editors. **X-ray Tomography in Material Science.** 1st ed. Hermes Science Publications, Paris, 2000.

BECKMANN, F. **Neutron and Synchrotron-Radiation-Based Imaging for Applications in Materials Science – From Macro- to Nanotomography**: Wiley-Vch Verlag GmbH & Co. KGaA, 2008.

BERGER, M.J. et al. **XCOM: Photon Cross Sections Database**. NIST Standard Reference Database 8 (XGAM), 2010.

BOBICKI, E. R. et al. Microwave treatment of ultramafic nickel ores: Heating behavior, mineralogy, and comminution effects. **Minerals** 8, 1–19, 2018.

CHAVES, A.P. **Teoria e Prática do Tratamento de Minérios: Separação Densitária**. Vol 6. Oficina de Textos, São Paulo, 2013. Portuguese.

COSTA, M.L. **Alumínio e bauxita no Brasil – Recursos minerais no Brasil: problemas e desafios.** Academia Brasileira de Ciências. Rio de Janeiro, 2016. Portuguese.

DAVIS, G. R., ELLIOT, J. C. Artefacts in X-ray microtomography of materials. **J. of Materials Science and Technology** 22, 2013.

EVANS, C.L., NAPIER-MUNN, T.J. Estimating error in measurements of mineral grain size distribution. **Minerals Engineering** 52, 198-203, 2013.

EVANS, C.L. et al. Quantifying mineral grain size distributions for process modelling using X-ray micro-tomography. **Minerals Engineering** 82, 78–83, 2015.

FANDRICH, R.G. et al. Two stereological correction methods: allocation method and kernel transformation method. **Minerals Engineering** 8, 707-715, 1998.

FURAT, O. et al. Description of Ore Particles from X-Ray Microtomography (XMT) Images, Supported by Scanning Electron Microscope (SEM)-Based Image Analysis. **Microsc Microanal.**, 2018.

GAUDIN, A.M. **Principles of Mineral Dressing**. McGraw-Hill Inc. London, UK, 1939.

GAY, S.L. Liberation modelling using particle sections. PhD thesis. The University of Queensland, 1994.

GAY, S.L., MORRISON, R.D. Using Two Dimensional Sectional Distributions to Infer Three-Dimensional Volumetric Distributions – Validation using Tomography. **Part. Part. Syst. Charact.** 23, 246–253, 2006.

GHOLAMI, H. et al. The effect of microwave's location in a comminution circuit on improving grindability of a porphyry copper deposit. **Energy Sources A**, 2020.

GRIFFITHS, P.R., HASETH, J.A. **Fourier transform infrared spectrometry.** 2ed, John Wiley & Sons, 2007.

GUIMARÃES, C., DURÃO, F. 2D simulation model of mineral particles yielded by discriminatory size reduction. **Minerals Engineering** 16, 1339-1348, 2003.

GUIMARÃES, C., DURÃO, F. Application of a cellular automata-based simulation model of size reduction in mineral processing. **Minerals Engineering** 20, 541-551, 2007.

HABASHI, F. **A Texbook of Hydrometallurgy**. Métallurgie Extractive Québec, Enr. 800, Quebec, Canada, 1993.

HAIBEL, A. μ-Tomography of Engineering Materials. In: Reimers W et al. **Neutrons and synchrotron radiation in engineering materials science**. Weinheim: Wiley-Vch Verlag GmbH & Co. KGaA, 2008.

HIND, A.R. et al. The surface chemistry of Bayer process solids: a review. **Colloids and Surface A** 146, 359-374, 1999.

HRSTKA, T. et al. Automated mineralogy and petrology – applications of TESCAN Integrated Mineral Analyzer (TIMA). **Journal of Geosciences** 63, 47–63, 2018.

HSIEH J. **Computed Tomography: Principles, Design, Artifacts, and Recent Advances**. 2ed, 2009.

JESUS, C.A.G., JOAQUIM, L.G. Ferro. **Brazilian Mineral Summary**. 2018. Portuguese.

KAK A C, SLANEY M. **Principles of Computerized Tomographic Imaging**, Society of Industrial and Applied Mathematics, 2001.

KASTNER J, HARRER B, REQUENA G, BRUNKE O. A comparative study of high-resolution cone beam X-ray tomography and synchrotron tomography applied to Fe- and Al-alloys. **NDT&E International** 43, 599-605, 2010.

KETCHAM R, HANNA R. Beam hardening correction for X-ray computed tomography of heterogeneous natural materials. **Computers and Geoscience** 67, 49-61, 2014.

KLEIN, C., HURLBUT, C. S. **Manual of Mineralogy**. 20 ed. John Wiley and Sons Inc., p.531-583, 1985.

KING, R.P., SCHNEIDER, C.L. Stereological correction of linear grade distributions for mineral liberation. **Powder Technology** 98, 21-37, 1998.

LAMARSH et al. **Introduction to Nuclear Engineering**. 3ed. Prentice Hall, 2001.

LANDIS E N, KEANE D T. X-ray microtomography. **Materials Characterization** 61, 1305-1316, 2010.

LEE, Sang Chul et al. A Flat-Panel Detector Based Micro-CT System: Performance Evaluation for Small-Animal Imaging. **Physics in Medicine and Biology**, v. 48, n. 24, p. 4173–4185, 2003.

LEE, Se-Hee et al. Synchrotron X-ray nanotomography and three-dimensional nanoscale imaging analysis of pore structure-function in nanoporous polymeric membranes. **Journal of Membrane Science** 535, 28-34, 2017.

LEIGH, G.M., LYMAN, G.J., GOTTLIEB, P. Stereological estimates of liberation from mineral section measurements: a rederivation of Barbery's formulae with extensions, **Powder Technology** 87, 141–152, 1996.

LEISSNER, T. et al. Evaluation of mineral processing by assessment of liberation and upgrading. **Minerals Engineering** 53, 171–173, 2013.

LIN, C.L., MILLER, J.D. Cone beam X-ray microtomography for three-dimensional liberation analysis in the 21st century. **Int. J. of Mineral Processing** 47, 61-73, 1996.

LIN, C.L., MILLER, J.D. 3D characterization and analysis of particle shape using X-ray microtomography (XMT). **Powder Technology** 154, 61-69, 2005.

LIN, C.L., MILLER, J.D. Cone beam X-ray microtomography-a new facility for three-dimensional analysis of multiphase materials. Mining, Metallurgy and Exploration 19, 65-71, 2002.

LINSMEIER C et al. Advanced materials characterization and modeling using synchrotron, neutron, TEM, and novel micro-mechanical techniques — A European effort to accelerate fusion materials development. **Journal of Nucleus Materials** 442, S834-S845, 2013.

LOTTER, N.O., EVANS, C.L., ENGSTROM, K. Sampling – a key tool in modern process mineralogy. **Minerals Engineering** 116, 196-202, 2018.

MAGALHÃES, L.F. et al. Iron ore tailings as a supplementary cementitious material in the production of pigmented cements. **Journal of Cleaner Production** 274, 2020.

MARIANO, R.A., EVANS, C.L. Error analysis in ore particle composition distribution measurements. **Minerals Engineering** 82, 36-44, 2015.

MILLER, J.D.; LIN, C.L. Treatment of polished section data for detailed liberation analysis. **Int. Journal of Mineral Processing** 22, 41-58, 1988.

MILLER, J.D. et al. Liberation-limited grade/recovery curves from X-ray micro CT analysis of feed material for the evaluation of separation efficiency**. Int. J. of Mineral Processing** 93, 48-53, 2009.

MILLER, J.D., LIN, C.L. X-ray tomography for mineral processing technology – 3D particle characterization from mine to mill. **Minerals & Metallurgical Processing** 35, 1-12, 2018.

MOMOSE A. Recent Advances in X-Ray Phase Imaging. **Japanese Journal of Applied Physics**, Part 1: Regular Papers and Short Notes and Review Papers, 2005.

NAPCHAN, E. Backscattered Electrons in the SEM. **Microscopy and Analysis**, 9-11, 2001.

NEUMANN, R. et al. Caracterização Mineralógica de Minérios – Parte II. In: Luz, A.B. et al. **Tratamento de Minérios.** 5ed. CETEM. Rio de Janeiro, 2010. Portuguese.

NOVO, B. L. et al. Caracterização e beneficiamento de bauxita: estudo do caso da bauxita nodular do nordeste do Pará. XXVI ENTMME, Poços de Caldas, 2015. Portuguese.

OLIVEIRA, G.J.R. et al. Probing the 3D molecular and mineralogical heterogeneity in oil reservoir rocks at the pore scale. **Scientific Reports** 9, 1-10, 2019.

PÉREZ-BARNUEVO, L. et al. Automated characterisation of intergrowth textures in mineral particles. A case study. **Minerals Engineering** 52, 136-142, 2013.

PORPHIRIO, N. H. et al. Caracterização Mineralógica de Minérios – Parte I. In: Luz, A.B. et al. **Tratamento de Minérios.** 5ed. CETEM. Rio de Janeiro, 2010. Portuguese.

RAMOS, G.J. et al. Evaluation of the conventional and synchrotron X-ray tomography applied to heterogeneous oil reservoir rocks. **Brazilian Journal of Radiation Sciences** 7, 1-15, 2019

REYES, F. et al. Calibrated X-ray micro-tomography for mineral ore quantification. **Minerals Engineering** 110, 122–130, 2017.

REYES, F. et al. Quantifying mineral liberation by particle grade and surface exposure using X-ray microCT. **Minerals Engineering** 125, 75–82, 2018.

ROUQUEROL, J. et al. **Adsorption by Powders and Porous Solids: Principles, Methodology and Applications.** Elsevier Science, 2013.

SAMPAIO, J. A. et al. Bauxita. In: **Rochas e Minerais Industriais,** 2ed. CETEM. 977p., 2008. Portuguese.

SAMPAIO, N. P. et al. The formation of Brazilian minerals database for integrated SEM-EDS system applied to the gold ore characterization. **Holos** 3, 2-22, 2018.

SEIBERT J A, BOONE J M. X-ray imaging physics for nuclear medicine technologists. Part 2: X-ray interactions and image formation. **J Nucl Med Technol** 33, 3-18, 2005.

SHETTIMA, A.U. et al. Evaluation of iron ore tailings as replacement for fine aggregate in concrete. **Construct. Build. Materials** 120, 72-79, 2016.

STARON, P. et al. **Neutrons and Synchrotron Radiation in Engineering Materials Science: From Fundamentals to Applications.** 2ed. Wiley, 2017.

STOCK, S.R. X-ray microtomography of materials. ASM International, 1999.

STROBL M et al. Advances in neutron radiography and tomography. **J. Phys. D: Appl. Phys**. 42, 243001, 2009.

SUN, Y. et al. A new approach for recovering iron from iron ore tailings using suspension magnetization roasting: A pilot-scale study. **Powder Technology** 361, 571-580, 2020.

TREIMER W. Imaging. In: Reimers W et al. **Neutrons and synchrotron radiation in engineering materials science.** Weinheim: Wiley-Vch Verlag GmbH & Co. KGaA, 2017.

UEDA, T. et al. Statistical effect of sampling particle number on mineral liberation assessment. **Minerals Engineering** 98, 204–212, 2016.

UEDA, T., OKI, T., KOYANAKA, S. Stereological correction method based on sectional texture analysis for the liberation distribution of binary particle systems. Advanced **Powder Technology** 28, 1391–1398, 2017.

UEDA, T. et al. Experimental analysis of mineral liberation and stereological bias based on X-ray computed tomography and artificial binary particles. **Advanced Powder Technology** 29, 462–470, 2018.

UEDA, T. Experimental validation of a statistical reliability method for the liberation distribution measurement of ore particles. **Minerals Engineering** 140, 2019.

UNITED STATES GEOLOGICAL SURVEY. Bauxite and Alumina Statistics and Information, 2019a. Available on < https://www.usgs.gov/centers/nmic/>. (Accessed June 16th, 2020).

UNITED STATES GEOLOGICAL SURVEY. Iron Ore Statistics and Information, 2019b. Available on < https://www.usgs.gov/centers/nmic/>. (Accessed August 15th, 2020).

VAN DER WIELEN, K.P., ROLLINSON, G. Texture-based analysis of liberation behaviour using Voronoi tessellations. **Minerals Engineering** 89, 93-107, 2016.

VAN DEURSEN, C. M. Métodos de desaguamento e disposição de rejeito da bauxita: estudo de caso e avaliação econômica. São Paulo: Escola Politécnica da USP, 2016. 127p. (Dissertação, Mestrado em Engenharia Mineral).

WANG, Y. **Image Processing Techniques for Three-dimensional Analysis of Multiphase Multi-size Packed Particle Beds Using X-ray Tomography.** PhD Dissertation. University of Utah, Salt Lake City, UT, USA, 2016.

WANG, Y. et al. Quantitative analysis of exposed grain surface area for multiphase particles using X-ray microtomography. **Powder Technology** 308, 368–377, 2017.

WANG, Y. et al. Stereological correction of perimeter-based estimates of exposed grain surface area. **Minerals Engineering** 126, 64–73, 2018.

WIEGEL, R.L. The rationale behind the development of one model describing the size reduction/liberation of ores. **Advances in Comminution**, 225-242, 2006.

WIEGEL, R.L. The solitary grain liberation model: a description of a mineral liberation model for low-grade ores. **Mining, Metallurgy and Exploration** 28, 159-168, 2011.

WILLS, B.A., FINCH, J.A. **Will's Mineral Processing Technology**. 8ed. Elsevier, Oxford, 2016.

YU, J. et al. An innovative methodology for recycling iron from magnetic preconcentrate of an iron ore tailing. **Physicochem. Probl. Miner. Processing** 54, 668-676, 2018.

ZAMBRANO, M. et al. Pore-scale dual-porosity and dual-permeability modeling in an exposed multi-facies porous carbonate reservoir. **Marine and Petroleum Geology** 128, 105004, 2021.

ZHANG, J., SUBASINGHE, N. Prediction of mineral liberation characteristics of comminuted particles of high-grade ores. **Minerals Engineering** 49, 68-76, 2013.

CHAPTER 3

EVALUATION OF MINERAL LIBERATION OF A BAUXITE ORE BASED ON 3D COMPOSITIONAL AND TEXTURAL CHARACTERISTICS BY X-RAY MICROTOMOGRAPHY

ABSTRACT

Bauxite ore is the primary source of aluminum and its oxides. The depletion of high-grade reserves demands the development of concentration strategies for low-grade high-silica bauxite ores. Mineral liberation plays an important role in mineral concentration, as it determines the maximum possible grade for a given recovery of downstream processes. Commonly, microscope-based automated image analysis systems have been used to obtain data regarding mineral liberation. However, this kind of analysis leads to significant stereological bias due to the intrinsic two-dimensionality characteristic of the technique. Three-dimensional imaging techniques such as X-ray microtomography comes as an alternative method to measure mineral liberation, eliminating the need for stereological corrections. In this work, we explored the potentiality of high-resolution X-ray microtomography to investigate the characteristics of liberation of a complex Brazilian bauxite. Due to differences in linear attenuation coefficient, gibbsite, kaolinite, and hematite could be easily distinguished and quantitative analysis of liberation could be performed. Grade distributions in 2D and 3D were correspondent when all possible cross-sections were considered in 2D. However, 2D surface exposure did not converge accurately to the 3D fashion due to the loss of 3D information. The magnitude of stereological effect revealed that 2D analysis overestimates the degree of grade and surface exposure.

3.1 Introduction

Bauxite ore is the primary source of aluminum and its oxides, finding applications that go from production of metallic aluminum to abrasive materials and refractory products (SAMPAIO et al, 2008; DILLINGER et al, 2020; BARBOSA et al, 2016). The ore is an impure mixture of aluminum oxyhydroxides, where the predominant difference between these specimens is present in their crystalline structures (TABERAUX and PETERESON, 2014). The most significant aluminum-bearing minerals are gibbsite ($Al(OH)_3$), boehmite (γ-AlO(OH)), and diaspore (α-AlO(OH)); and the main impurities are kaolinite ($Al_2Si_2O_5(OH)_4$), goethite (FeO(OH)), rutile (TiO_2), hematite (Fe_2O_3), and quartz (SiO_2) (MELO et al, 2020; RODRIGUES et al, 2016).

The aluminum production is mostly performed by the Bayer process, which transforms aluminum-bearing minerals in alumina (Al_2O_3), followed by the Hall Héroult one, which produces metallic aluminum. The Al/Si ratio that feeds the Bayer process is a key factor in the operational and economic viability of the aluminum industry (AYALA et al, 2019; BABISK et al, 2020; GIBSON et al, 2017). The silica from kaolinite is called reactive silica because it dissolves in the Bayer process causing expensive loss of the caustic soda that is the leaching agent. Therefore, the Bayer process feed must comprise < 5% of reactive silica (GIBSON et al, 2017). High-grade ores like those found in northern Brazil, for instance, are generally processed simply through comminution operations, and wet classification or blending of different ores are employed reduce the kaolinite content (SMITH, 2009; MARINO, 2012). However, the depletion of high-quality bauxite and the need to process high-silica reserves have been demanding the implementation of concentration strategies, such as froth flotation, to increase the Al/Si ratio (LAITINEN et al, 2016; LIU J et al, 2015). This requirement has drawn the attention of many researchers to the necessity of a more comprehensive understanding of the factors that influence the concentration of low-grade high-silica bauxite ores, such as liberation degree between gibbsite and kaolinite (XU et al, 20020; LIU Z et al, 2020; WANG Y et al, 2019).

Particularly, mineral liberation plays an important role in mineral concentration. Its relevance relies in the fact that it determines the maximum possible grade for a given recovery of downstream processes (LEISSNER et al, 2013; REYES et al, 2018).

Commonly, microscope-based automated image analysis systems (SEM-based) that combine scanning electron microscopy (SEM) and energy-dispersive X-ray spectroscopy (EDS) have been used to obtain data regarding mineral liberation (REYES et al, 2017). However, this kind of analysis leads to significant stereological bias due to the intrinsic two-dimensionality characteristic of the technique. The liberation assessment from polished sections normally overestimates the degree of liberation, because mixed particles may appear to be liberated in 2D, whereas truly free particles are always liberated in 2D (REYES et al, 2018; UEDA et al, 2018; WANG et al, 2018)

There have been many attempts to correct this major drawback. Gaudin, in 1939, was the first author to point out the existence of stereological bias of the degree of liberation (GAUDIN, 1939). Following this, the earliest works relied mainly on computer simulation and mathematical modelling (MILLER and LIN, 1988; KING and SCHNEIDER, 1998; LEIGH et al, 1996). However, the models are usually not satisfactory, since they depend on ore texture and each ore carries its own characteristics. Additionally, corrections for more than two phases are fairly unsatisfactory (WANG et al, 2018).

In this context, the usage of non-destructive three-dimensional imaging techniques such as X-ray microtomography (μCT) comes as an alternative method to measure mineral liberation, eliminating the need for stereological corrections. Early limited to coarser fragments due to limitation of spatial resolution, it is now possible to acquire high-resolution tomographic data of packed beds within short scanning times (WANG et al, 2018, WANG et al, 2016; TREIMER, 2017). In tomographic imaging measurement, a sample is located on a rotation stage between the X-ray source and the detector. When X-rays pass through the specimen, the beam will lose intensity due to scattering and absorption processes. As it rotates, the object is irradiated from several orientations and the transmitted beam intensity along a series of linear path recorded. By means of mathematical principles of tomography, a sequence of 2D images are generated and, when they are stacked together, they represent the object three-dimensionally (TREIMER, 2017).

The technique allows fast 3D visualization, with simple or no sample preparation, readily providing volumetric information concerning grains morphology and phase distribution within the particles (EVANS et al, 2015). Nevertheless, one limitation of the method, in comparison to microscope-based automated systems, is the inability to determine the mineralogy of the ore (REYES et al, 2018).

Pioneers in this three-dimensional approach, Lin and Miller have contributed substantially over the last few decades. Their work anticipated the potential of implementation of μCT and followed the development of equipment over time (LIN and MILLER, 1996; 2002; 2005). Recent works include Wang et al. (2018), who investigated perimeter-based liberation of a copper ore and compared to results obtained by a SEM-based system; and Wang et al. (2017), who assessed liberation and exposed grain surface of an auriferous pyrite ore for flotation. Reyes et al. (2018) studied 2D and 3D liberation of a low-grade porphyry copper in terms of grade and surface exposure. In a different work, Reyes et al. (2017) proposed a methodology that combined μCT and SEM images in order to obtain more detailed information on mineral characterization. Ueda et al. (2018) and Ueda (2018) proposed a method for stereological correction based on 2D and 3D attributes of artificial particles and tested the statistical reliability of the approach.

The complex structure of the aluminosilicates makes the stereological bias even more pronounced and it becomes challenging to perform an accurate liberation analysis of bauxite using conventional techniques (XU L et al, 2014; GEN et al, 2012). Our objective is to apply X-ray microtomography (μCT) to determine mineral liberation of a metallurgical bauxite in terms of 3D compositional and textural characteristics. This study will support the development of a concentration strategy to reduce the content of reactive silica improving the hydrometallurgical extraction of aluminum. Therefore, in this work, we anticipate the necessity of applying froth flotation prior to hydrometallurgical treatment and explored the potentiality of high-resolution μCT to understand better the characteristics of liberation of a complex Brazilian bauxite ore, a key factor on flotation performance. From the 3D tomographic data, liberation with regard to volume grade and surface exposure were measured. To assess the magnitude of stereological error, 2D image data were also evaluated to determine grade by area and surface exposure by perimeter. There are a few published works regarding diasporic bauxite processing, especially from China, as summarized by Gibson et al. (2017); however, there is still a

lack of studies covering gibbsitic ores and experimental evidences on bauxite liberation are needed. Furthermore, liberation models for stereological corrections have not found much practical application and there is the need to better understand the potential of 3D experimental data.

3.2 Materials and methods

A representative sample of a metallurgical bauxite from Juruti mine, a reserve located in the North of Brazil, state of Pará, was supplied by the Alcoa company. The sample is a gibbsitic ore exhibiting a complex mineral structure, that has been crushed, ground, and classified. Its granulometry is 90% passing approximately 100μm, determined by wet sieving. The sample was prepared, characterized and submitted to high-resolution microtomography experiments.

3.2.1 Mineralogical and chemical characterization

The semiquantitative chemical analysis of the sample was evaluated by X-ray fluorescence (XRF) in a Panalytical Zetium spectrometer, using a pulverized aliquot. Loss on ignition (LOI) was assessed at 1000ºC for 2h by calculating the weight loss at this condition.

Mineralogical composition was assessed on ground sample by powder X-ray diffraction (XRD), with backload hand mount to minimize preferential orientation, using a D2 Phaser diffractometer (2nd Generation) by Bruker. The equipment is available at the Nanotechnology Laboratory (NanoLab), a facility part of the Department of Metallurgical and Materials Engineering of the Federal University of Ouro Preto. The measurements were performed using an X-ray wavelength of 1.5406Å (Cu K-α), with 2θ varying from 0 to 90º and a step size of 0.018º. The peaks were analyzed and phase identification carried out by means of the software solution *Match!*, based on the Crystallography Open Database (COD). Semiquantitative phase quantification was also determined by *Match!* by running an automatic refinement based on the relative intensity of the peaks (I/I_0). The mineral phases were selected based on the figure-of-merit (i.e. quality of the fitting) as well as on a visual inspection of their agreement with the experimental diffractogram pattern.

The grades of available aluminum and reactive silica were determined by titrimetric and colorimetric analyses according to the ABNT NBR 15944.

3.2.2 High-resolution X-ray microtomography

High-resolution X-ray microtomography was implemented to investigate the spatial distribution of the mineral phases through the particles. The experiments were conducted at NanoLab in a Skyscan 1272 microtomography scanner by Bruker. The equipment operates from 20kV to 100kV and uses a cooled CCD camera of 16Mp as a detector, providing images of enhanced quality in comparison to traditional scanners. The images achieved voxel size of 5.0µm and further details on the experimental conditions are presented in Table 3.1.

Table 3.1. Experimental conditions used in the tomographic experiments.

Table 1: Experimental conditions used in the tomographic experiments.

Instrument	Skyscan 1272 - Bruker
Pixel size (µm)	5.0
Exposure time (s)	2
Number of projections	1600
Energy/Current	70kV/142µA
Source-to-object distance (mm)	46.46
Source-to-detector distance (mm)	272.43
Source spot size (µm)	<5
Detector/Resolution	CCD camera/16Mp
Detector pixel size (µm)	7.4
Filter	0.5mm Aluminum

The particles were dispersed in acrylic resin to form samples of cylindrical shape of about 6mm in diameter and 10mm in height (Figure 3.1). Even though the technique does not require any sample preparation, a well distribution of the particles contributes to make image processing and quantitative analysis easier, as it enables to identify isolated particles straightforwardly.

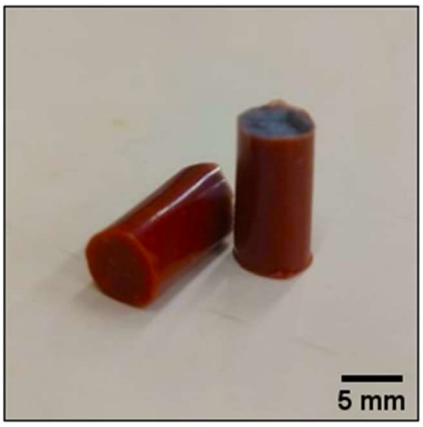

Figure 3.1. Bauxite ore sample. The particles were dispersed in acrylic resin to form samples of cylindrical shape of about 6mm in diameter.

3.2.3 Image processing and liberation assessment

Although the data exhibited high quality, the first step of image processing was to use a non-local means denoising algorithm to smooth the images. By applying a manual intensity threshold, based on the gray level of the tomographic images, mineral phases were segmented. Many cross-sectional images from different parts of the reconstructed volume were carefully analyzed using a threshold tool provided by the freeware ImageJ. Following, each particle was individualized by an object separation algorithm and received a unique label, then quantitative analysis was performed, with CTAn by Bruker. CTAn offers a custom processing function, which permits the user to create analysis routines. The operations selected to run are executed in sequence as defined by the user in a task list, allowing semi-automatic data processing. For volume rendering and 3D visualization, CTVox was used, also developed by Bruker.

Liberation was assessed in terms of compositional and textural characteristics of the fragments, from both 3D and 2D perspectives. Usually, in bauxite pretreatment by flotation, the specimen floated is kaolinite. Hence, the liberation reported in this work is for this aluminosilicate. In order to examine 3D liberation, for each particle, volume grade and proportion of surface exposure of kaolinite in relation to the total surface area of the particle were measured. For the 2D fashion, liberation was defined concerning grade by area and proportion of surface exposure by perimeter exposed. To investigate the extent

of stereological bias, 2D analyses were performed considering (i) all the slices possible per particle or considering (ii) 9, 5, and 2 random slices per particle.

In image analysis, the estimation of volume and area of objects is a simple task and consists in counting the number of voxels or pixels that constitute them, weighted by the volume of an individual voxel or the area of an individual pixel. However, to obtain the exposed surface area of the mineral of interest, firstly, one needs to identify the voxels of this particular mineral that are in the vicinity of the background (and not of other mineral phases). This can be achieved by calculating a distance map, which indicates the distance of each voxel that constitutes the mineral from the background; the distance of those voxels that are directly adjacent to the background is zero and, hence, they are exposed to the surface.

In Figure 3.2, the image processing and quantitative analysis procedure are summarized in a flowchart.

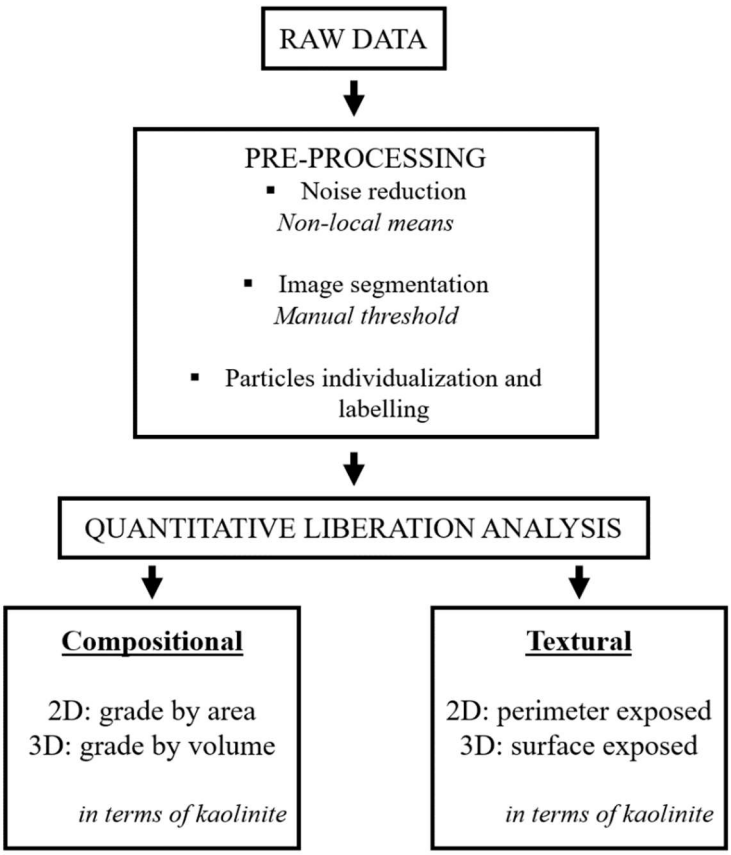

Figure 3.2. Flowchart describing the image processing procedure for quantitative liberation analysis.

Particle size distribution was also determined from image analysis. The diameter of each labeled particle was calculated by determining the longest distance between any two voxels within the particle, in 2D or 3D.

Particles containing less than 10 pixels of diameter (50μm) were excluded from the analysis to eliminate the influence of noise in the raw data. Approximately, 3.000 particles were studied.

3.3 Results and discussion

3.3.1 Mineralogical and chemical characterization

The bauxite semiquantitative chemical composition determined by XRF is expressed in Table 3.2 and the diffraction pattern with the identified peaks is displayed in Figure 3.3.

Table 3.2. Bauxite semiquantitative chemical composition by XRF (%).

SiO_2	Fe_2O_3	Al_2O_3	TiO_2	K_2O	CaO	ZrO_2	MgO	Cr_2O_3	LOI
22.86	23.63	35.15	3.27	0.03	0.06	0.08	0.02	0.05	14.84

Semiquantitative chemical composition suggested high content of silicon and aluminum. The loss on ignition was 14.84% and may be associated to the hydrated condition of the gibbsite. The semiquantitative analysis from XRD showed the presence of (54.5±1.0)% of gibbsite as the aluminum-bearing mineral, (39.8±1.0)% of kaolinite as silicate gangue, and (5.7±1.0)% of hematite. The XRD also indicated that a minor amount of quartz and goethite could also exist. This constitution agrees with the typical mineralogical assembly found in bauxite of tropical climates as the gibbsitic bauxite formed in northern Brazil.

Titrimetric and colorimetric analyses showed the presence of 15.2% available aluminum (AA) and 19.0% of reactive silica (RS), which represent the aluminum and silica that dissolves in a laboratory simulation of the Bayer process. The elevated amount of reactive silica corroborates with the high content of kaolinite, which is the silicate that is leached in the Bayer process.

Considering the feed requirement for the Bayer process of metallic aluminum production, the mineralogical characterization indicates that further mineral processing operations are necessary to increase AA/RS mass ratio.

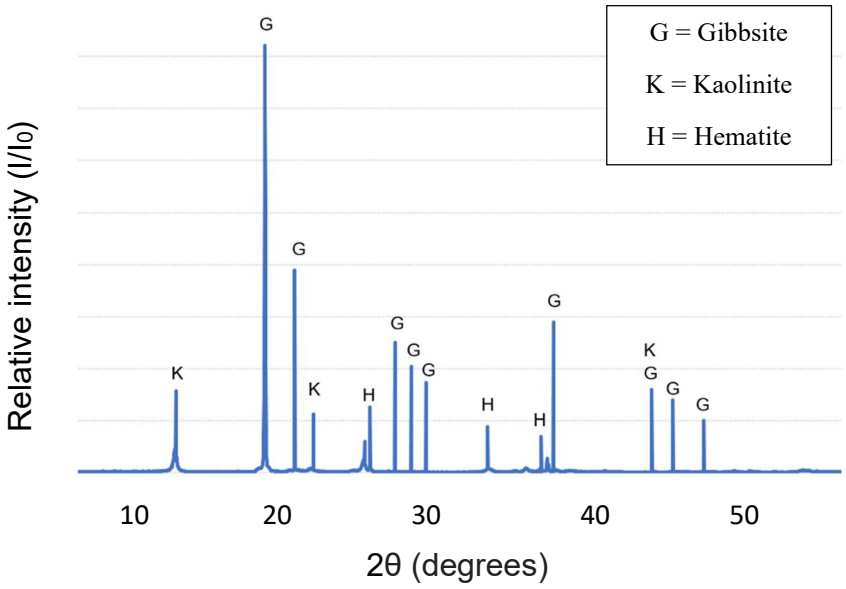

Figure 3.3. Indexed X-ray diffractogram of the bauxite sample. The semiquantitative analysis showed the presence of gibbsite, kaolinite, and hematite.

3.3.2 High-resolution X-ray microtomography

Figure 3.4 brings a cross-sectional image of the bauxite scanned, together with the graph of linear attenuation coefficient at different energies of the minerals that comprise the sample, plotted from the database created by Berger et al. (2009). The attenuation coefficients were simulated as weighted sums of the cross sections for the atomic constituents of each mineral phase. The μCT technique is based on the X-ray capability to penetrate distinct materials differently. The photons are attenuated as they travel through their path and the degree to which attenuation takes place is dependent on the linear attenuation coefficient of the materials (KETCHAM and CARLSON, 2001; CNUDDE and BOONE, 2013). Minerals containing low attenuation coefficient, such as gibbsite, appear as a darker gray shade in tomographic images. In contrast, hematite exhibits a high value of attenuation coefficient and appears as lighter shades. Kaolinite carries an intermediate coefficient and, hence, an intermediate gray level between gibbsite and hematite. The absence of attenuation would appear in black and mean porosity, which

was not significantly observed in this ore. The gray-level differentiation between gibbsite and kaolinite indicates that the μCT is a promising technique for determining mineral liberation with the sake of characterizing the ore for the reverse flotation of kaolinite from bauxite. Due to the small difference in their attenuation coefficients, kaolinite could not be distinguished from quartz, neither hematite from goethite. By any means, it does not affect the purpose of this study, as quartz and goethite are present only in very small amounts and are both gangue minerals.

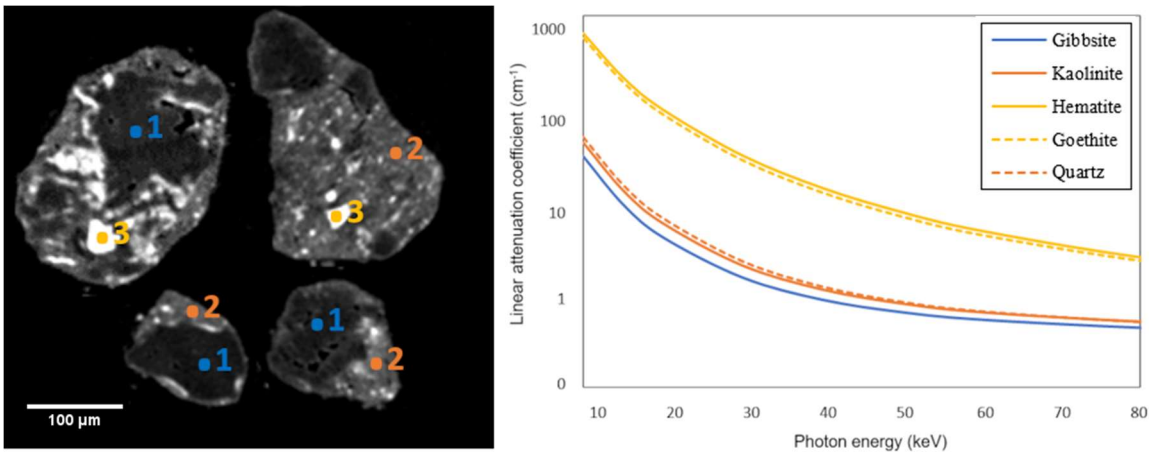

Figure 3.4. Cross-section tomographic image of bauxite indicating the minerals (1) gibbsite, (2) kaolinite, and (3) hematite; and their respective linear attenuation coefficients of X-rays at different photon energy. The higher the attenuation coefficient, the brighter it will appear in the image.

Phase quantification was also evaluated by μCT data to confirm the semiquantitative analysis assessed from the diffractogram. Table 3.3 brings a comparative of the results obtained by both XRD and μCT, showing a great agreement between them. The uncertainties of the quantitative analysis based on μCT were measured by calculating the average value and standard deviation of voxel intensities of the different phases. Then, minerals volume fractions were recalculated varying the user-defined threshold limits by subtracting and adding the standard deviation.

Table 3.3. Phase quantification assessed by XRD and μCT

Mineral phase	XRD (%)	Mineral phase	μCT (%)
Gibbsite	54.5 ± 1.0	Gibbsite	52.8 ± 0.9
Kaolinite	39.8 ± 1.0	Kaolinite	42.6 ± 0.9
Quartz	minor amount	Quartz	
Hematite	5.7 ± 1.0	Hematite	4.6 ± 0.9
Goethite	minor amount	Goethite	

In Figure 3.5, a three-dimensional reconstructed image of a selected region is presented. It is possible to notice small inclusions of hematite through the particles, as well as different mineral phases comprising the fragments surface. Only a few particles display larger diameters, ranging from 120μm to approximately 500μm. As liberation is related to particle size, these particles were excluded from the quantitative study of liberation to avoid any discrepancy that these elements could cause to the data analyzed. A detailed particle size distribution is provided in Figure 3.6, showing that 80% of the particles had diameter inferior to around 92μm. To perform liberation analysis, the sample was further subcategorized into two classes: Class A, from 50μm to 85μm; and Class B, from 85μm to 120μm. In this way, it was also able observe the impact of particle size in liberation.

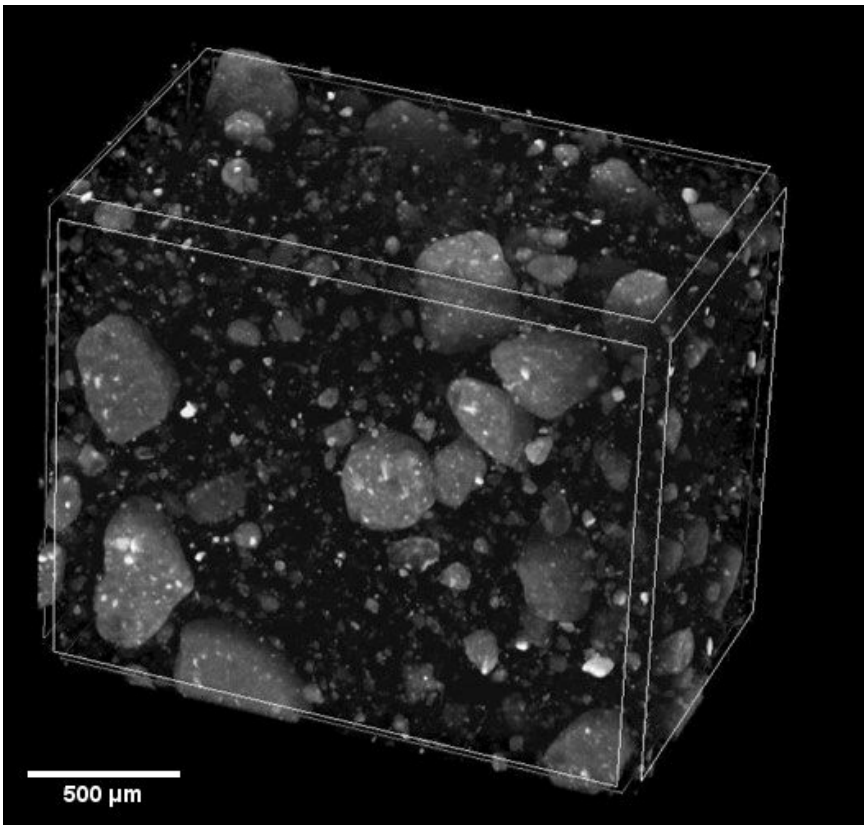

Figure 3.5. Three-dimensional image of the fragments scanned. We notice different size ranges and mineral phases comprising the particles surface.

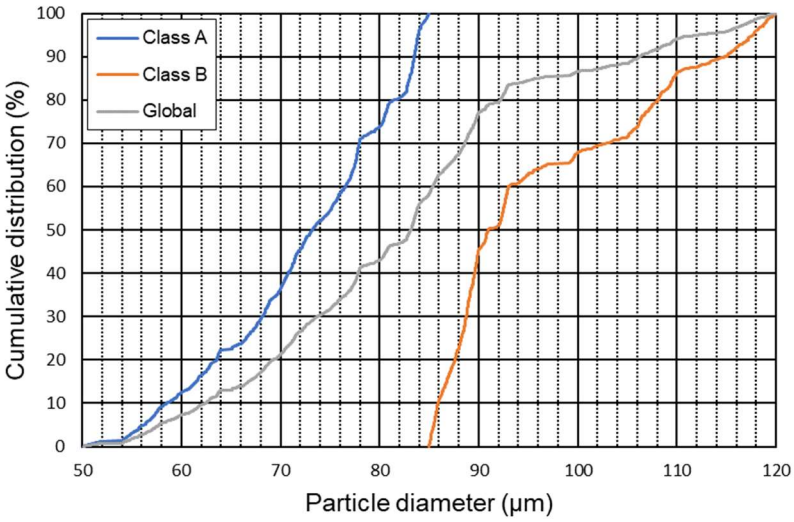

Figure 3.6. Particle size distribution by means of µCT diameter. 80% of the particles had diameter inferior to around 92µm.

3.3.3 Probing the 2D and 3D mineral liberation

The grade distributions using µCT for the bauxite sample are shown in Figure 3.7 and the surface exposure distributions are in Figure 3.8 (both Class A and Class B). Particles grades were calculated taking into consideration area of kaolinite over the total area of the particle for every slice through every fragment (2D perspective) and volume of kaolinite over the total volume of the particle (3D perspective). As pointed out by Reyes et al. (2018), because the integral of the 2D areas of each slice within the sample represents the 3D volume, distributions of grade in 2D and 3D are correspondent when all possible cross-sectional slices are considered. In Class A, there is the occurrence of more particles in the form of high-grade fragments. For instance, about 20% of the particles contain a grade higher than 80% in Class A, whereas, in Class B, this number is only 10%. This was predictable, as Class A has finer fragments and the finer the fragments, the higher the degree of liberation.

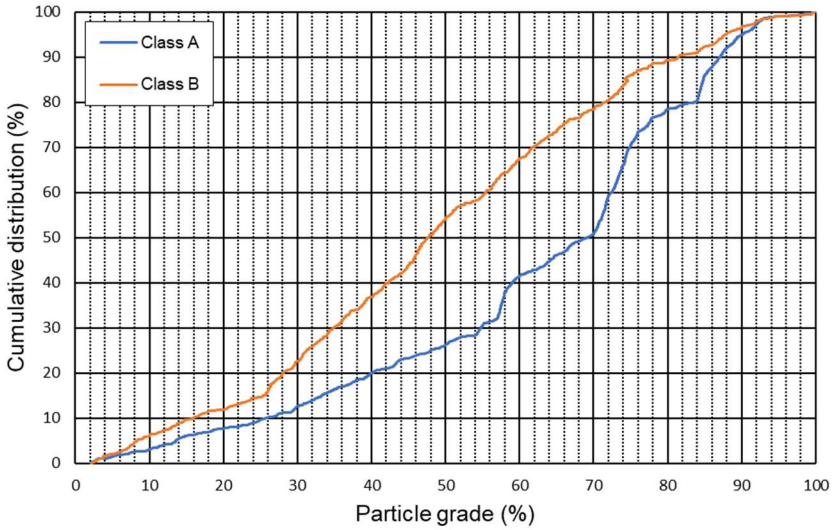

Figure 3.7. 2D and 3D grade distributions for both classes A and B. Because the integral of the 2D areas of each slice within the sample represents the 3D volume, distributions of grade in 2D and 3D are correspondent when all possible cross-sectional slices are considered.

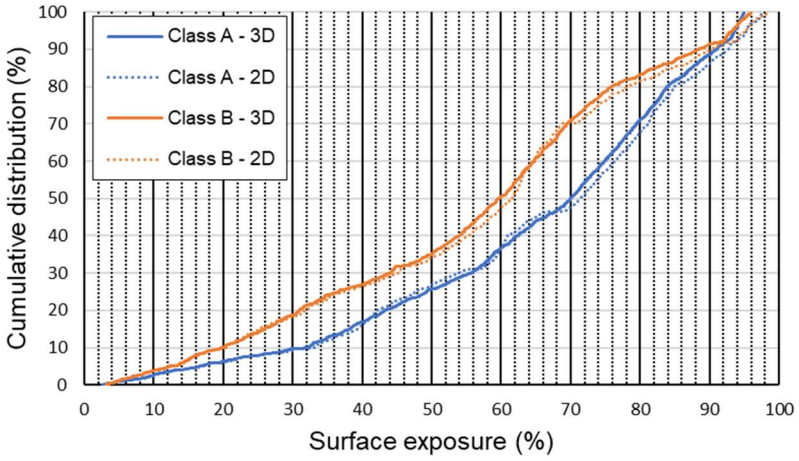

Figure 3.8. 2D and 3D surface exposure distributions for both classes A and B. There is a loss of three-dimensional information no matter how many slices or particles are examined.

On the other hand, 2D surface exposure does not converge exactly to the 3D view, even handling all the slices from the tomographic data. This fact evidences that there is a loss of three-dimensional information no matter how many slices or particles are examined (REYES et al, 2018). Nevertheless, the surface exposure distributions from both 2D and 3D data were practically similar to each other. The great issue at this point is that when traditional SEM-based techniques are applied to liberation analysis, virtually only one cross-section from each particle is acquired and much less fragments are analyzed. This will be further explored in Section 3.3.4. Analogous to particle grade, the finer the particles, the higher the surface exposure.

3D mineral surface exposure was plotted with respect to the volume grade in Figure 3.9. There is a directly proportional relation between them that can be described as a linear correlation with a coefficient of determination R^2 equal to 0.912. Measurement of exposed grain surface is of crucial relevance for mineral processing, especially in flotation, since it will help to define the most favorable operational parameters. However, it takes a lot of effort to measure it, even from 3D information. If there is a clear link between surface exposure and particle grade, as brought by Figure 3.9, then, it is possible to predict surface exposure by determining particle grade, which is a simpler task. It is important to stress, though, that the function is very specific to the ore and should not be extended to overall cases.

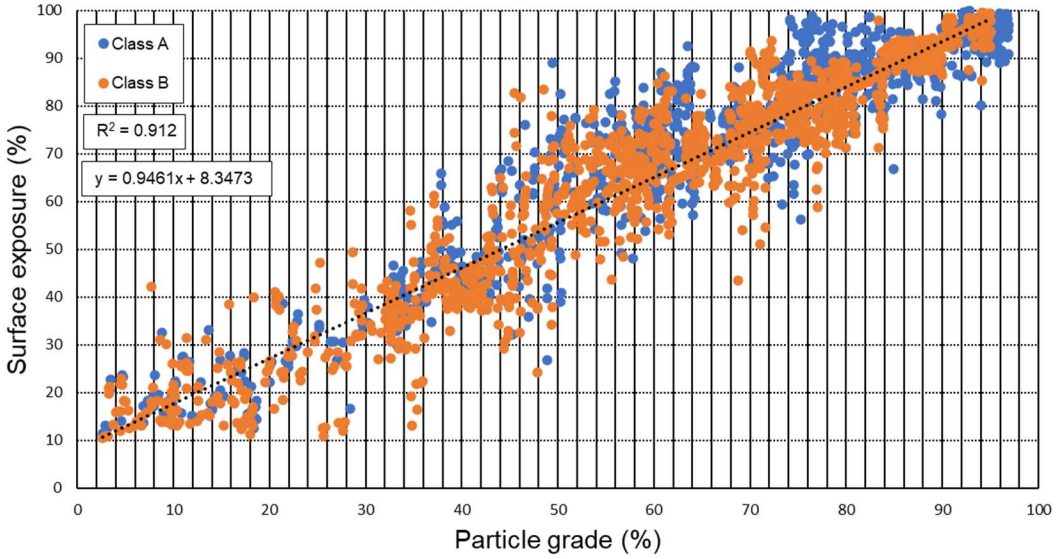

Figure 3.9. Particles surface exposure as a function of their grade. There is a directly proportional relation between them that can be described as a linear correlation.

To evaluate the grain size dependence of particle grade and surface exposure, the proportion of particles incident in narrow size classes for different ranges of grade and surface exposure were designed (Figure 3.10). Four ranges were considered: (a) 20-40%, (b) 40-60%, (c) 60-80%, and (d) 80-100%. As presumed, the incidence of finer fragments is higher at high ranges of grade and surface exposure. For the grades ranging from 80 to 100%, approximately half of the particles are concentrated in the first 4 size classes (from 50µm to 70µm). Oppositely, for the grades ranging from 20 to 40%, half of the particles contain a diameter between the upper 4 size classes (100µm and 120µm). The results also reveal the same behavior for surface exposure, that is, the particles containing the most ratio of kaolinite exposed surface area are in the finer classes. The extent of mineral liberation does not play an important role in Bayer process, as it does not affect the efficiency of bauxite digestion. However, a better understanding of bauxite liberation may guide us through the future challenges of implementing bauxite flotation. A great contribution would be to perform further research to analyze the feed and products of this sample after flotation experiments in terms of grade and surface exposure. This would help to define the optimum size class in which the operation would have the best efficiency, as well as, for example, avoid overgrinding of the ore.

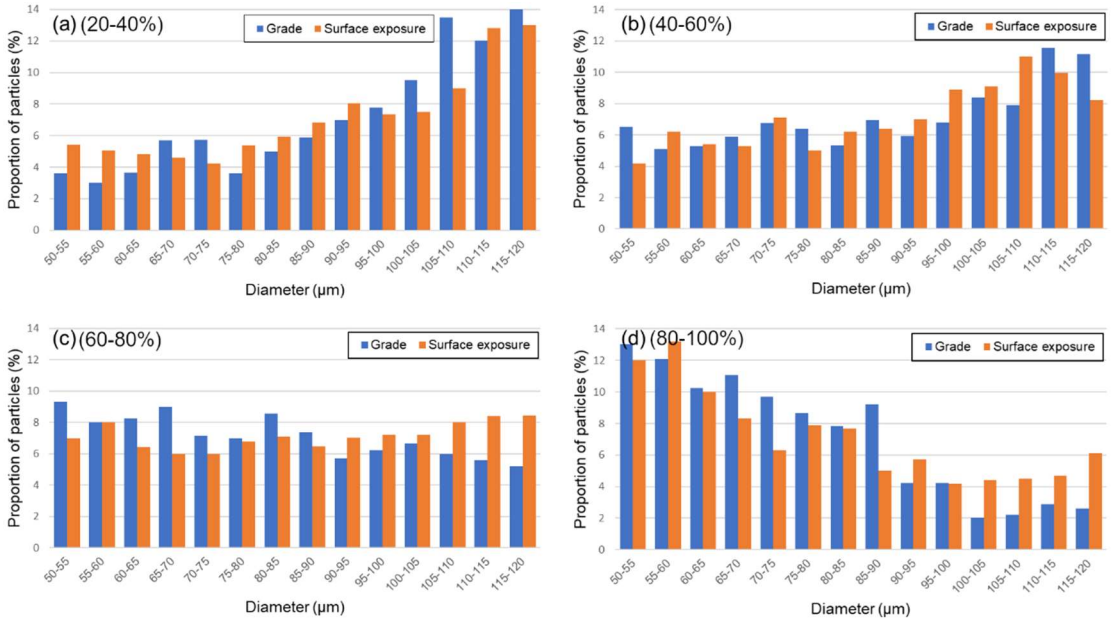

Figure 3.10. Proportion of particles occurring in different size classes for different ranges of grade and surface exposure (a) 20-40%, (b) 40-60%, (c) 60-80%, and (d) 80-100%. The particles containing the most ratio of kaolinite exposed surface area are in the finer classes.

3.3.4 Stereological bias

When performing mineral liberation analysis via traditional two-dimensional techniques such as SEM-based automated image analysis, practically only one slice from each fragment is acquired, as well as much less particles are examined. This is mainly due to the fact that the analyses are time-consuming and costly. Another reason is that sample preparation requires a lot of effort and involves a series of steps: the particles must be mounted in resin and, subsequently, the blocks must be carefully polished and receive a conductive coating. Conversely, µCT is able to scan a large number of particles in a single scan, providing statistical reliability, with the advantages of fast sample preparation and short scanning time.

To take a closer view in the magnitude of stereological bias, particle grade and surface exposure distributions were calculated from 2D data considering 9, 5, and 2 slices chose arbitrarily per fragment. In Figure 3.11, the results are plotted for each class and compared to the 3D distributions. Here, it was considered only the particles exhibiting grade and surface exposure in the range of 30% to 70%.

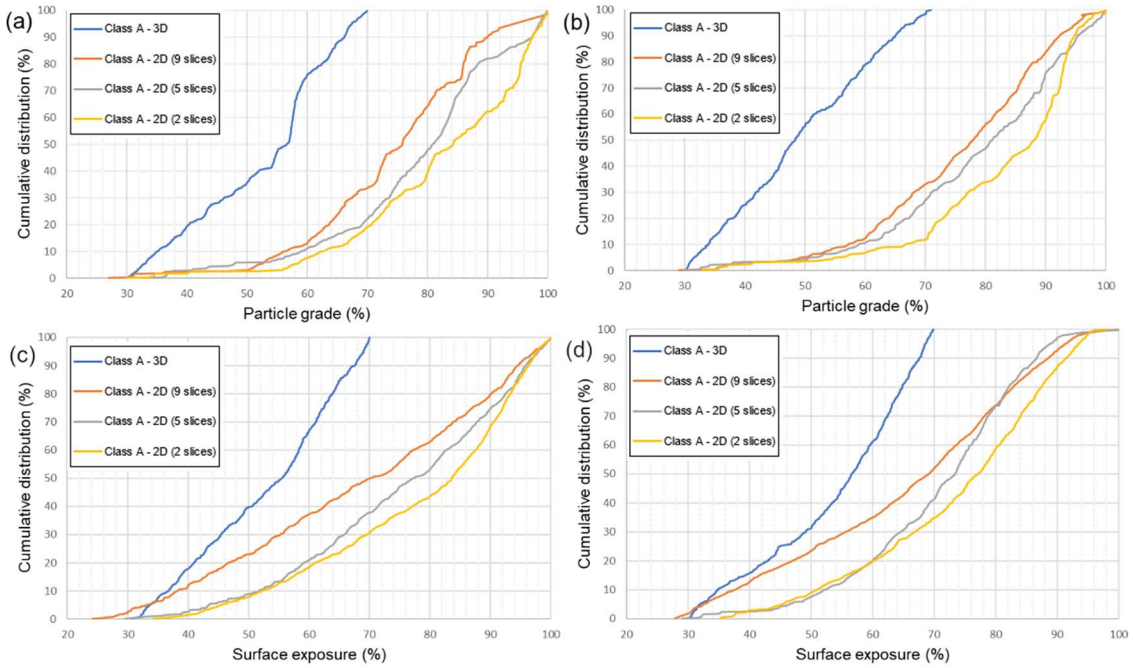

Figure 3.11. (a)(b) Particle grade and (c)(d) surface exposure distributions varying according to the number of slices used for classes A and B. The deviations in 2D and 3D measurements may be mainly attributed to the complexity of bauxite ore.

It is clear that 2D analysis overestimates the extent of grade and surface exposure, and it is more pronounced when less slices are considered. This can be explained by the fact that composite particles may appear to be liberated in 2D, whereas actually free particles will always appear locked in 2D (UEDA et al, 2018). In this context, particle characteristics such as aspect ratio, sphericity, and internal mineral structure, have an effect on stereological bias, that 3D visualization by X-ray microtomography is able to overcome. For instance, Ueda (2020) showed that the impact of internal structure was exceptionally significant when assessing surface exposure liberation. Considering that the investigated ore carries a complex structure, the deviations in 2D and 3D measurements may be mainly attributed to this complexity. In all cases, the 2D distributions indicated the existence of particles containing high grade and high surface exposure (>90%), when the truly values assessed by 3D visualization were 70% maximum. As previously discussed in Figure 3.8, specific for the case of exposed grain surface area, the 2D data does not converge to real 3D exposure no matter how may slices are observed.

Table 3.4 brings a summary of the mean particle grade and mean surface exposure calculated from all the perspectives. The standard deviations were calculated by varying the segmentation thresholds, similar as for phase quantification. When less slices are used, the loss of 3D information becomes more prominent. It is evident that 2D-based estimations are not accurate and should be corrected by stereological models. One of the consequences of grade and surface exposure overestimation is the misconception when designing mineral processing routes, leading to inefficient outcomes.

Table 3.4. Mean grade and surface exposure for each case.

Perspective	Grade – Class A (%)	Grade – Class B (%)	Surface exposure – Class A (%)	Surface exposure- Class B (%)
3D	52.57 ± 1.20	49.24 ± 1.33	53.01 ± 1.78	54.14 ± 2.00
2D – 9 slices	74.19 ± 1.25	75.74 ± 1.99	68.48 ± 2.05	65.75 ± 2.12
2D – 5 slices	78.22 ± 2.03	78.70 ± 2.05	75.37 ± 2.95	70.84 ± 3.03
2D – 2 slices	82.15 ± 2.12	82.84 ± 2.07	78.18 ± 3.30	73.85 ± 2.89

3.4 Conclusions

X-ray microtomography was implemented to investigate the mineral liberation of a gibbsitic bauxite based on 2D and 3D compositional and textural aspects of the particles.

The chemical and mineralogical characterization of the ore proved the existence of 54.4% of gibbsite, 39.8% of kaolinite, 5.7% of hematite, and minor amounts of goethite and quartz. The phase quantification was in agreement with volume fraction calculated by μCT. In light of Bayer process feed requirement, this suggests that concentration operations must be tested to increase AA/RS mass ratio.

As a consequence of differences in linear attenuation coefficient, gibbsite, kaolinite, and hematite could be easily distinguished by μCT and quantitative analysis of liberation could be effectively performed. Grade distributions in 2D and 3D were correspondent when all possible cross-sections were considered in 2D. However, 2D surface exposure did not converge accurately to the 3D fashion. No matter how many slices or particles are examined, there is a miscalculation caused by the loss of 3D

information. The results also indicated that there was a directly proportional relation between grade and surface exposure that can be described as a linear correlation.

The magnitude of stereological effect was assessed by varying the number of slices used in 2D calculations. It was clear that 2D analysis overestimates the degree of grade and surface exposure, being more pronounced when less cross-sections are used in the measurement. For instance, particle grade for Class A was overestimated from 52.57% (volumetric grade) to 74.19%, 78.22%, and 82.15% when, respectively, 9, 5, and, 2 slices were evaluated.

Our work proved that 2D-based estimations do not portray the real characteristics of mineral ores and stereological corrections should be applied. An accurate determination of grade and surface exposure is of great value in mineral processing industry, as it helps to optimize the efficiency of operations and makes better utilization of our mineral resources.

The X-ray microtomography has shown to be a solution to overcome the challenges of acquiring particles characteristics in three dimensions, even of ores exhibiting complex internal structure such as bauxite, as well as, a versatile tool which is able to determine different ore parameters such as volume fraction quantification, minerals liberation, and particle size distribution.

Acknowledgements

The authors are very thankful to Alcoa for providing the bauxite sample and to Mineração Curimbaba for conducting the XRF analysis. The financial support from the Brazilian research agency Coordenação de Aperfeiçoamento de Pessoal de Nível Superior (CAPES) is gratefully acknowledged. Finally, Guilherme José Ramos Oliveira is grateful to Conselho Nacional de Desenvolvimento Científico e Tecnológico (CNPq) for the research scholarship (140876/2019-7).

References

ABNT NBR 15944. Aluminium ores — Determination of usable alumina and reactive silica — Combined volumetric and colorimetric methods, 2011.

AYALA, J., FERNÁNDEZ, B. Treatment from abandoned mine landfill leachates. Adsorption technology. **Journal of Materials Research and Technology** 2019; 8:2732-2740.

BABISK, M.P. et al. Evaluation and application of sintered red mud and its incorporated clay ceramics as materials for building construction. **Journal of Materials Research and Technology** 2020; 9:2186-2195.

BARBOSA, F.M., BERGERMAN, M.G., HORTA, D.G. Removal of iron-bearing minerals from gibbsitic bauxite by direct froth flotation. **Tecnol. Metal. Mater. Min** 2016; 13:106-112.

BERGER, M.J. et al. XCOM: Photon Cross Sections Database Share, NIST Standard Reference Database 8 (XGAM); 2009.

CNUDDE, V., BOONE, M.N. High-resolution X-ray computed tomography in geosciences: A review of the current technology and applications. **Eartch-Sci Rev**. 2013; 123:1-17.

DILLINGER, B., BATCHELOR, A., KATRIB, J., DODDS, C. et al. Microwave digestion of gibbsite and bauxite in sodium hydroxide. **Hydrometallurgy** 2020; 192:105257.

EVANS, C.L. et al. Quantifying mineral grain size distributions for process modelling using X-ray micro-tomography. **Minerals Engineering** 2015; 82:78-83.

GAUDIN, A.M. Principles of Mineral Dressing. McGraw Hill. 1939. 554p.

GEN, H., CHANGCHUN, Z., JIONGTIAN, L. Effects of different factors during the de-silication of diaspore by direct flotation. **Int. J. of Mining Science and Technology** 2012; 22:341-344.

GIBSON, B., WONYEN, D.G., CHELGANI, S.C. A review of pretreatment of diasporic bauxite ores by flotation separation. **Minerals Engineering** 2017; 114:64-73.

KETCHAM, R., CARLSON, W. Acquisition, optimization and interpretation of X-ray computed tomographic imagery: applications to the geosciences. **Computers and Geosciences** 2001; 27:381-400.

KING, R.P., SCHNEIDER, C.L. Stereological correction of linear grade distributions for mineral liberation. **Powder Technology** 1998; 98:21-37.

LAITINEN, O. et al. Alkyl aminated nanocelluloses in selective flotation of aluminium oxide and quartz. **Chemical Engineering Science** 2016; 144:260-266.

LEIGH, G.M. et al. Stereological estimates of liberation from mineral section measurements: a rederivation of Barbery's formulae with extensions, **Powder Technology** 1996; 87:141–152.

LEISSNER, T. et al. Evaluation of mineral processing by assessment of liberation and upgrading. **Minerals Engineering** 2013; 53:171-173.

LIN, C.L., MILLER, J.D. Cone beam X-ray microtomography for three-dimensional liberation analysis in the 21st century. **Int. J. of Mineral Processing** 1996; 47:61-73.

LIN, C.L., MILLER, J.D. Cone beam X-ray microtomography-a new facility for three-dimensional analysis of multiphase materials. **Mining, Metallurgy and Exploration** 2002; 19:65-71.

LIN, C.L., MILLER, J.D. 3D characterization and analysis of particle shape using X-ray microtomography (XMT). **Powder Technology** 2005; 154:61-69.

LIU, J., WANG, X., LIN, C., MILLER, J.D. Alkyl aminated nanocelluloses in selective flotation of aluminium oxide and quartz. **Minerals Engineering** 2015; 78:58-65.

LIU, Z. et al. Digestion behavior and removal of sulfur in high-sulfur bauxite during Bayer process. **Minerals Engineering** 2020; 149:106237.

MARINO, S.L. The flotation of marginal gibbsitic bauxite ores from Paragominas-Brazil. [M.Sc. dissertation]. Utah: The University of Utah;2012.

MELO, C.C.A., ANGÉLICA, R.S., PAZ, S.P.A. A proposal for rapid grade control of gibbsitic bauxites using multivariate statistics on XRD data. **Minerals Engineering** 2020; 157:106539.

MILLER, J.D., LIN, C.L. Treatment of polished section data for detailed liberation analysis. **Int. Journal of Mineral Processing 1988**; 22:41-58.

REYES, F. et al. Quantifying mineral liberation by particle grade and surface exposure using X-ray microCT. **Minerals Engineering** 2018; 125: 75-82.

REYES, F. et al. Calibrated X-ray micro-tomography for mineral ore quantification. **Minerals Engineering** 2017; 110:122-130.

RODRIGUES, O.M.S. et al. Kaolinite removal from bauxite by flotation. **REM: Int. Eng. J.** 2016; 69:349-353.

SAMPAIO, J.A., ANDRADE, M.C., DUTRA, A.J.B. Bauxita. In: Luz AB, Lins FAF, editors. Rochas e minerais industriais: usos e especificações. 2ed. ed. CETEM. 2008. p. 311-338.

SMITH, P. The processing of high silica bauxites — Review of existing and potential processes. **Hydrometallurgy** 2009; 98:162-176.

TABERAUX, A.T., PETERSON, R.D. Aluminum Production. In: Seetharaman S, editor. Treatise on Process Metallurgy. Elsevier. 2014. p.839-917.

TREIMER, W. Imaging. In: Staron P, Schreyer A, Clemens H, Mayer S, editors. Neutrons and Synchrotron Radiation in Engineering Materials Science. 2ed. Wiley VCH. 2017. p.227-252.

UEDA, T., OKI, T., KOYANAKA, S. Experimental analysis of mineral liberation and stereological bias based on X-ray computed tomography and artificial binary particles. **Adv. Powder Technology** 2018; 29:462-470.

UEDA, T. Experimental validation of a statistical reliability method for the liberation distribution measurement of ore particles. **Minerals Engineering** 2019; 140:105880.

UEDA, T. Experimental study on the stereological bias in surface exposure measurement of ore particles. **Advanced Powder Technology** 2020; 31:61-69.

WANG, Y. Image Processing Techniques for Three-dimensional Analysis of Multiphase Multi-size Packed Particle Beds Using X-ray Tomography. [PhD thesis]. Utah: The University of Utah; 2016.

WANG, Y., LIN, C.L., MILLER, J.D. Quantitative analysis of exposed grain surface area for multiphase particles using X-ray microtomography. **Powder Technology** 2017; 308:368-377.

WANG, Y. et al. Stereological correction of perimeter-based estimates of exposed grain surface area. **Minerals Engineering** 2018; 126:64-73.

WANG, Y. et al Mineral transformation in treating low-grade bauxite using the calcification–carbonization process and preparing cement clinker with the obtained residue. **Minerals Engineering** 2019; 138:139-147.

XU, L. et al. Anisotropic adsorption of oleate on diaspore and kaolinite crystals: Implications for their flotation separation. **Applied Surface Science** 2014; 321:331-338.

XU, Y., CHEN, C., LAN, Y., WANG, L., LI, J. Desilication and recycling of alkali-silicate solution seeded with red mud for low-grade bauxite utilization. **Journal of Materials Research and Technology** 2020; 9:7418-7426.

CHAPTER 4

PROBING THE APPLICABILITY OF X-RAY MICROTOMOGRAPHY FOR MINERAL LIBERATION DETERMINATION OF AN IRON ORE TAILING

ABSTRACT

In mineral processing, a detailed characterization of multiphase particulate systems is fundamental to guarantee an efficient concentration of valuable minerals. A precise analysis allows the process engineer, for instance, to evaluate the optimum concentration route and to achieve the best possible metallurgical recovery. One of the most important aspects of the ore is mineral liberation, as it defines the maximum possible grade of concentrates. Scanning electron microscope-based (SEM-based) automated image analysis systems have been used to obtain information concerning mineral liberation. One of the limitations of SEM-based techniques is the unavoidable loss of 3D information, leading to significant stereological errors. In this regard, X-ray microtomography (μCT) emerges as a solution that allows three-dimensional imaging and direct measurement of spatial characteristics of particles, eliminating stereological issues. In this work, we used high-resolution X-ray microtomography to evaluate the characteristics of liberation of an iron ore concentration tailing containing about 88.8% of quartz, 10.4% of hematite, and 0.8% of goethite. The analysis was carried out with respect to compositional liberation (grade) and textural liberation (surface exposure), in both 2D and 3D perspectives to assess the degree of stereological bias. Both parameters, grade and surface exposure, have been overestimated by the 2D assessment. The stereological effect was more pronounced in surface exposure quantification. We found a linear relationship between (i) grade and surface exposure and (ii) particle size and surface exposure. A comparison of TIMA and μCT (2D and 3D) evidenced the fact that only a 3D technique is able to represent the real characteristics of particulate systems.

4.1 Introduction

In mineral processing, a detailed characterization of multiphase particulate systems is fundamental to guarantee an efficient separation of the valuable minerals. A precise analysis allows the process engineer, for instance, to evaluate the optimum concentration route and to achieve the highest possible metallurgical recovery (WILLS and FINCH, 2016; WANG et al., 2018). The points of major interest in ore characterization are the mineralogical and chemical composition of the particles, as well as the spatial distribution of different minerals within the particles (FURAT et al., 2018).

One of the most important aspects of the ore is mineral liberation, as it defines the maximum possible grade of concentration products (LEISSNER et al., 2013). It can be expressed as the fraction of the liberated particles of a given mineral over the total amount of the ore – degree of liberation – or, as the cumulative distribution of particles with respect to their content of the mineral of interest – liberation distribution (UEDA et al., 2018). In an industrial practice, liberation is achieved by means of comminution operations, which are highly energy-intensive. Hence, a reliable determination is important to avoid overgrinding, which, in consequence, minimizes the energy and costs required for mineral processing (WANG et al., 2018; GHOLAMI et al., 2020).

Scanning electron microscope-based (SEM-based) automated image analysis systems, such as Mineral Liberation Analyzer (MLA) and TESCAN Integrated Mineral Analyzer (TIMA), have been used to obtain information concerning mineral liberation. These systems combine scanning electron microscopy (SEM) and energy-dispersive X-ray spectroscopy (EDS), and have enabled simultaneous acquisition of morphological and compositional data automatically, identifying and visualizing a great number of particles (REYES et al., 2017).

However, SEM-based techniques presents a relevant limitation for mineral liberation assessment that is the unavoidable loss of 3D information, leading to significant stereological errors. The liberation measurement from 2D polished sections usually overestimates the extent of liberation, because locked particles may appear to be liberated in 2D, whereas real free particles will always seem liberated (REYES et al., 2018; UEDA et al., 2018; WANG et al., 2018). There have been many studies aiming to correct the stereological effect of the degree of liberation, most of them relying on simulation and

mathematical modelling (MILLER and LIN, 1988; KING and SCHNEIDER, 1998; FANDRICH et al., 1998; ZHANG and SUBASINGHE, 2013; VAN DER WIELEN and ROLLINSON, 2016), but the models are usually very specific for the ore investigated and corrections for more than two phases are complex (WANG et al., 2018).

X-ray microtomography (μCT) emerges as a solution that allows three-dimensional imaging and direct measurement of spatial characteristics of particles, eliminating stereological issues (REYES et al., 2018). The technique is based on the attenuation of X-ray photons as they pass through the sample and interact with it. The extent to which attenuation takes place is dependent on the linear attenuation coefficients of the minerals and varies linearly with density. Materials of different densities and chemical compositions will exhibit different outcomes, where each voxel (3D pixel) represents the photon attenuation at a given point (KETCHAM and CARLSON, 2001; LANDIS and KEANE, 2010; BAKER et al., 2012; CNUDDE and BOONE, 2013). However, there is a lack of published works on this subject.

The first relevant investigations date back to the end of the 1990s (LIN and MILLER, 1996; 2002; 2005), when limitations of spatial resolution did not allow to perform deep investigations. These works, however, paved the way to a more comprehensive understanding of μCT capabilities. More recent advances include Wang et al. (2017) and Wang et al. (2018), who investigated mineral liberation and surface exposure of an auriferous pyrite ore for flotation purposes; and assessed perimeter-based liberation of a low-grade copper ore comparing to results of a SEM-based system, respectively. Reyes et al. (2017) combined μCT and SEM images to perform a deep mineral characterization and determine mineral liberation. Reyes et al. (2018) examined the three-dimensional characteristics of grade and exposed grain surface of a copper ore. Ueda et al. (2018) and Ueda (2019) scanned artificial particles by μCT and proposed a method for stereological correction based on 2D and 3D information.

In this work, we used high-resolution μCT to evaluate the characteristics of liberation of an iron ore tailing. The analysis was carried out with respect to compositional liberation (grade) and textural liberation (surface exposure). The tomographic data was analyzed in both 2D and 3D perspectives to assess the degree of stereological bias. Additionally, we employed TESCAN Integrated Mineral Analyzer (TIMA), a SEM-

based technique for mineral liberation assessment, and compared to the results obtained by μCT.

Three-dimensional characterization of multiphase particles using μCT has been of growing interest of mineral processing and extractive metallurgy industries, and this work brings major contributions towards the consolidation of the technique in the mineral processing field.

4.2 Materials and methods

The investigated sample is a sandy waste from froth flotation of an iron ore from The Brazilian Iron Quadrangle, located in Minas Gerais state. The size analysis, determined by wet sieving, indicated that its granulometry is 90% passing 120μm. The sample was submitted to chemical and mineralogical characterization, high-resolution microtomography and TIMA experiments.

4.2.1 Chemical and mineralogical characterization

The semiquantitative chemical analysis of the iron ore tailing was evaluated for a pulverized aliquot by X-ray fluorescence (XRF) in a Panalytical Zetium spectrometer.

Mineralogical characterization was performed by powder X-ray diffraction (XRD) using a D2 Phaser diffractometer by Bruker. To avoid preferential orientation, the ground sample was prepared with backload hand mount. The equipment is available at the Nanotechnology Laboratory (NanoLab), a laboratory part of the Department of Metallurgical and Materials Engineering of the Federal University of Ouro Preto. An X-ray wavelength of 1.5406Å (Cu K-α), with 2θ varying from 0 to 90º and a step size of 0.018º was used. The mineral phases were identified by means of the software solution *Match!*, based on the Crystallography Open Database (COD). Semiquantitative phase quantification was also determined by *Match!* by running an automatic refinement based on the relative intensity of the peaks (I/I_0). The mineral phases were selected based on the figure-of-merit (i.e. quality of the matching) as well as on a visual inspection of their agreement with the experimental diffractogram pattern.

The mineralogical assembly was also assessed by TIMA using Energy-dispersive X-ray Spectroscopy (EDS). The mineral phases were identified taking into consideration the database developed by researchers from NanoLab (SILVA et al., 2020; PIRES et al.,

2019; SAMPAIO N. et al., 2018). Details on sample preparation and experimental conditions are presented in Section 4.2.4.

4.2.2 High-resolution X-ray microtomography

The particles were placed in an acrylic tube of about 6mm inner diameter and 10mm in height. The μCT experiments were performed at NanoLab in a Bruker Skyscan 1272 microtomography scanner. The images achieved a voxel size of 5.0μm. A 0.5mm-thick aluminum filter was used to eliminate beam-hardening artifacts. The experimental conditions are summarized in Table 4.1.

Table 4.1. Experimental conditions used in the tomographic experiments.

Table 1: Experimental conditions used in the tomographic experiments.	
Instrument	Skyscan 1272 - Bruker
Pixel size (μm)	5.0
Exposure time (s)	2
Number of projections	1600
Energy/Current	90kV/100μA
Source-to-object distance (mm)	46.46
Source-to-detector distance (mm)	272.43
Source spot size (μm)	<5
Detector/Resolution	CCD camera/16Mp
Detector pixel size (μm)	7.4
Filter	0.5mm Aluminum

4.2.3 Image processing and liberation assessment by μCT

The quantitative analysis of μCT data is not straightforward and takes a series of stages that must be executed carefully. First, to smooth images and enhance quality, a non-local means denoising filter was applied. An intensity threshold based on the gray-level of the images was manually defined and mineral phases were segmented. Both procedures were performed in the freeware ImageJ.

Following, isolated particles were identified by an object separation algorithm, where each one received a unique label, and quantitative analyses performed. The quantitative analysis was carried out in the software CTAn (Bruker) which offers a semi-automatic custom processing function, allowing the operator to create analysis routines and saving processing time.

The 3D liberation distributions were calculated based on compositional and textural characteristics of the fragments. In the reverse flotation of silicates from iron ore, quartz is collected in the froth. Therefore, liberation was assessed in terms of this mineral. For the compositional distribution, the quartz grade of each particle was calculated dividing the volume of quartz by the volume of the whole particle. In image analysis, the estimation of the volume of an object consists in counting the number of voxels that makes up the object multiplied by the volume of an individual voxel. The liberation distribution based on textural characteristics was measured regarding surface area, a critical parameter to predict flotation efficiency and reagents dosage. For each particle, it was calculated the ratio of exposed surface area of quartz in relation to the total surface area of the particle. Similarly, area is calculated by multiplying the number of pixels that constitute the area by the area of one single pixel. To assess the exposed surface area of quartz, firstly, it was necessary to define the voxels that were associated to the background and not to other mineral phases. This was done by creating a distance map, which indicated the distance of each voxel from the background. Voxels that were directly adjacent to the background was zero distant, hence, they were exposed to the surface.

To have an indicative of the magnitude of stereological effects, liberation was also calculated in 2D from tomographic data considering only one single slice per fragment, analogous to what would occur in a SEM-based system. Grade and surface exposure were calculated in terms of, respectively, area and perimeter exposed. The image processing routine is summarized in Figure 4.1.

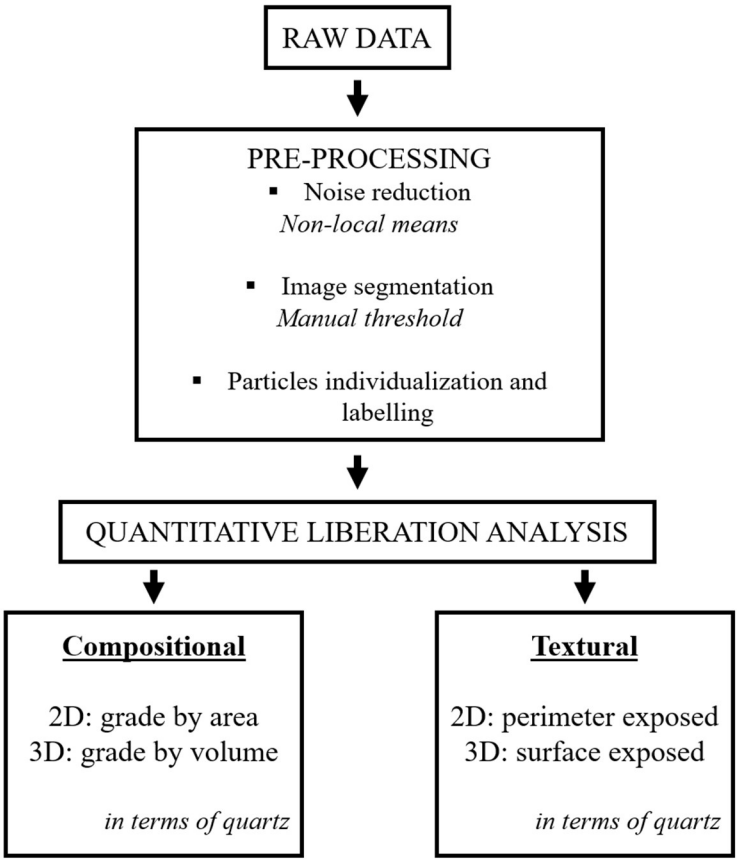

Figure 4.1. Flowchart describing the image processing procedure for quantitative liberation analysis.

Particle size distributions in 2D and 3D were determined from image analysis. The diameter of each labeled particle was calculated by determining the longest distance between any two voxels within the particle.

Particles exhibiting diameter inferior to 50µm (10 pixels) were excluded from the study to eliminate the influence of noise in the raw data, unless otherwise indicated.

4.2.4 TESCAN Integrated Mineral Analyzer (TIMA)

TIMA is a SEM-based system especially designed for use in mineral processing industry to determine mineral liberation from samples of feeds, concentrates, and tailings. It was used for mineralogical characterization and to assess mineral liberation. The mineral particles were mounted in acrylic resin, forming discs of, approximately, 25mm in diameter. The discs were, then, carefully polished and coated with a conductive carbon layer. The experimental conditions are expressed in Table 4.2.

Table 4.2. Experimental conditions used in the TIMA scanning.

Detector mode	Backscattered electrons
Beam energy	25keV
Probe current	5.09nA
Beam intensity	18.98
Spot size	81nm
Working distance	15mm
Acquisition mode	Dot mapping
Pixel size	3.0μm

The liberation reported by the equipment was given in terms of exposed perimeter. As our aim was to compare the data obtained by both μCT and TIMA rather than reporting the liberation status of the waste, we did not separate the sample in size ranges as usually done in SEM-based analysis.

4.3. Results and discussions

4.3.1 Chemical and mineralogical characterization

The semiquantitative chemical composition of the sandy waste determined by XRF is given in Table 4.3 and the indexed diffractogram is brought in Figure 4.2.

Table 4.3. Iron ore tailing semiquantitative chemical composition by XRF (%).

SiO_2	Fe_2O_3	Al_2O_3	TiO_2	K_2O	CaO	ZrO_2	MgO	Cr_2O_3	P_2O_5	Na_2O
82.97	15.88	0.30	0.01	<0.01	0.01	0.01	<0.1	0.03	0.01	<0.1

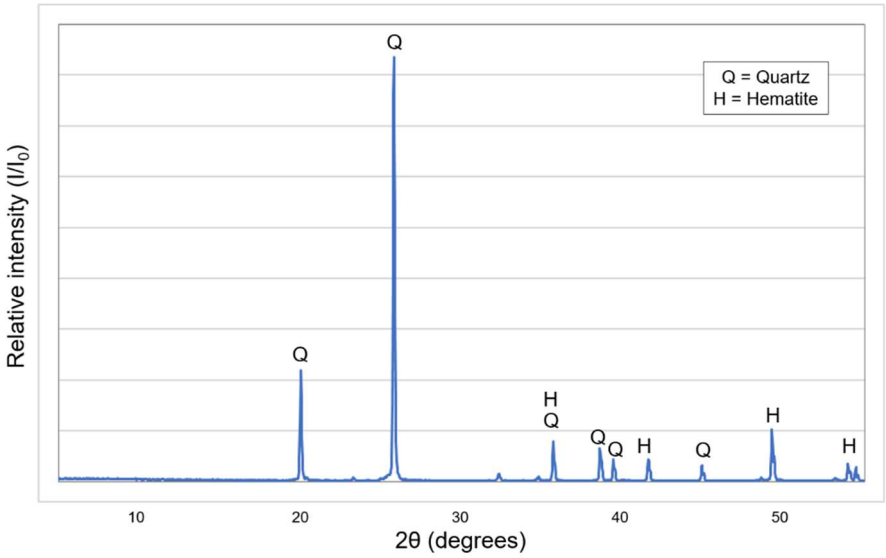

Figure 4.2. Indexed X-ray diffractogram of the iron ore tailing sample. Semiquantitative analysis revealed that the sample was composed by 88.8% of quartz, 10.4% of hematite, and 0.8% of goethite.

Semiquantitative analysis by XRF indicates that the ore presents high silica (82.97%) and low iron (15.88%) contents, which is expected from an iron ore flotation tailing. The phase quantification from the semiquantitative analysis of the diffractogram showed that the sample was composed by 88.8% of quartz, 10.4% of hematite, and 0.8% of goethite.

The mineralogical phase quantification by TIMA exhibited 86.40% of quartz, 8.59% of hematite/magnetite, 3.29% of goethite, and minor amounts of siderite, kaolinite, grunerite, greenalite, diaspore, and muscovite. 1.27% of the mineral phases were unclassified. Hematite and magnetite are classified as a single phase (hematite/magnetite) due to the difficulties of the technique in distinguishing these phases. In addition to the similar contrast in backscattered electrons (BSE) images, both minerals carry similar characteristic X-ray spectra detected by EDS. Figure 4.3 brings a cross-section image obtained by TIMA with the respective mineral phases identified, showing clearly that it is mainly composed by quartz and hematite/magnetite.

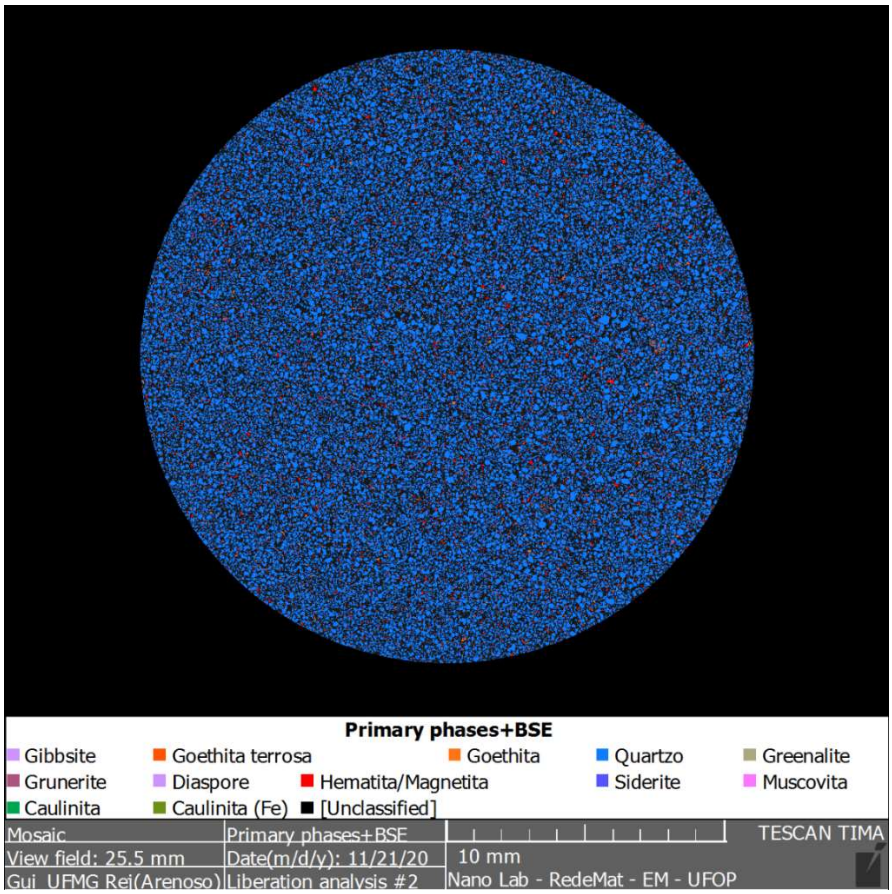

Figure 4.3. Cross-section image obtained by TIMA with the respective mineral phases identified. The main phases were 86.40% of quartz, 8.59% of hematite/magnetite, 3.29% of goethite.

4.3.2 High-resolution X-ray microtomography

As aforementioned, the μCT technique is based on the attenuation of photons and this phenomenon depends on the linear attenuation coefficient of the minerals. The higher the coefficient, the more attenuated the X-ray will be. In the reconstructed image, specimens presenting lower attenuation coefficient will appear darker in comparison to those carrying a high value of attenuation coefficient. The linear attenuation coefficients of quartz, hematite, and goethite are represented in Figure 4.4, which were simulated as weighted sums of the cross sections for the elements that constitute each mineral phase based on the database developed by Berger et al (2010). Due to only a minor difference in their attenuation coefficients, hematite cannot be distinguished from goethite.

However, it does not influence on the aim of this study, as the focus of this work is liberation between quartz and iron-bearing minerals.

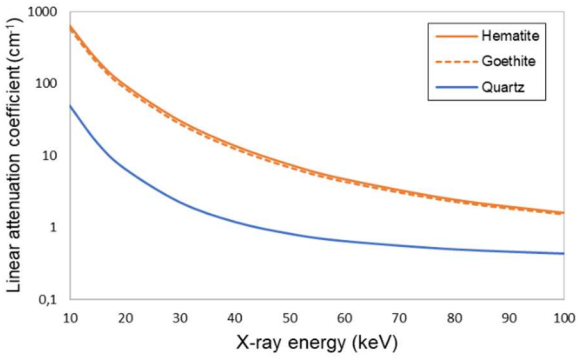

Figure 4.4. Linear attenuation coefficients of X-rays at different energies for quartz, hematite, and goethite. They were calculated as weighted sums of the cross sections for the elements that constitute each mineral phase.

Figure 4.5 brings a cross-sectional image exhibiting great quality of three different regions within the volumes analyzed. Aside the background (in black), we can distinguish two gray-levels: The darker one corresponds to quartz and the lighter one to hematite. It is possible to notice fully liberated quartz particles, as well as mixed particles containing different proportions of hematite. In total, approximately 6.200 particles were scanned, 1.004 of which were composite (about 16.2%). The fully liberated quartz fragments were excluded from the analysis.

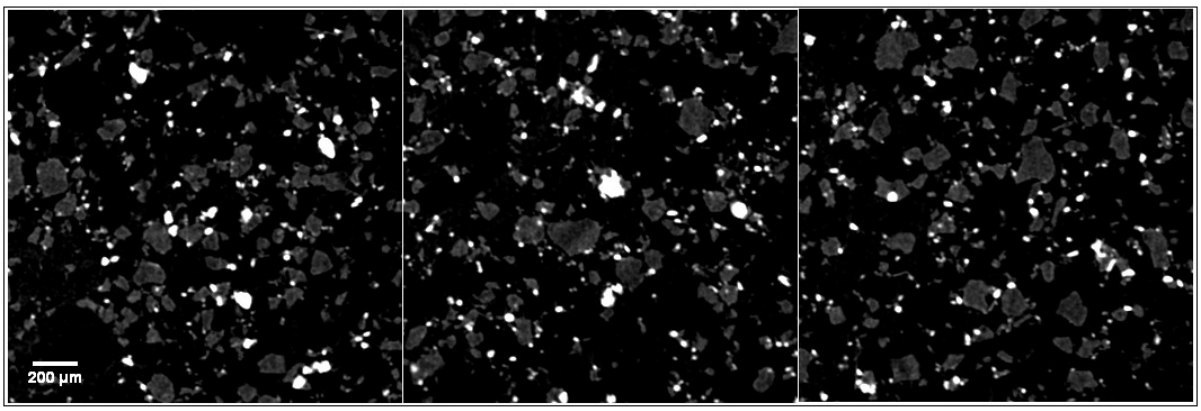

Figure 4.5. Cross-section tomographic image of the iron ore tailing. Quartz exhibits lower attenuation coefficient and, hence, appear as a darker shade in the tomographic image.

Phase quantification was determined by µCT as well, considering all the 6.200 particles and also considering only the 1.004 mixed particles. The results are expressed in Table 4.4. The composition for the global sample agrees with the quantitative analysis performed by XRD and TIMA. In the scenario where the liberated quartz particles were removed from the calculation, the proportion of iron-bearing minerals increased from 9.7% to 40.8%.

Table 4.4. Phase quantification assessed by µCT.

Mineral phase	Global (%)	Mixed particles only (%)
Quartz	90.3 ± 1.0	59.2 ± 1.0
Iron-bearing minerals	9.7 ± 1.0	40.8 ± 1.0

From the tomographic data, the grain size distribution was plotted from 3D observation and also considering only one single random slice of each particle (2D analysis) (Figure 4.6). There is a shape dependence on the stereological bias observed for grain size, hence, the grain distribution can be either over or underestimated in 2D. Particles containing diameter inferior to about 95µm in 3D appeared to have had their size underestimated. At the same time, the proportion of particles with diameter greater than 100µm increased.

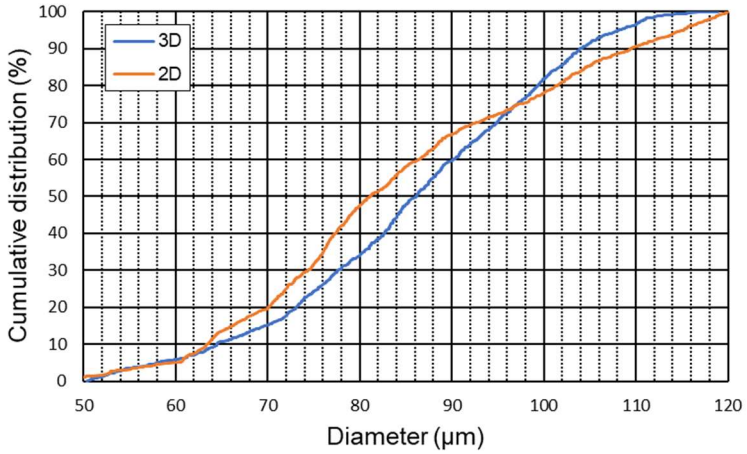

Figure 4.6. Particle size distribution in 2D and 3D assessed by µCT. Particles containing diameter inferior to about 95µm in 3D appeared to have had their size underestimated.

4.3.3 3D and 2D mineral liberation assessment by µCT

Mineral liberation was measured in 3D in two different fashions: liberation by particle grade and liberation by exposed grain surface. To study the magnitude of stereological bias, 2D liberation distributions were also calculated observing only one single slice from each particle. For the 2D perspective, it was considered grade by area and exposed grain surface by perimeter exposed.

Figures 4.7 and 4.8 bring, respectively, particle grade distribution and surface exposure distribution with respect to quartz for the iron ore tailing calculated in 2D and 3D.

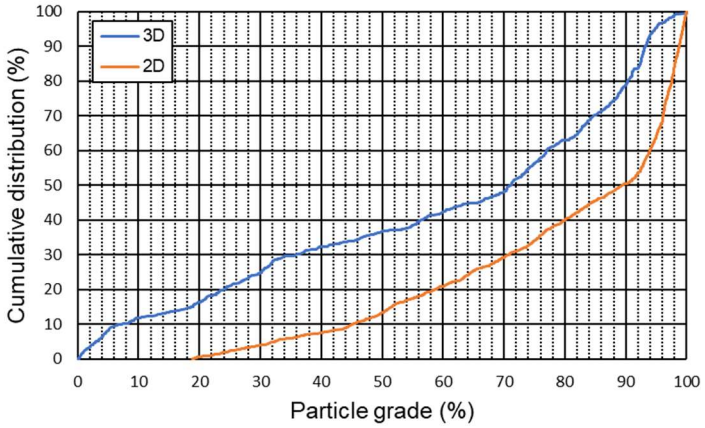

Figure 4.7. 3D and 2D grade distributions measured by µCT showing the stereological bias associated to 2D measurements. According to 2D liberation, 50% of the particles were contained in the range from 90% to 99.5% of quartz, whereas only 20% were truly high-grade fragments.

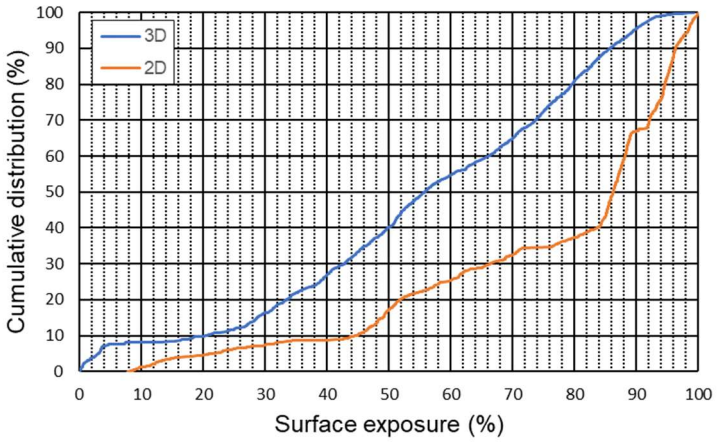

Figure 4.8. 3D and 2D surface exposure distributions measured by µCT. The stereological effects seemed to be more pronounced in surface exposure quantification.

For both grade and surface exposure there have been an overestimation in their degrees. In principle, stereological bias of mineral liberation usually overestimates the degree of liberation, because locked particles may seem liberated in 2D, but liberated particles will never appear locked in 2D observations. In the case of particle grade, for example, the 2D distribution indicated that there were no particles with less than 18% of quartz. When we take a look at the 3D distribution, though, we notice that about 15% of the particles presented a grade of 18% or inferior. Focusing on the high-grade particles (from 90% to 99.5% of quartz), according to 2D liberation, 50% of the particles were contained in this range, whereas only 20% were truly high-grade fragments. The stereological effects seemed to be more pronounced in surface exposure quantification. For instance, 2D distribution showed that more than 60% of the particles had a surface exposure varying from 80% to nearly 100%. However, the 3D distribution revealed that approximately 20% of the particles exhibited exposed grain surface higher than 80%.

These results elucidate the necessity of assessing mineral liberation three-dimensionally and developing new correction models for SEM-based systems. The extent of the bias can be reduced if more slices are considered in 2D analysis, as showed by Reyes et al. (2018). However, it is practically impossible to analyze more than one cross-section per particle in conventional microscope-based equipment. As also stated by Reyes et al. (2018), if every slice possible through every fragment were considered, the grade distributions in 2D and 3D would be correspondent, as the integral of the 2D areas of each

slice represents the 3D volume. However, 2D surface exposure would not converge exactly to the 3D distribution, i.e., it does not matter how many cross-sectional images are observed, there will always be a loss of 3D information.

In Figures 4.9 and 4.10, it is displayed the surface exposure with respect to, respectively, particle grade and particle size. From Figure 4.8, we observe a linear relationship between grade and surface exposure, with $R^2 = 0.9219$. There are a considerable number of particles with low grade and low surface exposure, i.e., particles that are virtually composed entirely by hematite. Nevertheless, these particles were able to be collected and floated in the beneficiation process. One of the hypotheses is that these particles were mechanically carried to the froth by ascendent particle-bubble aggregates. However, this may also be an indicative that small quartz grains disseminated through hematite particles are enough to make them float. A deep discussion on flotation dynamics is beyond the scope of this work, though.

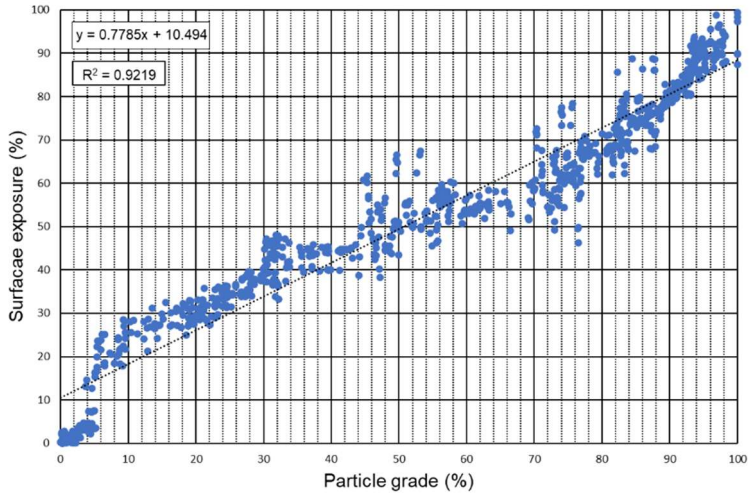

Figure 4.9. 3D surface exposure with respect to particle grade. We observe a linear relationship between both, with $R^2 = 0.9219$.

In Figure 4.10 we can also perceive a link between surface exposure and diameter. As expected, the finer the particle, the more exposed surface is available. The relationship is nearly linear with a coefficient of determination $R^2 = 0.8797$.

The mineral surface exposure is a key factor for understanding the flotation dynamics, helping to define optimum operational parameters, but its determination is extremely challenging. By defining a direct link between surface exposure, grade, and diameter, it is possible to infer the amount of exposed grain surface from the two last, which usually takes less effort to measure.

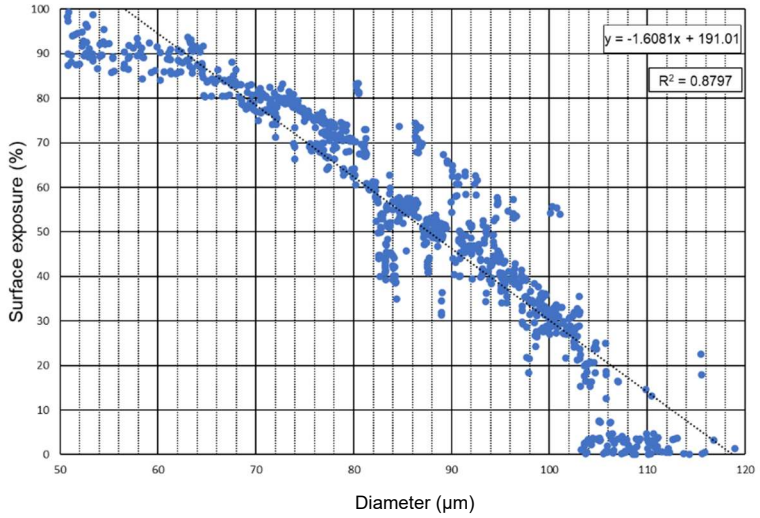

Figure 4.10. 3D surface exposure with respect to particle size. There is a nearly linear relationship between both aspects.

4.3.4 2D mineral liberation assessment by TIMA

Mineral liberation analysis by TIMA was carried out with respect to perimeter-based surface exposure. Hence, in this section, the results were compared to μCT information in terms of 2D and 3D surface exposure.

Additionally, the particle size range considered in the tomographic images was expanded to match with the size range analyzed by TIMA. The granulometry reported by TIMA showed that 94% of the particles were between +25.74 -361.00μm, and only 6% were -25.74μm. To eliminate the effect of noise that might influence the study of small particles, and considering that they represented only a minor fraction of the total, the size range analyzed from μCT data was from 25μm to 360μm.

The surface exposure distributions obtained using μCT and TIMA are shown in Figures 4.11 and 4.12. As most of the fragments are found as fully liberated quartz particles, in Figure 4.12, particles exhibiting more than 90% of exposed surface were excluded for a better visualization of the inferior classes.

The frequency of particles in the >90% class for TIMA and μCT 2D is similar. Compared to μCT 3D, there have been only a slight overestimation. As most of the particles occurring in this class are free, the degree of the stereological bias was reduced. However, for instance, for >80%<90% class, the overestimation of TIMA in comparison to μCT 3D is pronounced. Excluding the particles with more than 90% of surface exposure, according to TIMA, 60% of the particles are in between 80 and 90% of surface exposure, whereas, for the same range, the value calculated by μCT 3D was about 20%.

Both TIMA and μCT 2D liberation distributions were calculated through perimeter-based liberation. Nevertheless, it was observed significant differences between them for different classes. Taking a look in the >70%<80% class, for example, the frequency of particles reported by TIMA was about 20%, while μCT 2D reported less than 10%. To a little extent, the discrepancies in TIMA and μCT measurements may be attributed to the difference in pixel size used: 3.0μm for TIMA and 5.0μm for μCT. The results evidence the dependence of the calculated degree of liberation with the slice analyzed and that only a 3D approach is able to truly portray the characteristics of the ore.

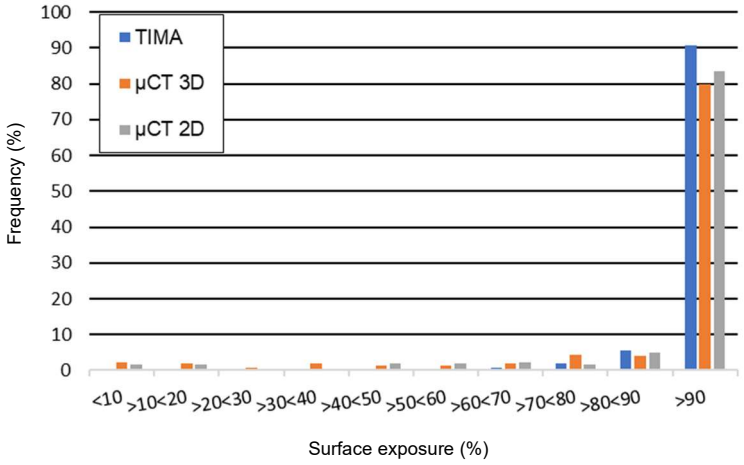

Figure 4.11. Surface exposure distributions by TIMA and µCT (2D and 3D). As most of the particles occurring in the >90% class are free particles, the degree of the stereological bias was reduced.

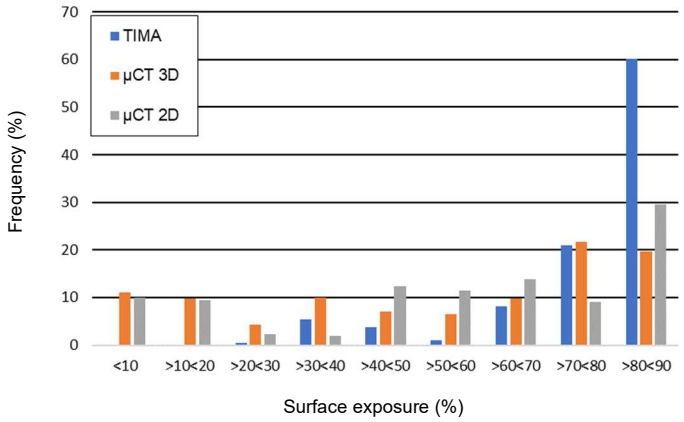

Figure 4.12. Surface exposure distributions by TIMA and µCT (2D and 3D), excluding particles exhibiting >90% of surface exposure. TIMA and µCT 2D liberation distributions were different, evidencing the dependence of liberation with the slice analyzed.

When mineral liberation measurements are made by conventional 2D techniques, such as SEM-based systems, basically only one slice from each particle is analyzed, because the procedure is time-consuming, costly, and, depending on particle size and morphology, it is just physically impracticable to prepare more than one slice per fragment. Additionally, sample preparation is not straightforward and requires precise procedures of mounting particles in resin, polishing and coating with a conductive layer. On the other hand, μCT offers the advantages of volumetric measurement, with simple and fast sample preparation, allowing that a great number of particles are examined simultaneously.

4.4 Conclusions

The chemical and mineralogical analyses showed it was composed mainly by quartz, hematite, and a small amount of goethite. The EDS analysis also showed minor quantities of siderite, kaolinite, grunerite, greenalite, diaspore, and muscovite.

The reconstructed images acquired from μCT exhibited high quality, allowing a reliable quantitative liberation investigation. 2D and 3D liberation were assessed in terms of compositional and textural characteristics of the ore by μCT. In comparison to 3D examination, both grade and surface exposure distributions were overestimated in 2D analysis. For instance, according to 2D distribution, 50% of the particles were between 90% to 99.5% of grade, whereas 3D measurement indicated that only 20% were in this range. In the case of surface exposure, 60% of the particles had a surface exposure varying from 80% to nearly 100% from a 2D perspective. However, 3D distribution revealed that approximately 20% of the particles exhibited exposed grain surface higher than 80%.

The results showed linear relationships between grade and surface exposure (R^2 = 0.9219) and between particle diameter and surface exposure (R^2 = 0.8797).

Results from TIMA showed agreement with μCT for high-grade particles. For intermediate particles, however, it did not occur. A comparison of TIMA and μCT 2D evidenced the fact that only a 3D technique is able to represent the real characteristics of particulate systems. A precise determination of liberation is of extreme relevance to guarantee the performance of downstream processes. The use of X-ray microtomography is a novelty in the field of mineral processing and comes as a solution to eliminate stereological effects.

Acknowledgements

We are very grateful to Coordenação de Aperfeiçoamento de Pessoal de Nível Superior (CAPES) and to Conselho Nacional de Desenvolvimento Científico e Tecnológico (CNPq). The first author is thankful for the research scholarship provided by CNPq.

References

BAKER, D.R. et al. An introduction to the application of X-ray microtomography to the three-dimensional study of igneous rocks. **Lithos**, v. 148, p. 262-276, 2012.

CNUDDE, V.; BOONE, M. N. High-resolution X-ray computed tomography in geosciences: A review of the current technology and applications. Earth-Sci Rev, v. 123, p. 1-17, 2013.

FANDRICH, R.G. *et al*. Two stereological correction methods: allocation method and kernel transformation method. **Minerals Engineering,** v. 8, p. 707-715, 1998.

FURAT, O. *et al*. Description of Ore Particles from X-Ray Microtomography (XMT) Images, Supported by Scanning Electron Microscope (SEM)-Based Image Analysis. **Microsc Microanal.**, v. 24, n. 5, p. 461-470, 2018.

GHOLAMI, H. *et al.* The effect of microwave's location in a comminution circuit on improving grindability of a porphyry copper deposit. **Energy Sources A**, p. 1-20, 2020.

KETCHAM, R., CARLSON, W. Acquisition, optimization and interpretation of X-ray computed tomographic imagery: applications to the geosciences. Comput Geosci, v. 27, p. 381- 400, 2001.

KING, R.P., SCHNEIDER, C.L. Stereological correction of linear grade distributions for mineral liberation. **Powder Technology**, v. 98, p. 21-37, 1998.

LANDIS, E. N., KEANE, D. T. X-ray microtomography. **Mater Charact**, v. 61, p. 1305-1316, 2010.

LEISSNER, T. *et al*. Evaluation of mineral processing by assessment of liberation and upgrading. **Minerals Engineering**, v. 153, p. 171-173, 2013.

LIN, C.L, MILLER, J.D. Cone beam X-ray microtomography for three-dimensional liberation analysis in the 21st century. **Int. J. of Mineral Processing**, v. 47, p. 61-73, 1996.

LIN, C.L, MILLER, J.D. Cone beam X-ray microtomography-a new facility for three-dimensional analysis of multiphase materials. **Mining, Metallurgy and Exploration,** v. 19, p. 65-71, 2002.

LIN, C.L, MILLER, J.D. 3D characterization and analysis of particle shape using X-ray microtomography (XMT). **Powder Technology**, v. 154, p. 61-69, 2005.

MILLER, J.D., LIN, C.L. Treatment of polished section data for detailed liberation analysis. **Int. Journal of Mineral Processing**, v. 22, p. 41-58, 1988.

PIRES, K.S. et al. Mineralogical Characterization of Iron Ore Tailings from the Quadrilatero Ferrifero, Brazil, by Eletronic Quantitative Mineralogy. **Materials Research** 22, 2019.

SAMPAIO, N. P. et al. The formation of Brazilian minerals database for integrated SEM-EDS system applied to the gold ore characterization. **Holos** 3, 2-22, 2018.

SILVA, F.L. et al. Quantitative phases characterization of clayey ceramics containing manganese ore tailings. **J. of Materials Research and Tech.** 9, 11884-11894, 2020.

UEDA, T., OKI, T., KOYANAKA, S. Experimental analysis of mineral liberation and stereological bias based on X-ray computed tomography and artificial binary particles. Adv. **Powder Technology**, v. 29, p. 462-470, 2018.

UEDA, T. Experimental validation of a statistical reliability method for the liberation distribution measurement of ore particles. **Minerals Engineering**, v. 140, 105880, 2019.

REYES, F., LIN, Q., UDOUDO, O., DODDS, C., LEE, P.D., NEETHLING, S.J. Calibrated X-ray micro-tomography for mineral ore quantification. **Minerals Engineering**, v. 110, p. 122-130, 2017.

REYES, F., LIN, J.J., CILLIERS, S.J., NEETHLING, S.J. Quantifying mineral liberation by particle grade and surface exposure using X-ray microCT. **Minerals Engineering**, v. 125, p. 75–82, 2018.

VAN DER WIELEN, K.P., ROLLINSON, G. Texture-based analysis of liberation behaviour using Voronoi tessellations. **Minerals Engineering,** v. 89, p. 93-107, 2016.

WANG, Y., LIN, C.L., MILLER, J.D. Quantitative analysis of exposed grain surface area for multiphase particles using X-ray microtomography. **Powder Technology**, v. 308, p. 368-377, 2017.

WANG, Y., MCCLUNG, C., LIN, C.L., MILLER, J.D. Stereological correction of perimeter-based estimates of exposed grain surface area. **Minerals Engineering**, v. 126, p. 64-73, 2018.

WILLS, B. A., FINCH, J.A. Wills' Mineral Processing Technology: An Introduction to the Practical Aspects of Ore Treatment and Mineral Recovery. Elsevier, 2016. 498p.

ZHANG, J., SUBASINGHE, N. Prediction of mineral liberation characteristics of comminuted particles of high-grade ores. **Minerals Engineering**, v. 49, p. 68-76, 2013.

CHAPTER 5

FINAL CONSIDERATIONS

5.1 Contributions and originality

The present study addressed the applicability of X-ray microtomography to overcome the stereological effect associated to mineral liberation assessment from 2D techniques. X-ray microtomography itself in mineral processing and extractive metallurgy is a recent topic in the literature, as deep investigations were restricted in the past due to limitations in spatial resolution. Now that it is possible to achieve high resolution images, in the sub-micrometer range within short acquisition time, the technique has become more attractive to the field and has drawn the attention of many researchers.

It is well established that a precise determination of mineral liberation is very important to guarantee the efficiency of concentration operations and that traditional measurements from polished sections carry stereological errors.

Since the stereological bias of degree of liberation was first pointed out by Gaudin, in 1939, there have been many works with a variety of approaches trying to correct it. The studies go from mathematical modeling and simulation to observations of artificial particles, but none has succeeded in finding a general correction that applies to a vast range of ores.

More advantageously than finding a correction model, X-ray microtomography enable us to direct measure the real volumetric characteristics of mineral ores, eliminating the necessity of applying any correction. The novelty of the technique in the field, however, implies that there are only few works published on the subject and further studies are necessary to consolidate the applicability of the technique.

In Chapter 3, the technique was used for the first time to explore the characteristics of liberation of a complex ore such as bauxite. The stereological errors are even more pronounced for particles with complex internal structures and X-ray microtomography proved to solve this challenge. The depletion of high-quality bauxite reserves demands a

more comprehensive understanding of the ore, aiming to implement accurate concentration strategies to remove silica of high-silica bauxite reserves.

In Chapter 4, it was tested the applicability of X-ray microtomography for the investigation of an iron ore tailing. The results were compared to the ones obtained by a commonly used SEM-based technique, the TESCAN Integrated Mineral Analyzer.

Both chapters proved that 2D-based estimations do not portray the real characteristics of mineral ores. It was clear that 2D analysis overestimates the degree of liberation by grade and surface exposure, being more pronounced when less cross-sections are used in the measurement. X-ray microtomography, followed by the proposed image processing routine, which is as important as the technique itself, was able to overcome the stereological bias.

Nevertheless, X-ray microtomography and SEM-based systems have their own advantages and disadvantages, and, therefore, should not be discredited. In Table 5.1, a list of attributes are described and compared between lab-based µCT and SEM-EDS technique.

Table 5.1. Major advantages and drawbacks of µCT and SEM-EDS systems.

Attributes	**µCT**	**SEM-EDS**
Stereological bias	✓ Direct measurement of 3D attributes, excluding the need for stereological correction	X Requires stereological correction, which are usually unsatisfactory
Sample preparation	✓ Requires simple or no sample preparation. The particles only need to be placed in a plastic tube, for example	X Difficult and very time-consuming, requiring particles to be mounted in resin, polished, and covered with a thin conductive coating
Sample size and resolution	X Resolution limited by sample size	✓ Usually, more particles can be analyzed with greater resolution

Data analysis	X Takes effort, demanding dedicated software solutions and careful work ✓ Once images are processed, a greater number of characteristics can be extracted ✓ Transverse and longitudinal views are easily produced by visualization software	✓ Quantitative liberation data can be extracted virtually right after acquisition X Only one plane is visualized
Mineralogical information	X Does not provide the mineralogy of the sample	✓ Besides morphological, also provides chemical and mineralogical information
Type of the technique	✓ Non-invasive and non-destructive	X Destructive
Accessibility to equipment	X Currently, less facilities are available	✓ Due to the consolidated use of the technique, there are more equipment and more qualified personnel available
Complexity of the equipment	✓ Simpler components	X Composed by a series of sensible components, which means maintenance can be problematic X Requires very stable power supply, vacuum and cooling system

Besides the scientific contribution of this work to the field of mineral processing, it has an important role in spreading the use of X-ray microtomography as an advanced materials characterization technique. It is an extremely versatile tool that finds application in many fields and there is the necessity of forming specialized human resources in the technique.

5.2 Suggestions for further research

Image processing and quantitative analyses of tomographic data are not straightforward and take a lot of work. The first recommendation is to dedicate in machine learning to create routines specialized in mineral liberation analysis. This would save a lot of time and make X-ray microtomography more suitable to habitual use.

In the case of minerals treated by flotation, another suggestion is to measure surface exposure of feed, concentrate, and tailing, to investigate the impact and requirements for the operation.

Finally, try to apply high-speed X-ray tomography to evaluate the employment of the technique in the industry.

CAPÍTULO 5

CONSIDERAÇÕES FINAIS

5.1 Contribuições e originalidade

O presente estudo abordou a aplicabilidade da microtomografia de raios-X para solucionar o efeito estereológico associado à avaliação da liberação mineral a partir de técnicas 2D. A microtomografia de raios-X por si só, no processamento mineral e metalurgia extrativa, é um tópico recente na literatura, visto que investigações minuciosas eram restritas no passado devido às limitações de resolução espacial. Agora que é possível obter imagens de alta resolução, na faixa submicrométrica e em curto tempo de aquisição, a técnica se tornou mais atrativa para o campo e tem chamado a atenção de muitos pesquisadores.

Já é bem estabelecido que uma determinação precisa da liberação mineral é muito importante para garantir a eficiência das operações subsequentes de concentração e que medições tradicionais de seções polidas carregam um grande efeito estereológico.

Desde que o efeito estereológico do grau de liberação foi apontado pela primeira vez por Gaudin, em 1939, houveram muitos trabalhos com diferentes abordagens tentando corrigi-lo. Os estudos vão desde modelagem matemática e simulação até observações de partículas artificiais, mas nenhum conseguiu encontrar uma correção geral que se aplique a uma vasta gama de minérios.

Mais vantajoso do que encontrar um modelo de correção, a microtomografia de raios X nos permite medir diretamente as características volumétricas reais dos minérios, eliminando a necessidade de aplicar qualquer correção. A novidade da técnica na área, entretanto, implica que há poucos trabalhos publicados sobre o assunto e que mais estudos são necessários para consolidar a aplicabilidade da técnica.

No Capítulo 3, a técnica foi usada pela primeira vez para explorar as características de liberação de um minério complexo como a bauxita. Os erros estereológicos são ainda mais pronunciados para partículas com estruturas internas complexas e a microtomografia de raios-X comprovou superar esse desafio. O esgotamento das reservas de bauxita de alta qualidade exige um entendimento mais

abrangente do minério, visando implementar estratégias de concentração precisas para remover a sílica das reservas de bauxita com alto teor de sílica.

No Capítulo 4, foi testada a aplicabilidade da microtomografia de raios-X para a investigação de um rejeito de minério de ferro. Os resultados foram comparados aos obtidos por uma técnica 2D comumente usada, baseada em Microscopia Eletrônica de Varredura, o *TESCAN Integrated Mineral Analyzer*.

Ambos os capítulos provaram que as estimativas baseadas em observações 2D não retratam as características reais dos minérios. Ficou claro que a análise 2D superestima o grau de liberação, por teor e por superfície exposta, sendo mais pronunciado quando menos seções transversais são usadas na medição. A microtomografia de raios X, seguida da rotina de processamento de imagens proposta, tão importante quanto a própria técnica, conseguiu superar o efeito estereológico.

No entanto, a microtomografia de raios-X e os sistemas de análise baseados em observações ao MEV têm suas próprias vantagens e desvantagens e, portanto, não devem ser desacreditados. Na Tabela 5.1, uma lista de atributos é descrita e comparada entre a µCT e os sistemas MEV-EDS.

Tabela 5.1. Principais vantagens e desvantagens da µCT e dos sistemas MEV-EDS.

Atributo	**µCT**	**SEM-EDS**
Erros estereológicos	✓ Medição direta de atributos 3D, excluindo a necessidade de correção estereológica	**X** Requer correção estereológica, que geralmente são insatisfatórias
Preparação de amostra	✓ Requer preparação simples ou nenhuma. As partículas só precisam ser colocadas em um tubo plástico, por exemplo	**X** Difícil e muito demorada, exigindo que as partículas sejam embutidas em resina, polidas e cobertas com um revestimento condutor fino
Tamanho de amostra e resolução	**X** Resolução limitada pelo tamanho da amostra	✓ Normalmente, mais partículas podem ser analisadas com maior resolução

Análise dos dados	X Trabalhosa, demandando softwares específicos e um trabalho cuidadoso ✓ Uma vez que as imagens são processadas, um maior número de características pode ser extraído ✓ Vistas transversais e longitudinais são facilmente produzidas por softwares de visualização	✓ Dados quantitativos de liberação podem ser extraídos praticamente logo após a aquisição X Apenas uma seção é visualizada
Informação mineralógica	X Não fornece a mineralogia da amostra	✓ Além de informações morfológicas, fornece também químicas e mineralógicas.
Tipo da técnica	✓ Não-invasiva e não-destrutiva	X Destrutiva
Acessibilidade a equipamentos	X Atualmente, menos instalações estão disponíveis	✓ Devido ao consolidado uso da técnica, há mais equipamentos e mais pessoal qualificado disponível
Complexidade do equipamento	✓ Componentes mais simples	X Composto por uma série de componentes sensíveis, o que significa que a manutenção pode ser problemática X Requer fonte de alimentação, sistema de vácuo e refrigeração muito estáveis

Além da contribuição científica deste trabalho para a área de processamento mineral, ele tem um importante papel na difusão do uso da microtomografia de raios-X como uma técnica avançada de caracterização de materiais. É uma ferramenta extremamente versátil, que encontra aplicação em diversos campos, e existe a necessidade de formar recursos humanos especializados na área.

5.2 Sugestões para trabalhos futuros

O processamento de imagens e as análises quantitativas de dados tomográficos não são simples e exigem muito trabalho. A primeira recomendação é se dedicar ao aprendizado *machine learning* para criar rotinas especializadas em análise de liberação mineral. Isso economizaria muito tempo e tornaria a microtomografia de raios-X mais adequada para o uso habitual.

No caso de minerais tratados por flotação, outra sugestão é medir a exposição superficial da alimentação, concentrado e rejeito, para investigar o impacto e as necessidades da operação.

Por fim, tentar aplicar a tomografia de raios-X de alta velocidade para avaliar o emprego da técnica na indústria.